Tuning Mesoscopic Self-Assembly Behavior via Nano Building-Block Interactions and Architecture

by

Ryan L. Marson

A dissertation submitted in partial fulfillment
of the requirements for the degree of
Doctor of Philosophy
(Materials Science and Engineering)
in the University of Michigan
2015

Doctoral Committee:

Professor Sharon C. Glotzer, Chair
Professor Nicholas Kotov
Professor Ronald G. Larson
Professor Peter X. Ma
Professor Anish Tuteja

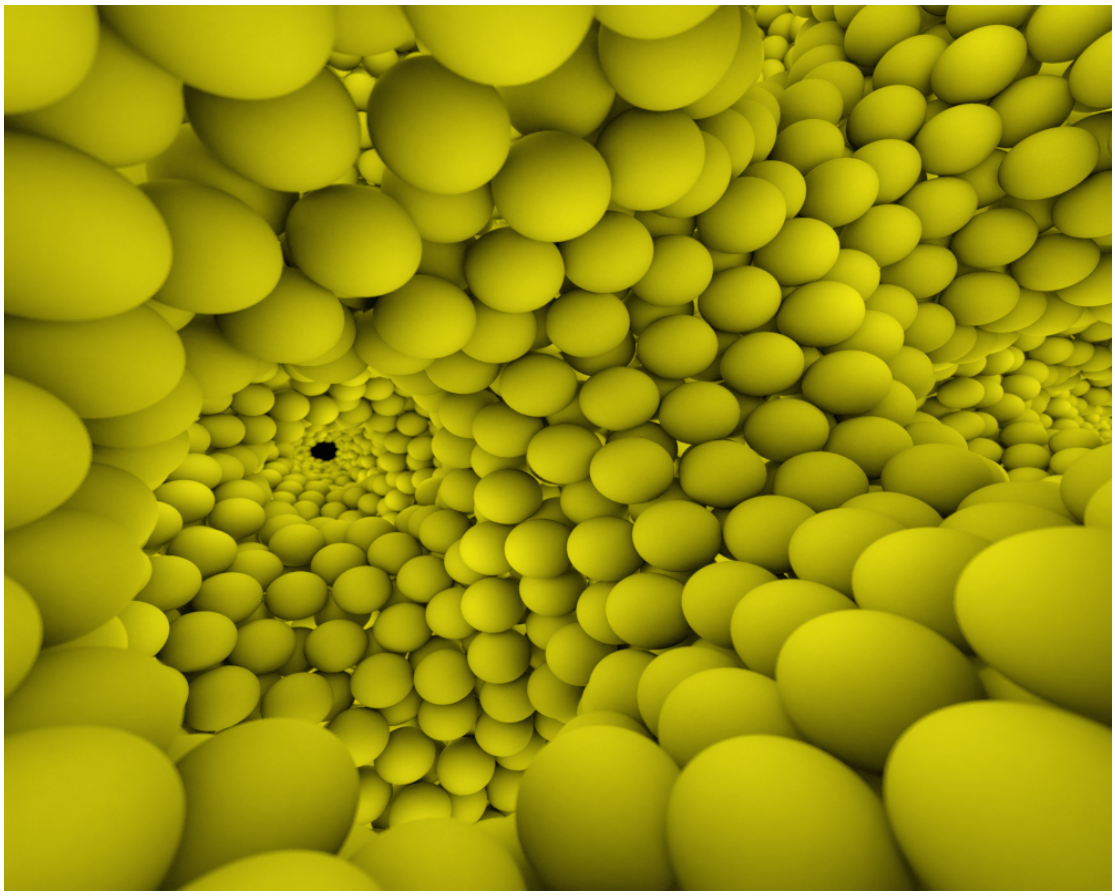

2015

For my father, Rex. May I always maintain your enthusiasm, generosity, and positive outlook on life. Each and every day I find an opportunity to be grateful for the love and support you gave so freely and unconditionally. Each and every day I see more of you in me. You are dearly missed.

Acknowledgments

I would first and forest like to thank my advisor Sharon Glotzer for taking me on and the University of Michigan for the outstanding support and facilities they've provided me with over the course of my doctoral work. Sharon has given me the freedom to pursue the kinds of research I find most interesting, and built an incredible team of researchers, all while maintaining her brilliance and passion for research. She has also allowed me to share in amazing collaborations with Nick Kotov and Peter Ma, amongst many others. I'm indebted for these opportunities. I have had a tremendous support network over the past few years. I am surrounded by incredibly intelligent, and incredibly patient, individuals who have guided me through this process. Carolyn Phillips helped me to craft my first paper in the Glotzer group, wrangling in my overly verbose scientific prose, producing clear, more concise, and imminently more readable documents; all of this while being a mentor and friend. Joshua Anderson empowered me with the fastest and greatest (in my humble opinion) Molecular Dynamics code in the land, HOOMD, and built up tools to bridge our sundry group codes to the complex world of high performance computing. Matthew Spellings has patiently and dutifully shepherded my many random-walks into the world of software development, and helped me to be a more complete computer scientist. Greg van Ander's brilliance is matched only by his utterly humble, decent, and friendly nature. Eric Irrgang, Ben Schultz, and Eric Jankowski have always been willing to think deeply and technically about problems with me, helping me to firm up my intuition, and inspiring me to be a better researcher; they've also shared adventures in bicycles, beers, and beyond. Karen Coulter has crafted the infrastructure that allows us to get anything done, and runs a pretty fine research lab, by my estimation. To the rest of the Glotzer group, thank you too! Each and everyone of you has brought a new perspective into my life, and have helped shape me as an individual. Most of all, I thank my friends and family. They are too numerous to thank, both in number and in quality; I am deeply humbled. There is nothing that I could have done to deserve you all, but I will do everything in my power to earn it.

TABLE OF CONTENTS

LIST OF FIGURES

ABSTRACT

Tuning Mesoscopic Self-Assembly Behavior via Nano Building-Block Interactions and Architecture

by

Ryan L. Marson

Chair: Sharon C. Glotzer

Using molecular dynamics (MD) computer simulations we show that a variety of complex, technologically relevant phases emerge from tuning aspects of nanoparticle architecture and interactions. In doing so, we demonstrate that nanoparticles can be thought of as building-blocks in larger scale assemblies over which we can tune nearly every aspect of the structure for specific applications such as photonics, photovoltaics, or catalysis. We highlight three specific case studies - polymer/nanoparticle composite building-block assemblies, star polymer microdroplets, and amino-acid coated nanoparticles with embedded dipoles that form rods of preferred chirality. In all cases predictions from simulations are used to either guide building-block assembly or to offer detailed insight into structures that were not previously understood. Additionally, we establish general, domain-agnostic mesophase behavior, as well as hypothesize synthesis and assembly strategies to target highly specific structures for any given application.

CHAPTER 1

Introduction

1.1 Introduction

We are in the midst of a materials revolution – a revolution in which materials will be designed, optimized, and engineered, rather than merely selected, for targeted properties, behavior, and function. Future materials and devices will be made and tailored to target specifications, combining disparate and even competing attributes of multiple materials classes to achieve new functionality. These materials will borrow heavily from nature, which sets the standard for complex materials functionality - we need only look at the cells within our body, or into the scales of a butterfly to see the exquisite functionality and complexity that can be achieved. This intrinsic tailorability of materials properties will contrast starkly with today's relatively static matter that is largely chosen, rather than designed, for the task at hand [20].

To tackle this next generation of materials, we must leverage sophisticated tools to conceptualize and quantify the accessible materials design space. Since the first studies of hard disks conducted in the late 1950s, computer simulation has evolved into a powerful, and in many cases, indispensable, tool for investigating atomic, molecular, and mesoscopic systems. Revolutionary advances in computer architectures and simulation algorithms over the past two decades have enabled computational scientists to elucidate problems spanning many orders of magnitude greater in time and length scales and from various angles. In particular, open-source MD packages such as Gromacs [21], LAMMPS [22], and HOOMD-Blue [23, 24] have facilitated the spread of tools and ideas, as well as set a standard for rigorous and reproducible simulations that scale from laptops to supercomputing clusters. More interesting, perhaps, is the ability of computational studies to offer predictions that are testable, which prove highly valuable for bottom-up engineering of nanomaterials. Finally, the ability to predictively design new materials is at hand, and available to computational experts and non-experts alike.

The rational design of nanomaterials via computer simulation requires identifying the desired target nanostructures, candidate building blocks, and efficient assembly pathways. In this regard, computational techniques such as Monte Carlo, molecular dynamics (MD), and self-consistent field theory have played a vital role in predicting assembled structures obtained with almost arbitrary types of building blocks, including block copolymer and nanoparticle systems [25, 26, 27]. Coupled with today's increasingly powerful computing capacity, these techniques allow simulators to rapidly predict assembled morphologies, screen candidate building blocks, and search for efficient assembly pathways over a wide range of parameters.

Next generation materials require new types of building blocks, made in large quantities, that can self-assemble into complex, functional, or reconfigurable structures [28]. Bottom-up assembly engineering builds upon the thermodynamic foundations of assembly science to engineer these building blocks in order to optimize the yield (quantity as well as quality) of a desired assembly. This paradigm shift is possible today due to the great strides in synthesis and characterization over the past decade. New nanoparticle and colloidal building blocks, comprised of organic, inorganic, and/or biological constituents,[29, 30, 31, 32, 33, 34, 35, 36, 37] and with arbitrary shape[38] and interaction patchiness[39], can now be made nearly to specification.

Nanoparticles provide a versatile assembly platform with numerous design axes.[28] Researchers have demonstrated extraordinary control over the shape and composition of these particles.[40, 41, 42] Moreover, interactions between these particles can be altered to affect the nature of how they assemble. Examples include induced dipoles due to surface charges[43], and surface interactions due to stabilizers or coatings[44]. These interactions can create free stranding structures such as wires[30, 37], sheets[34], or clusters[36]. This toolkit can be used to obtain specific morphologies that suit a target application.

Polymers are another interesting class of building block that are ubiquitous in assembly engineering.[45] Immiscibility between segments of the polymer block can be used to induce phase separation between components, resulting in complex phase behavior.[46, 47, 48, 26, 49, 27] Moreover, the ability to control their architecture from linear[26], to star-shaped[50], as well as other morphologies, introduces architectural complexity; this complexity can be used as an additional tool for influencing the resulting self-assembled structure.

A final compelling class of nanoscale building block we will addess in our studies is the tethered nanoparticle (TNP)[51] : a nanoparticle (NP) to which a polymer tether (T) is permanently attached, creating a surfactant-like, amphiphilic object with a large (NP) head group and a tail (T). In more complex architectures, multiple tethers, of similar or

different type, attached at different places on the NP, are also possible. The TNP conceptual framework allows for tuning domain properties on nearly every scale.[51] When assembled, nanoparticles make up the functional domains of the material, while polymer tethers form the continuous space between these domains; alternatively, the polymer domains can serve as the functional material, while nanoparticle domains can form surfaces or other structural elements. Moreover, TNPs create a spectrum of mesoscopic assemblies, including: 1) pseudo - 2D assemblies (e.g. lamellae), 2) micellar structures adopting BCC, Frank-Kasper, or quasiscrystalline patterns, and 3) complex diamond, gyroid, or other networks.

Between these classes of building blocks, an enormous design space is accessible for the design and discovery of new materials. Before moving into our case studies, we will briefly review the available toolkit for assembly engineering of mesoscale systems, which includes current advances in the synthesis of building-blocks, as well as how they are being utilized in self-assembly. We then turn our attention to how computer simulation has been applied to rapidly screen candidate building blocks for useful structures, or even to predict the type of building blocks that might assemble a desired structure. In the introductory sections that follow, we briefly review the status of work in the field of tuning soft-matter mescoscopic assemblies - both experimental and computational. Figures and text in this introductory section is reproduced (and adapted where appropriate) from our forthcoming prospective, "Rational design of nanomaterials from assembly and reconfigurability of polymer-tethered nanoparticles", *MRS Communications*, which is under review at the time of preparation of this thesis.[9]

1.2 Assembly toolkit for nanoscale building - blocks

1.2.1 Nanoparticle building blocks

Tremendous effort in synthesis techniques has been devoted to controlling the shape, size, and composition of nano building blocks for high yield and uniformity. Methods such as seed-mediated growth and redox transmetallation have been widely applied, allowing for a zoo of building blocks in various geometries (e.g. spheres, rods, cubes, plates, stars) and materials (e.g. semiconductor, metal and metallic oxides).[40, 41, 52] Other anisotropy dimensions have also been realized via selective surface modification, functionalization, and compartmentalization [6]. For instance, nanoparticles and colloids can be functionalized with different chemical moieties through the use of appropriate stabilizers and linkers (Fig. 1.1(a)). To precisely control the number of the attached functional groups, one can

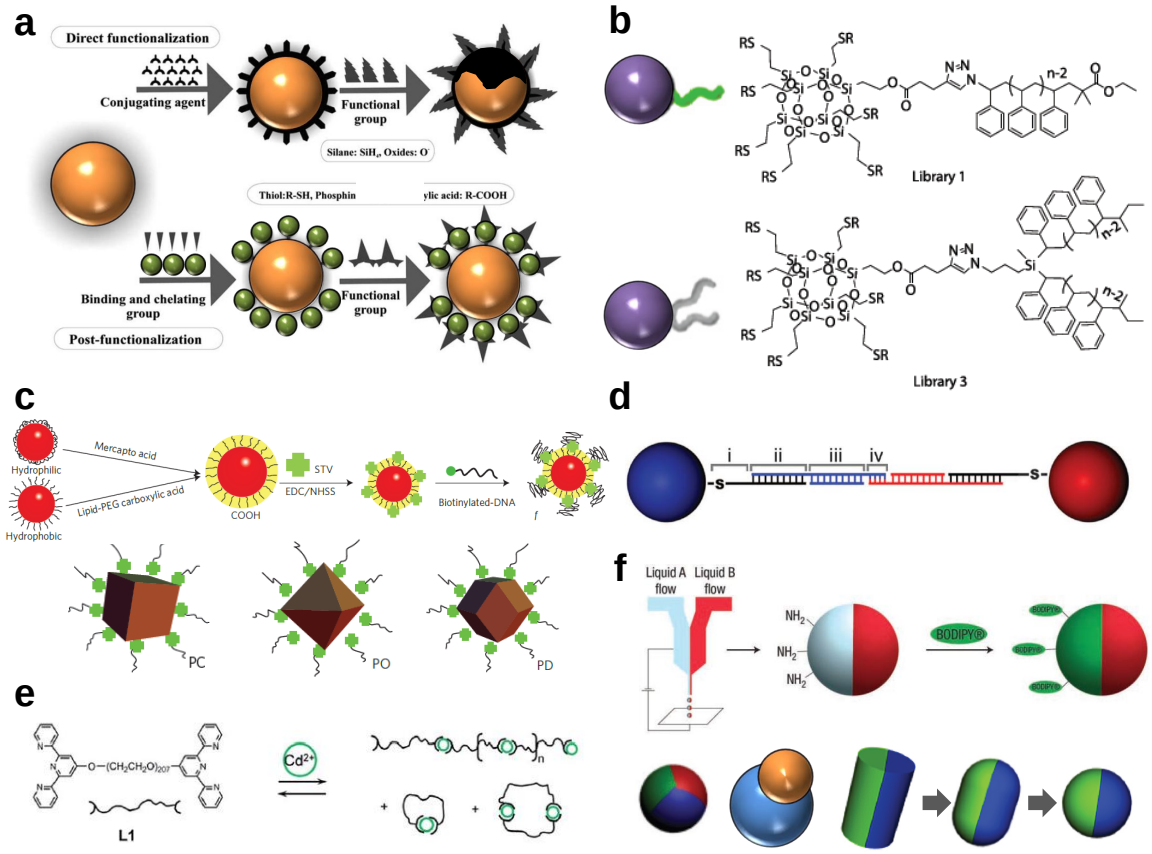

Figure 1.1: *Experimental building-blocks*: (a) Functionalization (adapted from Ref. [1]); (b) click reactions (Ref. [2]); DNA conjugation with (c) multiple DNA strands [3] and (d) single DNA strand [4] per building block; (e) coordination with metal ions [5] and (f) electrohydrodynamic co-jetting methods that are used to produce multicompartmentalized building blocks [6, 7, 8]. Figure taken from our prospective.[9]

take advantage of techniques based on "click chemistry" [53, 2] and DNA conjugation [54, 4, 3, 55].

For nanoparticles noble metals have been used to create a variety of surface modified facetted polyhedra.[38, 56, 41, 57, 38, 42] These particles are usually created using a combination of seed mediated growth, oxidative etching, reactions within the solvent, or electrochemical means to guide the growth preferentially over different facets.[57] Additionally, surface stabilizers are required for individual nanoparticles.[56] Surface modification adds an additional parameter that can be used to later guide the assembly of the nanoparticles.

In the case TNPs, a variety of methods are used to create composite blocks. In "click chemistry", for example, [53, 2] (Fig. 1.1(b)), multicomponent building blocks, e.g. surfactants and shape amphiphiles, are created through a series of sequential "click reactions", namely the copper-catalyzed azide-alkyne cycloaddition (CuAAC) reaction and the thiolene reaction [53, 2]. This technique has recently been used to interchange nearly every portion of the building block [58, 2, 59]. Examples include the ability to interchange head groups from POSS cages to gold nanoparticles, as well as to exchange polymer types such as polystyrene or PMMA; additionally, the size, number, and placement of these chemically distinct domains can be controlled, such as tethering a single corner of a POSS molecule with one or more polymer tethers.[53, 58, 2, 59]

An alternative strategy that has also produced numerous candidate TNPs is to functionalize nanoparticles or colloids with a finite number of DNA oligomers (Fig. 1.1(c,d)). The highly specific interactions between complementary strands of DNA induce attraction between specific nanoparticle type pairs. This suggests a robust framework that has already enabled the design of numerous nanoparticle superlattices upon tuning the nanoparticle size and bond distance using DNA linkers.[4, 3, 55]

TNP colloidal "molecules" are reminiscent of their molecular counterparts, as their interaction can be made directional and highly specific. For example, coordination polymeric structures exist that link polymeric or molecular sub-units using non-covalent interactions, creating adaptive and responsive polymer-like superstructures. In these building blocks interactions are made highly specific at certain sites via the use of suitable metallic ions and ligands (Fig. 1.1(e)).[5] Patchy particles and multicompartmentalized particles are realized via selective surface treatment methods [60] and electrohydrodynamic co-jetting (Fig. 1.1(e)), respectively. Recently, Sacanna and Pine reported a simple, yet generic, route to fabricating colloids with tunable cavity, which enable a host of complex assemblies [61].

1.2.2 Assembled nanostructures

While initial experimental effort were primarily directed at building blocks synthesis, attention has increasingly turned to structure assembly. Combining the functionality of nanoparticles, with the flexibility of polymers, and the ability to "click" particles together to make composite blocks produces an enormous design space. This design space is comparable to that of copolymers, but with an expanded spectrum of properties and structures beyond the complex phases exhibited by coordination polymers and block copolymers [62, 25, 45, 5, 46, 26, 63, 54, 10] (Fig. 1.2(a-c)).

Nanoparticles alone form numerous phases, including glasses, as well as liquid and solid crystals.[64, 38, 41, 65] In these cases crystalline phases range from standard simple, face-centered, and body-centered cubic, to extremely large and complex unit cells such as the β-Mn phase formed by dodecahedra. These particles must be stabilized with coatings[56], which allows for additional design axes, such as coupling the assembly to the presence of light[37, 66] or influencing the handedness of the resulting structure[67, 68].

As mentioned previously, direct realizations of TNP assembly have come from the use of "click chemistry" to attach tethers to nanoparticles directly, creating gram quantities of material. [53, 58, 2] TNPs created with this method have been used to self-assemble many of the same structures observed in block copolymers, but with the additional benefit of controlling the specific material composition of each domain of the material. By tuning various portions of the block geometry, different types of structures are accessible. For example, by increasing the length of a polystyrene tether attached to the corner of a polyhedral oligomeric silsesquioxane (POSS) cube Cheng et al. can tune between lamella, the double gyroid, hexagonal tubes, and BCC micelles, as seen in Fig. 1.2(b).[59] Moreover, these structures demonstrated a high degree of sensitivity to the block features; by fixing the volume fraction of each component, but adding additional tethers to one corner of the POSS cube, they could induce a phase inversion in the hexagonal tubes phase, resulting in a matrix of POSS and tubes of polymer. Similarly, by replacing a single tail with two tails of half the length, they could select either the double gyroid for the former or hexagonal tubes for the latter.

For building blocks with highly specific interactions, it is possible to design nanostructures with a higher degree of complexity. For instance, using self-complementary and non-self-complementary DNA strands, Macfarlane et al. have showed that one can program the multivalent interaction between DNA-functionalized nanoparticles [4]. With such encoded interactions, the resulting structure can be a NaCl or simple cubic lattice, depending on the size ratio of the inorganic nanoparticles (Fig. 1.2(d)).

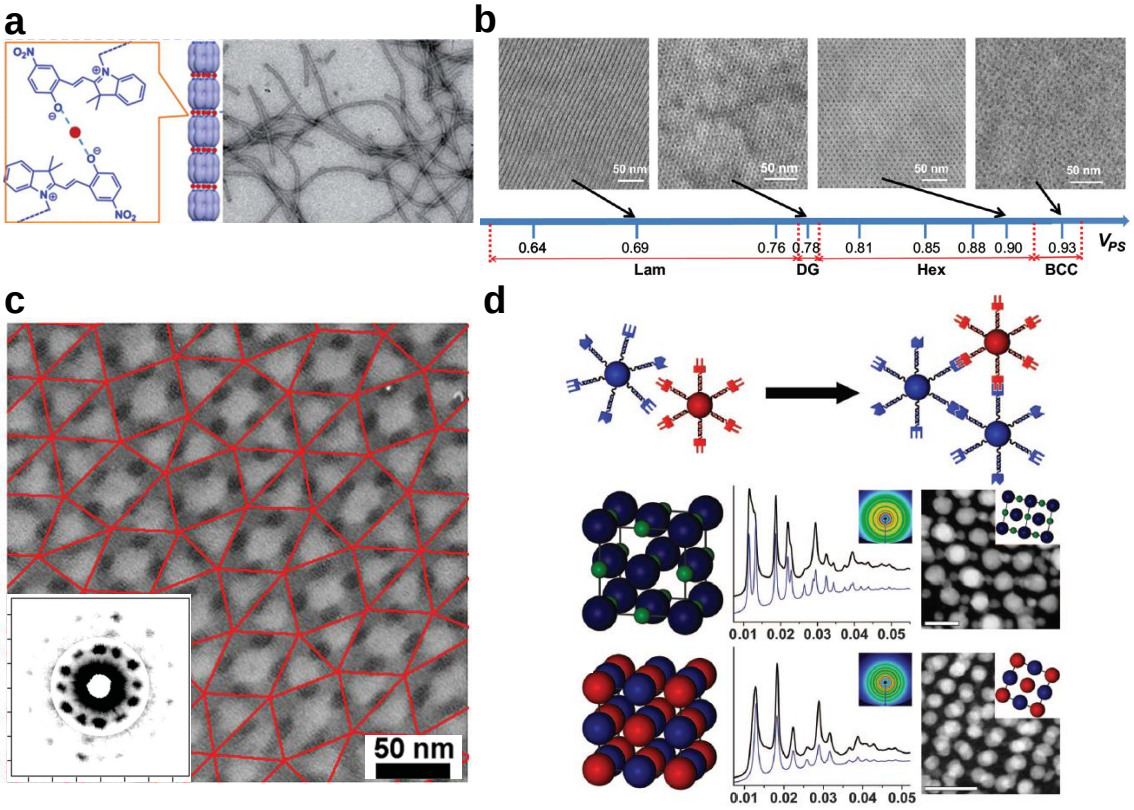

Figure 1.2: *Experimental building-block assemblies*: (a) Nanotubular assemblies from coordination polymers upon addition of divalent metal ions (red circle) [5], (b) Assembled structures from shape amphiphiles, including lamellar, gyroid, hexagonal cylinders, and BCC micelle phases, as reported in [2]. (c) Dodecagonal quasicrystal formed in a blend of polyisoprene-polystyrene-poly(2-vinylpyridine star block copolymers / polysterene homopolymer blend [10]; (d) Ordered structures formed by gold nanoparticles functionalized with complementary DNA strands (top): NaCl lattice (middle) and simple cubic lattice (bottom) [3]. Figure taken from our prospective.[9]

1.3 Computational design of functional nanostructures

Given the versatility of the assembly toolkit and the enormity of the design space provided by these nanoscale building blocks, what types of structures are possible? Can we design and assemble domain-specific materials with precisely controlled bulk and nano-scale properties?

This question drove an initial flurry of computational investigation into tethered nanoparticles [51, 69] a decade ago. Nanoparticles, it was hypothesized, would offer a truly limitless design platform, provided they could successfully be used to create composite polymer-nanoparticle blocks. Initial investigations focused on establishing relationships between existing theory for polymers and surfactants, and TNPs via simulation [70, 71]. Toward this end, work initially centered on the phase behavior [51, 69, 70, 72, 73] and properties [74, 75, 76, 77, 78] of TNPs, focusing on the size effects of an isotropic nanoparticle. Fig. 1.3 shows examples of interesting assembled structures from these studies, including double gyroids[11], cylinders and columnar structures[12], bilayer sheets[13], and dodecagonal quasicrystals[14]. Key amongst these findings was the realization that the phase behavior of tethered nanoparticles, to a great extent, is consistent with that of surfactants and liquid crystals [70]. Recently, many of these initial findings have also been corroborated with experiments [59].

Given the close relationship between tethered nanoparticles and liquid crystals [71], the roles of the shape of the nanoparticle head group have also been extensively investigated [79, 80, 81, 82, 83, 84]. In these cases, it was again found that structures and transitions similar to those in liquid crystals were observed, such as lamella, gyroids, cylinders, and micelles. However, the connectivity and coordination of the micelles and networks were altered by the packing of the head groups. Additional types of liquid-crystalline ordering were found within these domains, such as long micelles and lamella [83], twisted columns and sheets with liquid crystalline order [82, 81, 79], honeycombs [81], and gyroids [80].

Most recently, the effects of shape alone have been highly scrutinized, returning to purely nanoparticle systems.[38, 64, 85, 86, 65, 87, 88, 89, 90, 42] Key amongst these findings was that shape alone is enough to stabilize an enormous diversity of crystalline structures. For example, by studying over 100 different polyhedra Damasceno *et al.*[65] showed several classes of structures such as liquid crystals, glasses, and numerous crystal structures can form based on particle shape. Moreover, the study demonstrated the ability to reasonably predict the class of structure that might form *a priori*.

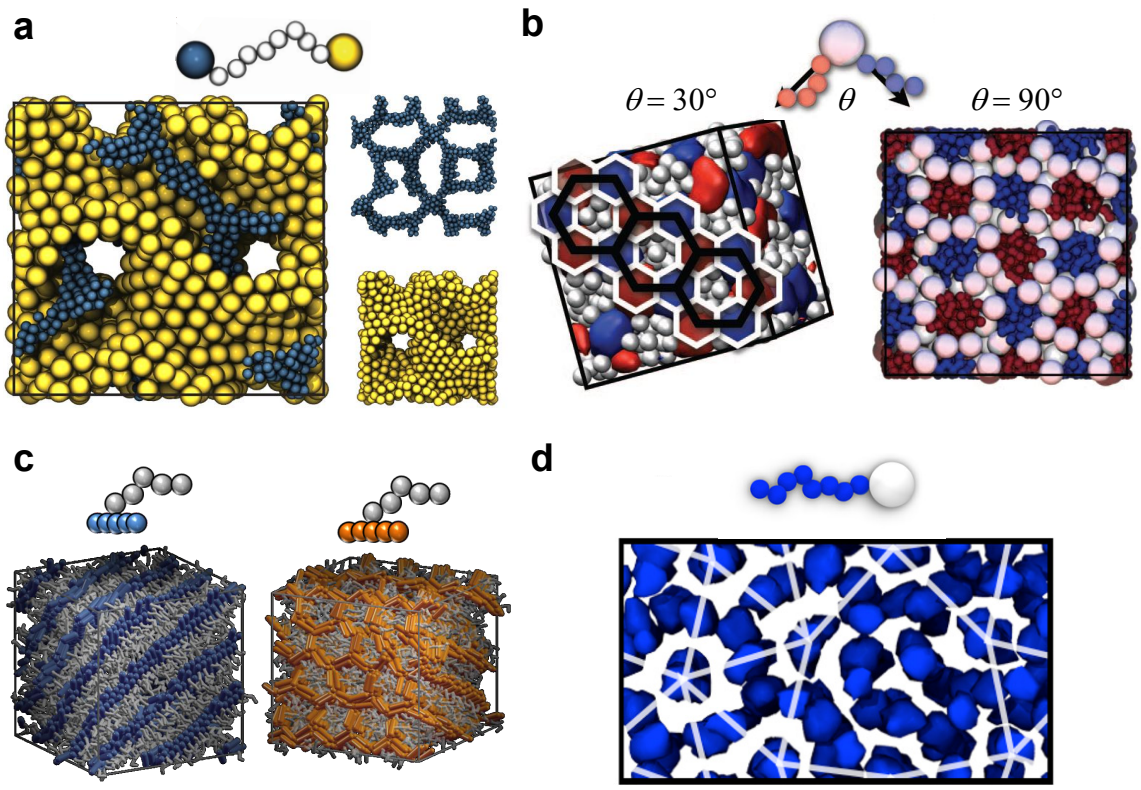

Figure 1.3: *Simulated mesophases*: (a) Double gyroid formed by tethered nanoparticle telechelics [11]; (b) tetragonally cylinder structure and [6;6;6] columnar structure assembled by di-tethered nanospheres with different planar angles, θ, between two tethers [12]; (c) bilayer sheets and honeycomb grid formed by laterally tethered nanorods [13]; (d) dodecagonal quasicrystal formed by mono-tethered nanoparticles [14]; Figure taken from our prospective.[9]

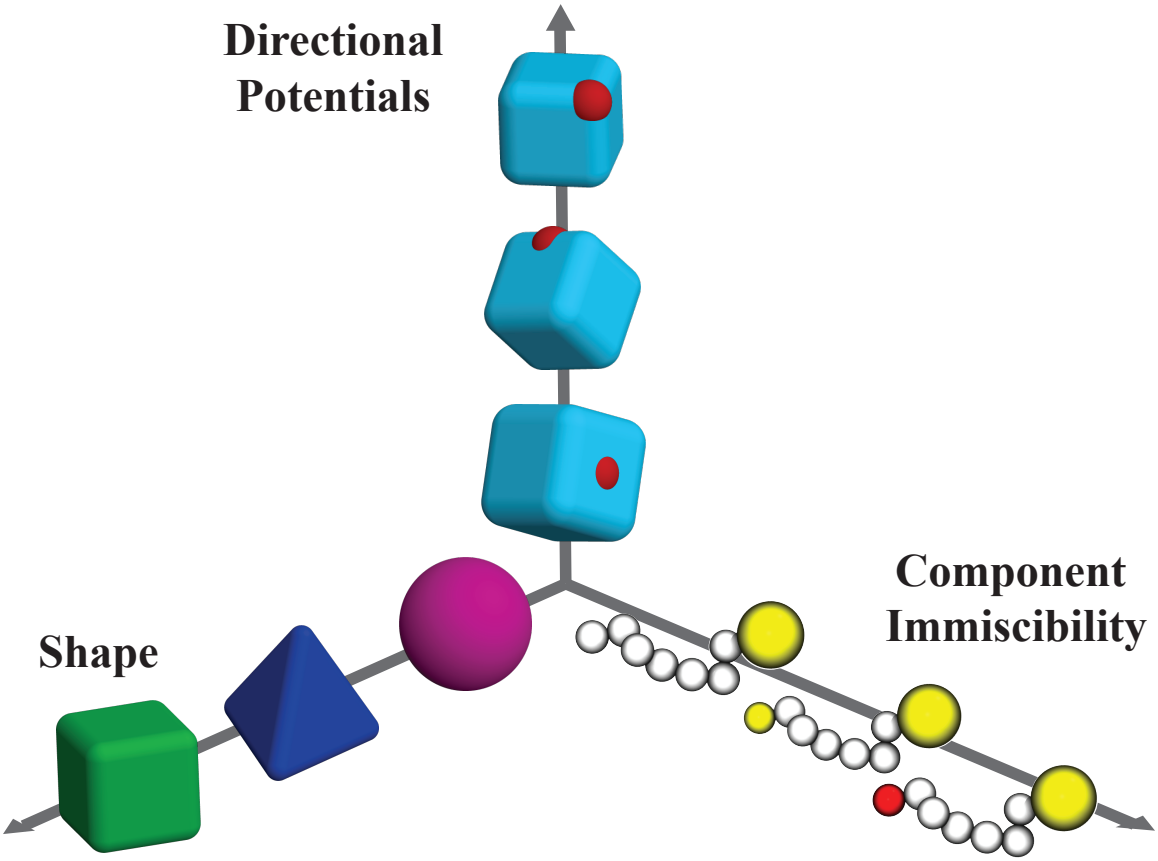

Figure 1.4: *Mesoscale assembly "anisotropy" axes*: Anisotropy axis for relevant assembly dimensions in nanoparticle systems. By tuning nanoparticle shape and interaction, researchers can tune the resultant structure and ordering in TNP systems. Additionally, reconfigurability of these building blocks will allow for tunable and responsive next-generation materials.

1.4 Final introductory remarks

As we have seen, neither the ability to synthesize and assemble complex particles or phases, nor our ability to simulate them is lacking. Still, a comprehensive framework to predict general assemblies for general building blocks is not in hand. Thus, the focus of this thesis is developing model systems that probe our understanding of how the architecture and interactions of building blocks affect the mesoscale structures they self-assemble.

We will discuss three specific case studies - polymer/nanoparticle composite building-block assemblies, star polymer microdroplets, and amino-acid coated nanoparticles with embedded dipoles that form rods of preferred chirality. In each case study, building-block features - such as the architecture of the block or interactions between the blocks, or pieces of an individual block - are varied in a systematic way. Through varying these blocks and their interactions we demonstrate both enormous diversity in the bulk-scale equilibrium thermodynamic assembly behavior, as well as the ability to tune the morphology and functionality of the resultant self-assembled structures (in our case, droplets and rods). In all cases predictions from simulations are used to either guide building-block assembly or to offer detailed insight into structures that were not previously understood. Additionally, we establish general, domain-agnostic mesophase behavior, as well as hypothesize synthesis and assembly strategies to target highly specific structures for any given application. Where appropriate, text and figures have been taken or adapted directly from our published work; these sections are noted, and guide the reader to the publication for further details.

CHAPTER 2

Model

2.1 Molecular dynamics simulation method

We utilize a minimal coarse-grained model used in previous works to study the phase behavior of our building-blocks.[70, 12, 91, 73] These models vary between cases, as different methods are needed to incorporate all relevant aspects of assembly. We begin with a discussion of relevant forces for capturing immiscibility between building-block components, and the solvent; this lays the ground work for all simulations involving polymer-based building blocks. Next, we discuss the Discrete Element Method, our method for incorporating particle shape in MD simulations that is adapted from the granular materials community. Additionally, we address two anisotropic potentials that were used in nanoparticle simulations. Finally, we conclude with details on dissipative particle dynamics, which is used for fast, large-scale simulations of pure polymeric systems.

The Lennard-Jones pair potential is used to capture immiscibility in polymer-based simulations; in all cases block portions are immiscible, inducing species to aggregate. A shifted LJ is used to incorporate size differences between polymer beads and nanoparticles. The radially shifted Lennard-Jones pair potential is:

$$V_{\mathrm{ij}}^{SLJ}(r) = 4\epsilon_{\mathrm{ij}}\left[\left(\frac{\sigma_{\mathrm{ij}}}{(r-\delta)}\right)^{12} - \left(\frac{\sigma_{\mathrm{ij}}}{(r-\delta)}\right)^{6}\right] \tag{2.1}$$

The attractive interaction potential, which is applied between nanoparticle pairs of the same type (NP_A-NP_A, NP_B-NP_B), is:

$$U_{\mathrm{ij}}^{attractive}(r) = \begin{cases} V_{\mathrm{ij}}^{SLJ}(r) - V_{\mathrm{ij}}^{SLJ}(r_{\mathrm{cut}}^{SLJ}) & r < r_{\mathrm{cut}}^{SLJ} + \delta \\ 0 & r \geqslant r_{\mathrm{cut}}^{SLJ} + \delta \end{cases} \tag{2.2}$$

The units of interaction strength ϵ_{ij} are $\epsilon_{ij} = 1.0\epsilon$ between all particle pairs, the units of diameter for all beads in the system are $\sigma_{ij} = 1.0\sigma$, $\delta = \frac{D_i - D_j}{2} - 1$ is the magnitude of

the shift (where D_i and D_j are the diameters of beads i and j, respectively), and $r_{cut}^{SLJ} = 2.5\sigma$. This form of the potential assures that there is no softening of the potential when accommodating systems of NPs with different diameters.

For unlike pairs (NP_A-NP_B, NP_A-t, NP_B-t, t-t) we use a shifted Weeks-Chandler-Anderson (SWCA) potential.[92] SWCA is the LJ potential shifted by ϵ and with $r_{\rm cut}^{WCA} = 2^{1/6}\sigma$:

$$U_{\rm ij}^{repulsive}(r) = \begin{cases} V_{\rm ij}^{SLJ}(r) - V_{\rm ij}^{SLJ}(r_{\rm cut}^{WCA}) & r < r_{\rm cut}^{WCA} + \delta \\ 0 & r \geqslant r_{\rm cut}^{WCA} + \delta \end{cases} \tag{2.3}$$

Nanoparticles are bonded to end tether beads with finitely extensible non-linear elastic (FENE) springs:

$$U_{\rm ij}^{FENE}(r) = -\frac{1}{2}kR_0^2 \ln\left[1 - \left(\frac{r_{\rm ij}}{R_0}\right)^2\right] \tag{2.4}$$

with $k = 30\frac{\varepsilon}{\sigma^2}$ as the spring constant and $R_0 = 1.5\sigma$ equal to the maximum allowed separation between the two particles, which avoids artificial tether crossing. Additionally, FENE springs are used to bond individual beads of the tether.

For the TNPs, σ is the individual bead diameter, m is the bead mass, and ϵ is the LJ interaction strength, making the dimensionless time of the system $t = \sqrt{m\sigma^2/\varepsilon}$. Temperature is given by $T^* = k_bT/\epsilon$, and controls the degree of immiscibility of individual particles. The volume fraction, ϕ, of the system is determined by dividing the total excluded volume of all beads by the total volume of the box.

Systems are simulated in an implicit solvent within the NVT ensemble, using Brownian Dynamics[93] (BD), which obviates the need for explicit solvent (and thus reduces the computational workload). Particle trajectories are governed by the Langevin equation, given by

$$m_i\ddot{\mathbf{r}}_{\mathbf{i}}(\mathbf{t}) = \mathbf{F}_i^C(\mathbf{r}_i(t)) + \mathbf{F}_i^R(t) - \gamma_i\mathbf{v}_i(t) \tag{2.5}$$

where m_i is the particle's mass, $\mathbf{r}_i$ is the position, $\mathbf{F}_i^C$ is the conservative force on the particle, $\mathbf{F}_i^R$ is a random force, $\mathbf{v}_i$ is the particle velocity and γ_i is the particle's friction coefficient. The friction coefficient is $\gamma_i = -6\pi\eta a$, where η is the solvent viscosity and a is the particle diameter. $\mathbf{F}_i^C$ is the conservative force established by the SLJ and FENE potential fields. The random force , $\mathbf{F}_i^R$, satisfies the Fluctuation-Dissipation theorem. The combined effect of the friction coefficient, γ, and the random force, $\mathbf{F}_i^R$, is to couple particles to a non-momentum-conserving heat bath.

All simulations are performed using the Highly Optimized Object-oriented Molecular Dynamics (HOOMD)-Blue software package,[94, 23] a GPU-based MD code.

All phases are identified through a combination of visual inspection, diffraction pattern, radial distribution function (RDF), and bond order diagram (BOD) analysis. To obtain unit cells, micelle and network node locations are determined by using Gaussian blurring and thresholding on particle positions. Blurred particle positions are averaged over at least 100 frames, which are dumped every $1000\Delta t$. Micelle and network node locations are then determined by constructing a cluster centroid from the blurred and averaged density grid. Unit cells are then compared to perfect crystal structures for final structure determination. Where possible, system snapshots are rendered with individual nanoparticle beads. In some cases, however, the larger nanoparticle species is rendered as a transparent isosurface, so that ordering in the smaller species is not obscured.

2.1.1 Dissipative particle dynamics

In cases where only polymer beads need to be simulated, but the effects of the solvent are important, we use dissipative particle dynamics (DPD). DPD is an excellent tool for such systems because the pairwise force is purely repulsive and linear, meaning that forces are bounded, allowing for a much larger time step, resulting in faster simulations; additionally, this method is easily parallelized, allowing for very large simulations.[95, 24]

In the DPD model, three forces are applied to each particle at each time step - a conservative, a random, and a dissipative force.

$$F = F_{\mathrm{C}}(r) + F_{\mathrm{R,ij}}(r_{ij}) + F_{\mathrm{D,ij}}(v_{ij}) \tag{2.6}$$

where the forces are given by:

$$F_{\mathrm{C}}(r) = A \cdot w(r_{ij}) \tag{2.7}$$

$$F_{\mathrm{R,ij}}(r_{ij}) = -\theta_{ij}\sqrt{3}\sqrt{\tfrac{2k_b\gamma T}{\Delta t}} \cdot w(r_{ij}) \tag{2.8}$$

$$F_{\mathrm{D,ij}}(r_{ij}) = -\gamma w^2(r_{ij})\left(\hat{r}_{ij} \circ v_{ij}\right) \tag{2.9}$$

and

$$w(r_{ij}) = \begin{cases} (1 - r/r_{\text{cut}}) & r < r_{\text{cut}} \\ 0 & r \geq r_{\text{cut}} \end{cases} \tag{2.10}$$

The conservative force, F_c, is a purely repulsive force meant to inhibit overlap between particles; the strength of this force is tuned through the coefficient A, allowing particles to be less or more repulsive. A pairwise random force, F_R, mimics the effect of the solvent on the non-solvent beads. The dissipative force, F_D, tunes the effective viscosity of the system by opposing the motion of the particle. Because the forces are applied pairwise, the DPD system is momentum conserving.

2.2 Discrete element method for molecular dynamics

In cases where the nanoparticle shape is crucial[65, 86], we use an adaptation of the discrete element method (DEM), which has been used extensively by the granular materials community to obtain dynamics of anisotropic particles in the past.[96, 97, 98, 99, 100] This method stands alongside similar methods for capturing shape, such as Monte Carlo [101] and event-driven molecular dynamics[102, 103, 104, 90]. In this method, interactions between particles are modeled as interactions between the minimal set of lower-dimensional geometric features which capture the geometric features of the shapes of interest. Here we describe a conservative adaptation of DEM to run in parallel on Graphics Processing Units within the HOOMD-Blue[94] molecular dynamics framework. This section is adapted from our manuscript on the DEM MD model, which is in preperation.[15]

2.2.1 DEM model

Some assumptions must be made about the simulated particles for the method described here to be useful in classical molecular dynamics. First, we assume that the polytopal shapes have been rounded by a sphere or disk of a given radius. This is necessary to smooth the interaction's dependence on particle orientation to be resolvable with a nonzero timestep. Second, we assume that particles interact only through short-range, repulsive forces. These assumptions allow us to approximate interactions between the volumes of particles i and j as interactions between the nearest points of lower-dimensional features in the particles using simple point-point interactions, without integrating over the volumes

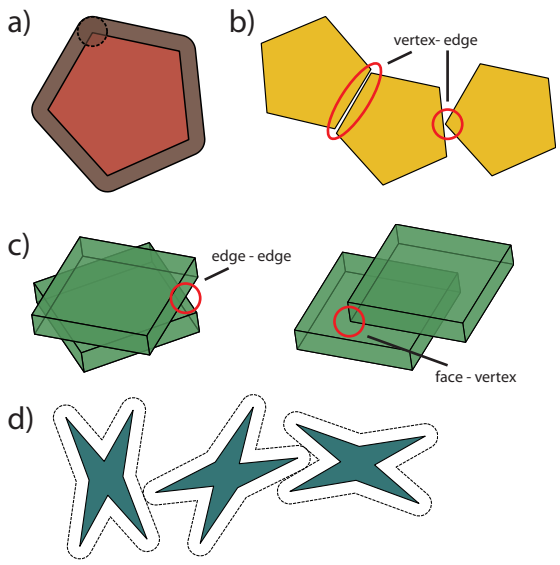

Figure 2.1: *DEM feature checks*: Various checks must be performed against the geometric features of the shape - faces, edges, and vertices. Taken from our DEM manuscript, in preparation.[15]

of the particles. In 2D, it is sufficient to consider interactions between all pairs of vertices and edges between the two particles. In 3D, simulating polyhedral volumes requires interactions between all pairs of vertices and faces and all pairs of edges and edges.

In typical MD a building block is often built up out of stacked or overlapping spheres, which are treated as an individual rigid body; forces are calculated between all pairs of spheres, but translations and rotations are applied to the body as a whole. Within DEM these units are instead built up out of the geometric features of a 2D or 3D polytope: vertices (V), edges (E), and faces (F). Forces and torques are then calculated on the particle due to contributions from all pairs of geometric features; in 3D, the potential energy U_{ij} for particles i and j is defined as

$$U_{ij} = \sum_{E_i \in i, E_j \in j} U(E_i, E_j) + \sum_{V_i \in i, F_j \in j} U(V_i, F_j) + \sum_{V_j \in j, F_i \in i} U(V_j, F_i) \tag{2.11}$$

In 2D these features are reduced to only checks between vertices and edges.

$$U_{ij} = \sum_{V_i \in i, E_j \in j} U(V_i, E_j) + \sum_{V_j \in j, E_i \in i} U(V_j, E_i) \tag{2.12}$$

We evaluate energies, forces, and torques between particles at the closest points be-

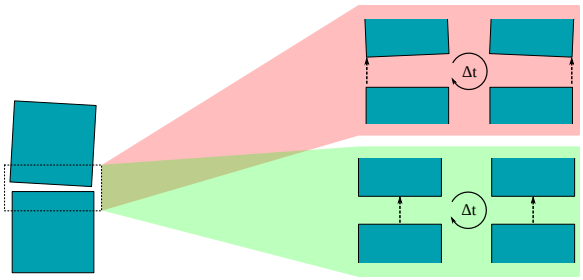

Figure 2.2: *DEM edge-edge instability*: Care must be taken to avoid numerical instability in the edge - edge check. Taken from our DEM manuscript, in preparation.[15]

tween two features due to our approximately hard interaction. This distance can be found using standard point-point, point-line, and point-plane formulae such as those available at http://www.geometrictools.com.

Finally these energies, forces, and torques must be calculated and applied. Because we are simulating nanoscale and colloidal systems, we choose a conservative pair potential that is representative of these energies and well vetted within the community. A shifted and truncated version of the Lennard-Jones (LJ) potential, Weeks-Chandler-Andersen (WCA),[92] creates a steep, purely repulsive force between pairs of features:

$$U_{\mathrm{ij}}^{SLJ}(r) = 4\epsilon_{\mathrm{ij}}\left[\left(\frac{\sigma_{\mathrm{ij}}}{r}\right)^{12} - \left(\frac{\sigma_{\mathrm{ij}}}{r}\right)^{6}\right] \tag{2.13}$$

$$U_{\mathrm{ij}}^{WCA}(r) = \begin{cases} U_{\mathrm{ij}}^{SLJ}(r) - U_{\mathrm{ij}}^{SLJ}(r_{\mathrm{cut}}^{WCA}) & r < r_{\mathrm{cut}}^{WCA} \\ 0 & r \geqslant r_{\mathrm{cut}}^{WCA} \end{cases} \tag{2.14}$$

where $r_{\mathrm{cut}}^{WCA} = 2^{\frac{1}{6}}\sigma$.

For simple system initialization schemes, it is common to encounter collisions of perfectly parallel edges. These collisions introduce a numerical instability for the molecular dynamics integrator: the points of interaction fluctuate at every timestep between the endpoints of each edge, yielding an unstable torque that changes sign at every timestep. To alleviate this issue while still only using point interactions, when two edges are sufficiently close to parallel the interaction point is taken to be the midpoint of overlap between the two edges.

A more common occurrence during simulation is for features to be "overcounted;" for example, when a vertex happens to be the nearest point of contact between two shapes i and j, the interaction is evaluated once for each face in i, once for each face in j, and once for each pair of edges in i and j. This could lead to energetic "bumps" in the inter-

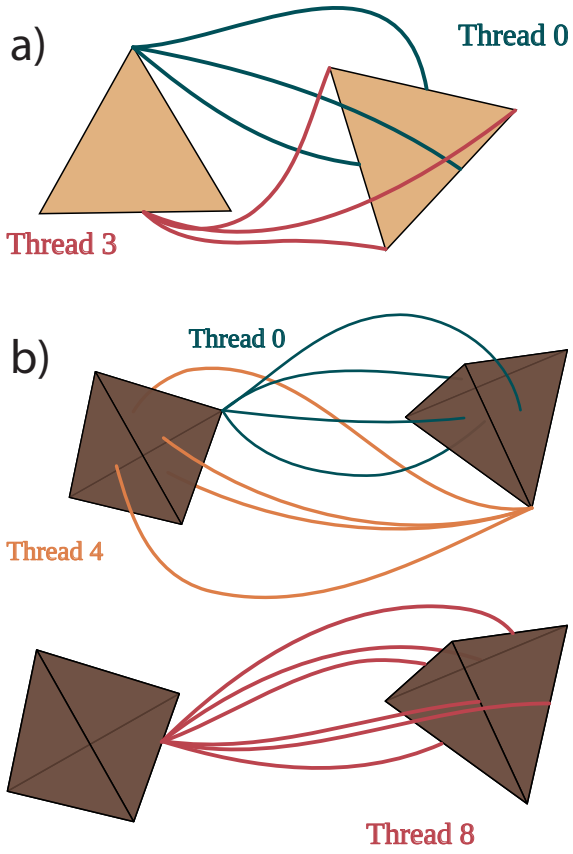

Figure 2.3: *DEM GPU decomposition*: Thread decomposition for the GPU. Taken from our DEM manuscript, in preparation.[15]

action: while the cutoff radius is not affected, the slope of the interaction is increased by some multiplicative factor according to the geometry of the two interacting sites, causing equipotential lines to expand slightly around vertices and edges. This effect should not matter to the extent that the potential used is a good approximation of a "hard" force field. For example, if two cubes are touching perfectly face to face, they will have an interaction strength 36 times as large as a single vertex-face interaction. If the single vertex-vertex interaction had a strength of $1k_BT$, then the $1k_BT$ isosurface for the now $36k_BT$ interaction would have moved out by 9.4% of the rounding radius. Due to the cutoff in the WCA potential, it is impossible for the rounding radius to be increased by more than a factor of $2^{1/6}$ with this overcounting effect.

2.2.2 DEM algorithm

The total force, torque, and potential energy for a given particle is the sum of the force, torque, and potential energy contributions between it and its neighbors. In 2D, two CUDA threads are assigned to each vertex of particle i. The first thread assigned to a given vertex calculates and sums the force, torque, and potential energy contributions between that vertex and the nearest point to that vertex on each edge of each neighboring particle j. The second thread assigned to a given vertex calculates and sums the force, torque, and potential energy contributions between the nearest point on the edge beginning at that vertex in particle i to each vertex in each neighboring particle j.

In 3D, two CUDA threads are assigned to each vertex of particle i and one thread is assigned to each edge of particle i. The first vertex thread calculates the interaction between that vertex and the nearest point to each face in each neighboring particle j. The second vertex thread calculates the interaction between that vertex in each neighboring particle j and the nearest point of each face of particle i. The edge thread calculates the interaction between the nearest point on its edge of particle i to each edge of each neighboring particle j.

2.3 Anisotropic potentials

2.3.1 Dipole potential

To model interactions between particles that have a net dipole charge, we use a model from previous studies.[34, 32, 36] The energy between pairs of interacting particles is:

$$
\begin{aligned}
U_{ij} = \frac{q_i q_j}{4\pi\epsilon_0\epsilon r_{ij}} e^{-kr_{ij}} C_0^2 + \\
\frac{q_i\mu_j cos(\theta_j) + q_j\mu_i cos(\theta_i)}{4\pi\epsilon_0\epsilon r_{ij}^2} e^{-kr_{ij}} C_0 C_1 + \\
\frac{\mu_i\mu_j}{4\pi\epsilon_0\epsilon r_{ij}^3}\big\{cos(\theta_i)cos(\theta_j)[2 + kr_{ij} + (kr_{ij})^2] + \\
sin(\theta_i)sin(\theta_j)cos(\phi_i - \phi_j)[1 + kr_{ij}]\big\} e^{-kr_{ij}} C_1^2
\end{aligned}
\tag{2.15}
$$

with

$$
C_0 = \frac{e^{ka}}{1 + ka}
$$

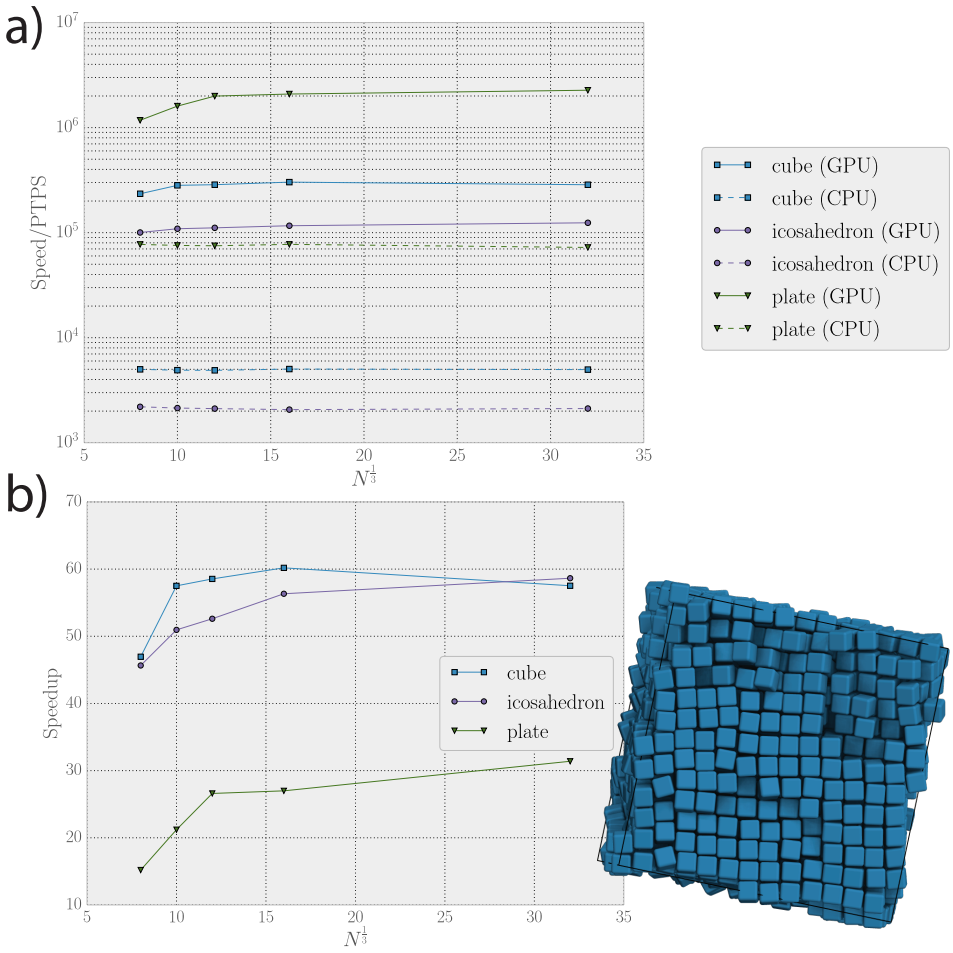

Figure 2.4: *DEM algorithm performance*: Performance of the DEM MD implementation over system size for various shapes. Taken from our DEM manuscript, in preparation.[15]

and

$$C_1 = \frac{3e_{ka}}{2 + 2ka + (ka)^2 + \epsilon_0(1+ka)/\epsilon}$$

where q_i and q_j is the charge carried by particle *i* and *j*, μ_i and μ_j are the dipole moments, r_{ij} is the distance between particle centers, θ_i and θ_j are the angles of the dipole vector with respect to the vector connecting the centers of the particles, ϕ_i and ϕ_j are dihedral angles that describe the relative orientation of the dipoles, ϵ_0 is the permittivity of free space, ϵ is the permittivity of the solvent, and a is the radius of the nanoparticle.

2.3.2 Chiral potential

In one study, we choose to apply a chiral bias, or "twist", between interacting faces of tetrahedral nanoparticles. Two particles i and j that are within range to interact (their centers of mass are within some cuttoff distance) iterate through their faces, and impose a "twist" to pairs of interacting faces. So, each particle must iterate between all pairs of faces 1-1, 1-2, 1-3, 1-4, ..., 4-4. The applied potential $\mathbf{V}(\mathbf{r})$ is chosen to be purely repulsive, as well as smooth and differentiable everywhere.

$$V(r) = \epsilon * (1 - \frac{r}{\lambda})^{\frac{5}{2}} \tag{2.16}$$

$$\frac{dV(r)}{dr} = -\frac{5}{2}\frac{\epsilon}{\lambda} * (1 - \frac{r}{\lambda})^{\frac{3}{2}} \tag{2.17}$$

The normal of face i on particle 1 is given by $\hat{z}_i^{'(1)}$ and the normal of face j on particle i is $\hat{z}_j^{'(2)}$. Primes indicate that the coordinates of the feature have been rotated into the body frame of the particle. Face directions are given by $\hat{w}_i^{'(1)}$ and $\hat{w}_j^{'(2)}$; these directions are reference points for calculation of the chiral potential, with the angle between these two directions determining the amount of "twist". A modulation $\xi \sim sin(3\theta) = 3sin(\theta) - 4sin^3(\theta)$ is applied between pairs of interacting faces. The form of this modulation is -

$$\xi_{ij} = \frac{1}{2}(\hat{w}_i^{'(1)} \times \hat{w}_j^{'(2)}) \cdot (\hat{z}_i^{'(1)} - \hat{z}_j^{'(2)}) \tag{2.18}$$

This modulation has the effect of destabilizing face to face contacts, instead encouraging faces to twist with respect to one another. This results in an effective potential -

$$V_\xi^{\pm}(r, w_i^{(1)}, w_j^{(2)}) = \pm V(r) \cdot (3\xi - 4\xi^3) \tag{2.19}$$

where the total Force from particle i to particle j is given by -

$$F_{12} = \pm \sum_{ij} \frac{dV_{ij}}{dr_{ij}} \frac{1}{r_{ij}} (\vec{r}_{12} + c_i^{'(1)} - c_j^{'(2)})(3\xi_{ij} - 4\xi_{ij}^3) \tag{2.20}$$

CHAPTER 3

Complex Structures formed by Tethered Nanoparticle Building Blocks

Tethered nanoparticles are best thought of as a conceptual framework that allows for tuning domain properties on nearly every scale.[51] These TNPs create a spectrum of mesoscopic assemblies, such as: 1) pseudo - 2D assemblies (e.g. lamellae), 2) micellar structures adopting BCC, Frank-Kasper, or quasicrystalline patterns, and 3) complex diamond, gyroid, or other networks. In this section, we highlight a collection of such phases assembled in two different classes of tethered nanoparticles - "telechelics" and "giant surfactants". While a TNP "telechelic" shares more in common with triblock co-polymers, the TNP "giant surfactant" is best thought of as large surfactant molecule, as its name implies.

In both cases of TNP simple geometric changes are made to the building-block - the length of the polymer tether in both cases, and the size ratio of the two nanoparticle end-groups for the telechelic. These small changes to the block result in dramatic changes in the equilibrium morphology for a given set of thermodynamic conditions. For the telechelic, phases ranging from sheets to networks emerge; the giant surfactants form a variety of micelle phases, including Frank-Kasper phases[17]. The results of our TNPT have been published, and are reproduced here; further information can be found in "Marson, R. L.; Phillips, C. L.; Anderson, J. A; Glotzer, S. C. *Nano letters* 2014, 14, 2071-2078".[16]

3.1 Tethered nanoparticle telechelics

In the case of TNP Telechelics NPs are modeled as beads of diameter 1.0σ, 2.0σ, 3.0σ, or 4.0σ; tethers are modeled as chains of beads of diameter 1.0σ, which is the persistence length of a polymer segment. We consider NPs of a single TNPT to be generally two different particle types, as shown in Figure 3.1a). To mimic immiscibility between NPs, those of the same type have an attractive interaction, while all other interactions are volume excluding. To model interactions we use a radially shifted Lennard-Jones (SLJ) potential, which

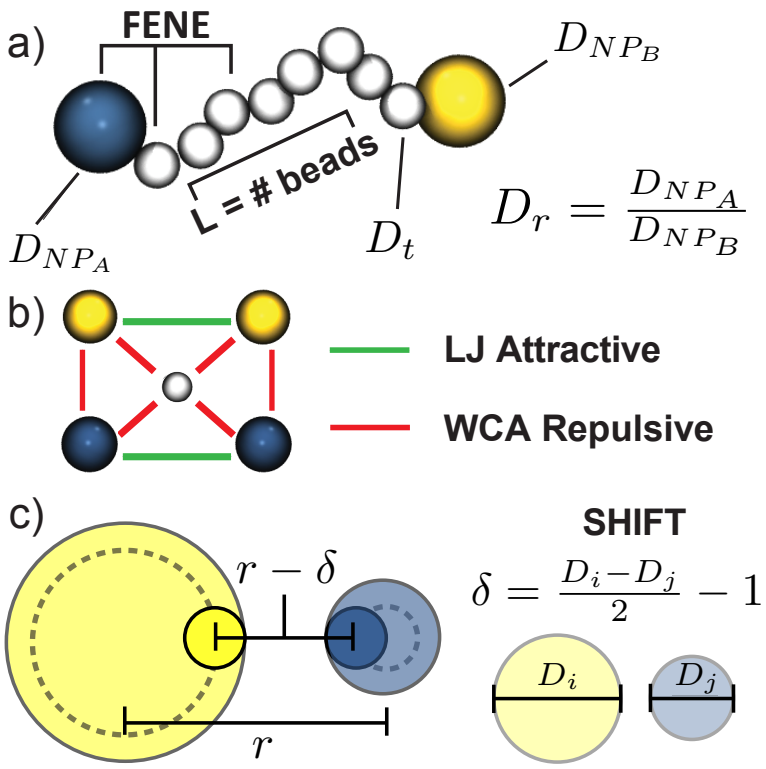

Figure 3.1: *The TNPT model*: (a) Four different nanoparticle lengths are explored: L = 2, 4, 6, and 8 beads. For each choice of L, three different diameter ratios are used: $D_r = \frac{D_{NP_A}}{D_{NP_B}} = 1.0, 0.6$, and 0.5. (b) NPs interact with like species via a SLJ potential. A shifted WCA models a repulsion between unlike species. The nanoparticle is bonded to a tether bead by a FENE spring; additionally, tether beads are also connected by FENE springs. (c) Description of the shifted LJ and WCA potentials. The potential is shifted by δ and evaluated at a distance $r - \delta$. Figure reproduced from publication.[16]

shifts the potential to the surface of the particle. Figure 3.1b) illustrates the interactions between particle types.

Simulations are initialized with $N = 1000$ TNPTs randomly placed in a periodic, cubic box. The system is randomized by raising the temperature well above the order-disorder transition temperature, $T^* >> T^*_{ODT}$, for 10 million time steps. All simulations begin dilute, and are compressed to the desired volume fraction over 10^4 time steps by uniformly scaling the box dimensions. The system temperature is lowered by $\delta T^* = 0.05$, and run for 20 million time steps at each increment, to a final temperature of $T^* = 0.25$. All simulations use a time step $\Delta t = 0.005\sqrt{m\sigma^2/\varepsilon}$. Each simulation is repeated 10 times with different random initial conditions.

The simulated nanoparticles (NP) are assigned a diameter $D_{NP} = 1\sigma$, 2σ, 3σ, or 4σ. In all figures the smaller nanosphere is labeled nanoparticle A (NP_A) and colored blue; the larger is labeled nanoparticle B (NP_B) and colored yellow. We simulate three nanoparticle diameter ratios - $D_r = \frac{D_{NP_A}}{D_{NP_B}} = 1.0, 0.67$, and 0.5 - and four tether lengths - $L = 2, 4, 6$, and 8 beads of diameter 1σ. Every system was simulated at volume fractions $\phi = 35\%, 40\%, 45\%$, and 50%; additionally, where noted, some cases were investigated at lower volume fractions. Each temperature schedule represents at least ten separate simulations. All phases reported occurred in three or more of the ten independent simulations. Each phase contains at least two unit cells per box direction (8 total unit cells), aside from the $Ia\bar{3}d$ and $Fddd$ networks, which contain one unit cell.

We report several phases that are new to the TNP design-space, and identify new analogs to several structures that have been previously reported in TNP simulations where the building blocks are comprised of a single NP and one or two tethers. [70, 72, 80, 12, 73, 91] Figure 3.2 shows a phase diagram of the observed structures. Two phases - BCC spherical micelles and tetragonal long micelles - that were found for parameters that fell outside the parameter range of Figure 3.2.

3.1.1 Micelle in network phases

3.1.1.1 $\beta - Sn$ micelles in network $-$

For tether lengths of L = 6 and L = 8, at $\phi = 35\%$ and $D_r = 0.5$, the TNPT assembles a $\beta - Sn$ (with an elongated c-axis) phase, as shown in Figure 3.3a. Figure 3.3b shows the particle centroids extracted by Gaussian filtering and the BOD of the nearest neighbor centroids. The centroid diffraction pattern is shown from two different symmetry axes, Fig. 3.3c (left), and compared to the diffraction pattern of an ideal $\beta - Sn$ crystal structure, Fig. 3.3c (right).

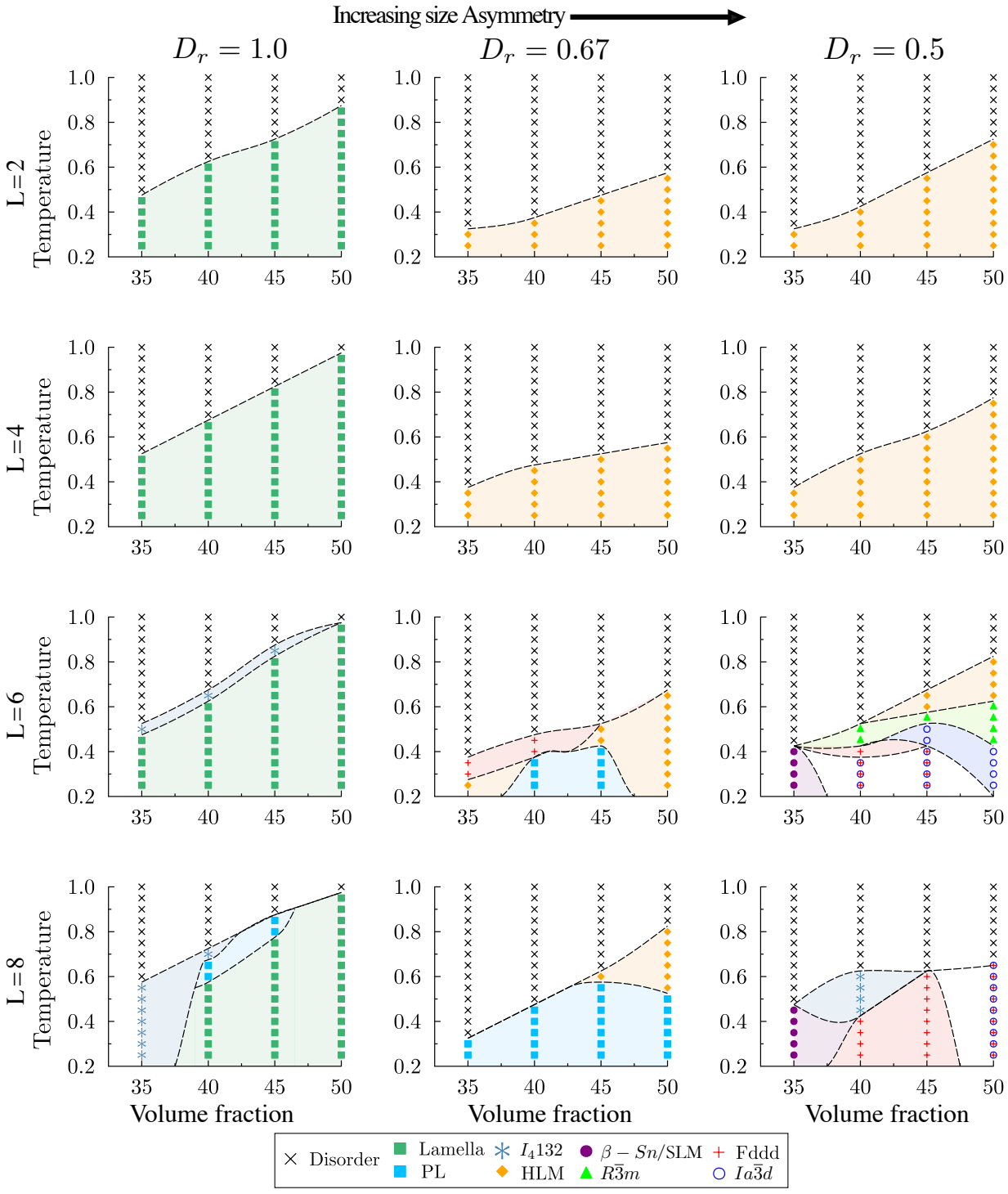

Figure 3.2: *Phase diagram.* At top, each of the three diameter ratios (D_r) are listed from most to least size-symmetric; tether length (L) increases from top to bottom. Each diagram contains a listing of phases found between 35% and 50% volume fraction (ϕ), over a wide temperature range. Regions are shaded and separated with dotted lines to guide the reader. Overlapping symbols indicate multiple stable phases in a region. Figure reproduced from publication.[16]

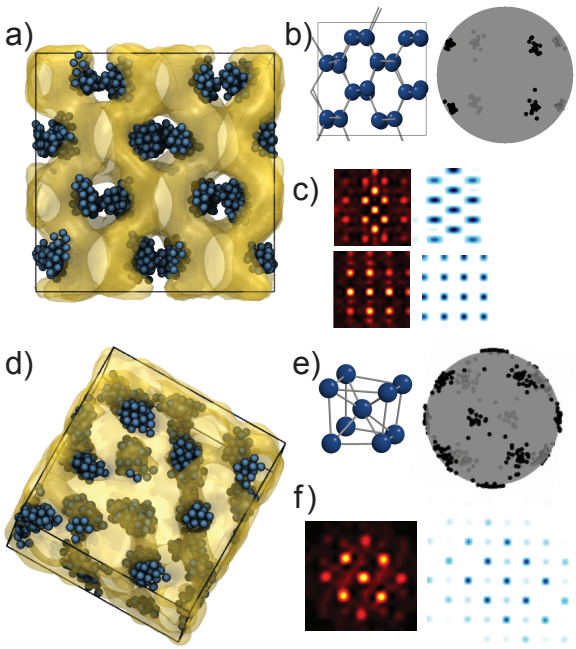

Figure 3.3: *Micelle Phases*. (a) $\beta-Sn$ micelles. (b) (left) The micelle centroids and (right) a BOD for the nearest neighbor centroids. (c) The diffraction pattern of the centroids (left) and an ideal $\beta-Sn$ crystal. (d) BCC micelles. (e) A unit cell constructed from the micelle centroids and a BOD for the nearest neighbor centroids. (f) The diffraction pattern of the centroids (left) and an ideal BCC crystal. Figure reproduced from publication.[16]

In this phase, NP_A form spherical micelles that decorate a $\beta - Sn$ lattice, while NP_B form a continuous $\beta - Sn$ network. As is characteristic of the $\beta - Sn$ crystal structure, the micelles are offset (do not lie on the same line) and alternate through the crystal structure from two symmetry axis. Because this $\beta - Sn$ phase has an elongated c-axis the BOD does not indicate neighbors at the north and south "poles", as would be found for the BOD of an ideal $\beta - Sn$ crystal structure. NP_B forms a continuous network phase that surrounds the micelles. This phase is the tetragonal analog to the diamond crystal, compressed in the "c" direction; the ideal $\beta - Sn$ crystal structure is further compressed in the "c" direction. The network phase is shown as a yellow transparent isosurface in Figure 3.3a.

3.1.1.2 *BCC micelles in network* –

For tether lengths of L = 2 at $\phi = 30\%, 35\%, 45\%$, and L = 4 at $\phi = 45\%$, with $D_r = 0.5$ the TNPT assembles a body centered cubic (BCC) micelle phase, shown in Figure 3.3d. This data is not shown in Figure 2, as this phase was found in a small set of simulations where, despite the same ratio of 1/2, the absolute sphere sizes are twice as big ($D_r = \frac{2\sigma}{4\sigma}$, instead of $\frac{1\sigma}{2\sigma}$).

In the BCC phase NP_A beads form micelles, which decorate a BCC lattice. Figure 3e shows a BCC unit cell extracted from the simulation data and the BOD of the micelle centroids. The diffraction pattern of the four-fold axis of the centroid is shown in Figure 3f (left), along with the diffraction pattern of a perfect BCC crystal structure. NP_B form a network that surrounds the lattice. The network phase is shown as a yellow transparent isosurface in Figure 3.3d.

3.1.2 Network phases

3.1.2.1 *Gyroid networks* –

The TNPT assembles two types of gyroid structures, the alternating gyroid (AG) and the double gyroid (DG).

The AG forms at tether lengths of L = 6 for $\phi = 35\%, 40\%, 45\%$ as well as at L = 8 for $\phi = 35\%, 40\%$ for $D_r = 1.0$. The AG is also found for $\phi = 40\%$ at L = 8 and $D_r = 0.5$. The AG has symmetry $I4_132$ (No. 217) and is composed of two interpenetrating gyroid networks of opposite chirality composed of NP_A and NP_B respectively, as shown in Figure 3.4b. The polymer tether fills the dividing space between the two networks. The NP_A and NP_B domains are shown on the top and bottom right of Figure 3.4d, respectively. Within a single gyroid network, three edges of the network connect at a node. Nodes connected by

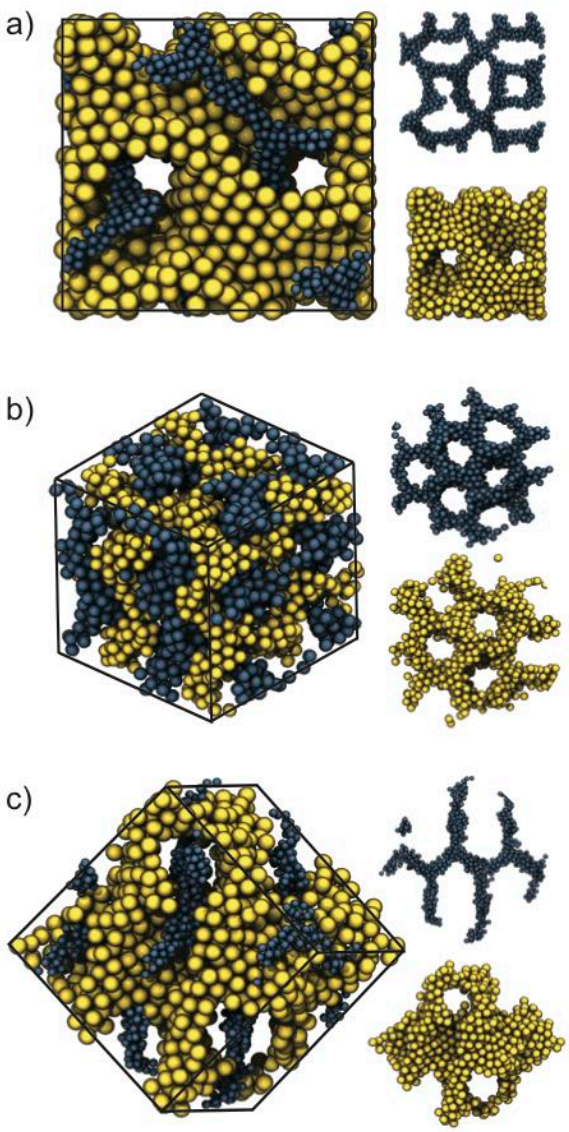

Figure 3.4: *Network Phases*. Three network structures. (a) $Ia\bar{3}d$ (Space group No. 230) Double Gyroid. (b) $I4_132$ (Space group No. 214) Alternating Gyroid. (c) $Fddd$ (Space group No. 70) Fddd network. Figure reproduced from publication.[16]

an edge are rotated 70.5 degrees relative to each other.[26] The nodes formed in both the NP_A and NP_B gyroid can be seen on the right of Figure 3.4b.

The DG forms for tether lengths of L = 6 at $\phi = 40\%, 45\%, 50\%$ and for L = 8 at $\phi = 50\%$ at $D_r = 0.5$; it is shown in Figure 3.4a. In contrast to the AG, in the DG both halves of the interpenetrating gyroid network are composed of NP_A (Fig. 3.4a, top right), and are surrounded by the tether. Thus, the DG of symmetry $Ia\bar{3}d$ (No. 230) has an inversion symmetry that the AG does not. The NP_B (Fig. 3.4a, bottom right) forms the minimal surface that divides the two gyroid networks.

Per Figure 3.2, at L = 6, there is an order-order phase transition between the DG and either the HLM or $R\bar{3}m$ network, but at L = 8 the DG forms spontaneously from a disordered system. In all regions except for L = 6 at $\phi = 50\%$, the DG competes for stability with the Fddd network (section 3.2.2).

3.1.2.2 *Fddd network* –

An Fddd network phase (space group No.70) forms at tether length L = 6, $\phi = 35\%$ and 40% for $D_r = 0.67$, and at $\phi = 40\%$ for $D_r = 0.5$. At a tether length of L = 8, the $Fddd$ network forms at $\phi = 40\%, 45\%$, and 50% for $D_r = 0.5$.

As shown in Figure 3.4e, NP_A form a continuous network where three edges meet at each node; each node and edge group lie in the same plane. Two of the edges connect to a node with edges in the same plane, while the third edge connects to a node rotated into a new plane. This pattern of node connections combines the patterns of the PL (same plane) and DG/AG (different plane) network structures. [26] NP_B forms a surface that surrounds the network. The NP_A and NP_B domains are shown on the right of Figure 3.4e.

Per Figure 3.2, at $D_r = 0.67$ there is an order-order phase transition between the $Fddd$ phase and PL or HLM. At $D_r = 0.5$, there is an order-order phase transition between the $Fddd$ phase and $R\bar{3}m$. In several regions the $Fddd$ network competes for stability with the DG.

3.1.3 Long micelle phases

3.1.3.1 *Tetragonally arranged, alternating long micelles* –

For a tether length of L = 8 at $\phi = 25\%$, $D_r = 1.0$, the TNPT system forms a tetragonal packing of long cylindrical micelles (TLM). This phase was found in a small set of simulations outside the range shown in Figure 3.2. This was the only ordered phase observed for $\phi < 35\%$.

In this phase, both NP_A and NP_B form long micelles, as seen in Figure 3.5f. The LM arrange tetragonally, rather than hexagonally, and alternate NP_A and NP_B. The polymer tether fills the space between the LM.

3.1.3.2 *Hexagonally arranged, long micelles* –

For a tether length of L = 2 and 4, $\phi = 35 - 50\%$, $D_r = 0.67$ and 0.5, the TNPT system forms hexagonally arranged long micelles (HLM). The phase also forms for a tether length of L = 6, $\phi = 35\%, 45\%, 50\%$ and L = 8, $\phi = 45\%$ and 50%, for $D_r = 0.67$, and L = 6, $\phi = 45\%$ and 50%, for $D_r = 0.5$.

In the HLM phase, NP_A form LMs that are hexagonally arranged, as shown in Figure 3.5b. The tethers form a shell around the LMs. NP_B forms a honeycomb shaped bilayer around the LM. As the tether increases in length, the shell formed around the LM becomes thicker.

As seen in Fig. 2, for L = 2, and L = 4, $D_r = 0.67$ and 0.5, HLM was the only stable phase found. At L = 6 and 8, there is an order-order phase transition between HLM and PL phases, the $Fddd$ network, and $R\bar{3}m$.

3.1.3.3 *$R\bar{3}m$ micelles* –

A network phase of space group $R\bar{3}m$ (space group No. 166) forms at a tether length L = 6 at $\phi = 40\%, 45\%, 50\%$, $D_r = 0.5$.

Within this phase, NP_A forms a weaving long micelle type structure. These structures have nearly straight sections that weave around the surface formed by NP_B, forming distinct "kinks" followed by persistent straight sections. The effect of these kinks is to create a distinct "square-wave"- like long micelle, as shown in Figure 3.5e. This structure shares the same space group with hexagonally perforated lamellar structures of type ABC packing (HPL_{ABC}), but is a different structure.[105]

3.1.3.4 *Honeycomb with spherical & long micelles* –

For tether lengths of L = 6 and L = 8, at $\phi = 35\%$, and $D_r = 0.5$ the TNPT assembles a Honeycomb with Spherical and Long Micelle (HC/SLM) phase , as shown in Figure 3.5d. This phase forms in the same region of the phase diagram, for the same thermodynamic parameters, as the $\beta - Sn$ micelles.

In this phase NP_B forms a honeycomb-like structure with lateral perforations that are perpendicular to the long axis of the honeycomb. NP_A forms a set of alternating spherical and long micelles; long micelles sit in the center of HC cells, while spherical micelles

occupy the lateral perforations. The tether forms a shell around the micelles, filling the space between NP_A and NP_B.

3.1.4 Lamellar phases -

3.1.4.1 $Lamellae$ $-$

For $D_r = 0.5$ lamellar (LAM) sheets are the most prevalent structure. At tether lengths L = 2 and L = 4 this is the only ordered phase present at all ϕ. For L = 6 the AG forms at intermediate T^*, with a LAM configuration stable at low T^*. At the longest tether length, L = 8, LAM structures form at intermediate to high T^*, remaining stable throughout the simulation.

The LAM structure is composed of two nanoparticle domains that each form a layer spanning the length of the box. An example of this type of structure is shown as the equilibrated phase in Figure 3.5a. Nanoparticle domains alternate in chemical specificity. The spacing between layers in the LAM structure is determined by the length of the polymer tether; increasing tether length increases the spacing between layers.

3.1.4.2 $Perforated\, lamellae$ $-$

Perforated lamellae (PL) form for $D_r = 0.67$ at both the L = 6 and L = 8 tether lengths. In the L = 6 tether length case, HPL form at $\phi = 40\%$, and 45% for low T^*. Increasing the tether length to L = 8, we also see a prevalence of PL structures forming at $\phi = 35\%, 40\%, 45\%$, and 50%; here the HPL form at intermediate T^*.

In this phase, NP_A forms a set of lamellar sheets with perforations. NP_B forms a honeycomb-like structure that surrounds the PL. This HC structure contains lateral perforations, which accommodate the PL. This phase neighbors the HLM phase because of their structural similarity, where the PL phase is a higher density structure with connections that develop between like nanoparticle species. For NP_A, these connections occur between tubes, laterally, to become PL; for NP_B, layers connect vertically to form a HC-like structure.

3.1.5 Discussion

The TNPT design space contains the same set of structures found in linear triblock copolymer systems. All linear TBCP phases reported as equilibrium or metastable phases in the literature[26] appear in our phase diagram, including: BCC micelles, hexagonal tubes,

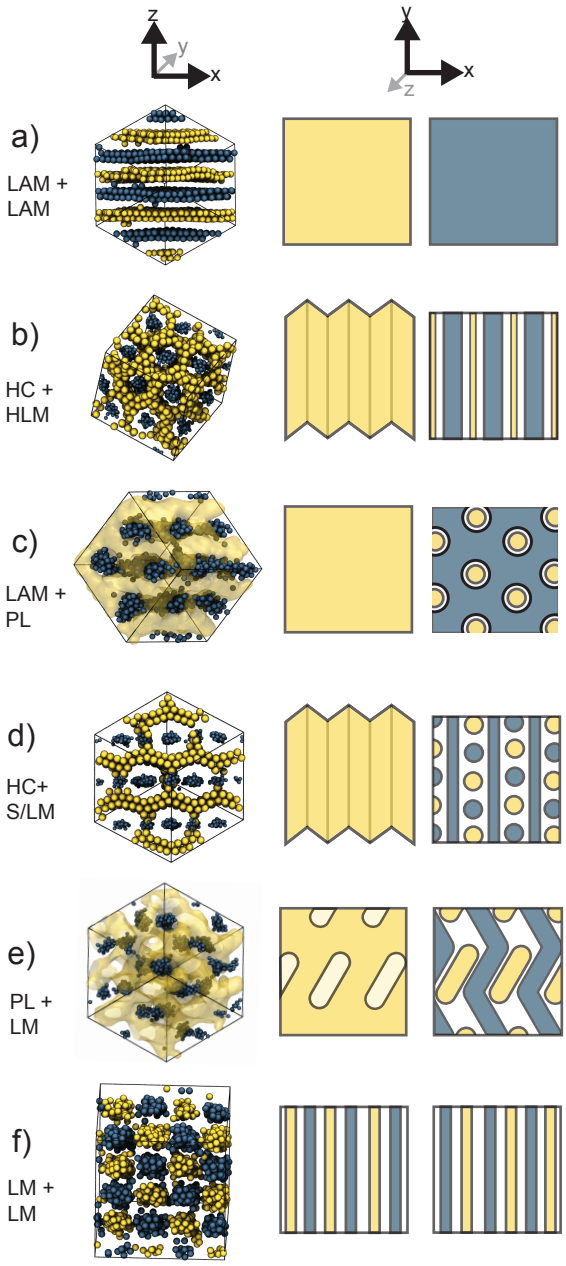

Figure 3.5: *LAM, PL, and LM phases*. The left column shows simulations results for the following phases: (a) lamellar phase, (b) honeycomb plus long micelle phase, (c) lamellar plus perforated lamellar phase, (d) lamellar plus short/long micelle phase, (e) ($R\bar{3}m$) perforated lamellar plus long micelle phase, and (f) tetragonally arranged long micelle phase. The middle and right column illustrate neighboring cross-sections of the phase. Figure reproduced from publication.[16]

tetragonal alternating tubes, both AB and ABC stacked perforated lamellar sheets, standard lamellar sheets, the $Fddd$ structure, and both alternating ($I4_132$) and double ($Ia\bar{3}d$) gyroids. [106, 107, 108, 109, 26, 110] This is significant in that it predicts that NPs, from a variety of materials, can take the place of the usual polymer end blocks while maintaining the same phase diversity.

Symmetry (or asymmetry) in the size of the NP end groups usually results in the assembly of microphases that are likewise symmetric (or asymmetric) with respect to the end groups. For $D_r = 1.0$, we find only symmetric phases, that is, phases invariant to exchanging the two end groups. These phases are tetragonally arranged long micelles, the AG, and AB lamellar sheets. As an example, in the AG, each of the two interpenetrating chiral networks of the gyroid is composed of a single nanoparticle species. For $D_r = 0.67$ and $D_r = 0.5$, all phases found are asymmetric with respect to the end groups. Thus, for the DG, a single end group now forms both chiral networks of the gyroid; the other, larger, end group forms the minimal surface that divides the space between interpenetrating networks. The single exception is an AG that forms with $D_r = 0.5$ for L = 8 at $\phi = 40\%$. In this case, the volume fractions of the two end groups are asymmetric. However, this phase is only present at high T where the effective volume of the smaller nanoparticle domain is larger due to large thermal fluctuations. At low T^*, the system stabilizes an $Fddd$ phase, which is again asymmetric with respect to the end groups.

Increasing the length of the polymer tether provides the TNPT system with the configurational freedom necessary to adopt an increasing number of complex phases. At short tether lengths, we find only a single ordered phase at each diameter ratio - lamellar sheets for $D_r = 1.0$ and hexagonally arranged long micelles in a honeycomb network for $D_r = 0.67$ and $D_r = 0.5$. TNPT with short tethers are effectively floppy dimers and form phases similar to those observed in sets of asymmetric, softened dumbbells.[89] At longer tether lengths, several micelle and network phases are present. We also observe order-order transitions, suggesting the configurational entropy added by the longer tether is a significant contribution to the free energy. Also, more of the phases seen in triblock copolymer system are observed in this part of the TNTP phase diagram.[26]

The most complex region of the phase diagram occurs where the diameter ratio is the most asymmetric ($D_r = 0.5$) and the tether length is moderately long (L=6). Throughout the assembly process the system must balance constraints imposed by asymmetry in phase behavior due to nanoparticle size asymmetry and configurational freedom provided by the tether. In this region the system is best able to balance these constraints, driving the assembly of complex structures.

The $\beta - Sn$ micelle in network phase of section 3.1.1, the $R\bar{3}m$ long micelles of sec-

tion 3.3.3, and the honeycomb with spherical and long Micelles of section 3.3.4 have not been reported in the triblock copolymer literature to our knowledge. In linear triblock copolymers, the only micelle phase reported is BCC.[26] All three phases occur at the most asymmetric diameter ratio, $D_r = \frac{1\sigma}{2\sigma} = 0.5$. We found that maintaining the same diameter ratio, but doubling the volume of the end groups, produces a BCC micelle in network phase instead. Both the $R\bar{3}m$ and HC/SLM are mixed lamellar - micellar morphologies

In several cases, we see competition between two phases in regions of the phase diagram. This occurs due to small differences in free energy between related phases. The perforated lamellar phases, for example, have been proposed to be kinetically arrested, metastable precursors to continuous network phases, for both block copolymer[111, 112, 113] and TNP systems[84, 72]. The $Fddd$ and $Ia\bar{3}d$ gyroid are, similarly, known to be very close in free energy.[114] Our simulations were run for tens of millions of time steps for each temperature value reported, but this does not guarantee that the system will find the free energy minimizing structure. Moreover, it is possible that even stable structures can fluctuate out of equilibrium at higher temperatures and not fluctuate back over the duration of a simulation. Deciding which structures are the true equilibrium structures, however, is not the goal of the present study. Rather, we aim to qualitatively understand how tethering can be used as a tool for the creation of complex self-assembled structures.[28] Thus, we report both stable and robust metastable phases, mindful that metastable structures are desirable[115] or can be important precursors in kinetic transitions to more complex structures like the gyroids.[105, 72, 116]

Our simulations predict that, compared to BCPs, the effect of replacing polymer blocks with NPs has two significant effects. First, the conformational entropy of the end group is reduced.[70, 12] Second, when the NPs are confined to an end-group domain of a microphase-separated system, the local packing of the NPs induces order. Microphase separation promotes local icosahedral packing for spherical NPs, for example. [117, 72] As a result, TNP systems can have additional ordering not found in polymer microphase separated systems. By varying the geometry of the NPs, it may be possible to realize different types of ordering in the NP domains that may impact the stability of different microphase structures. This is an area for future study.

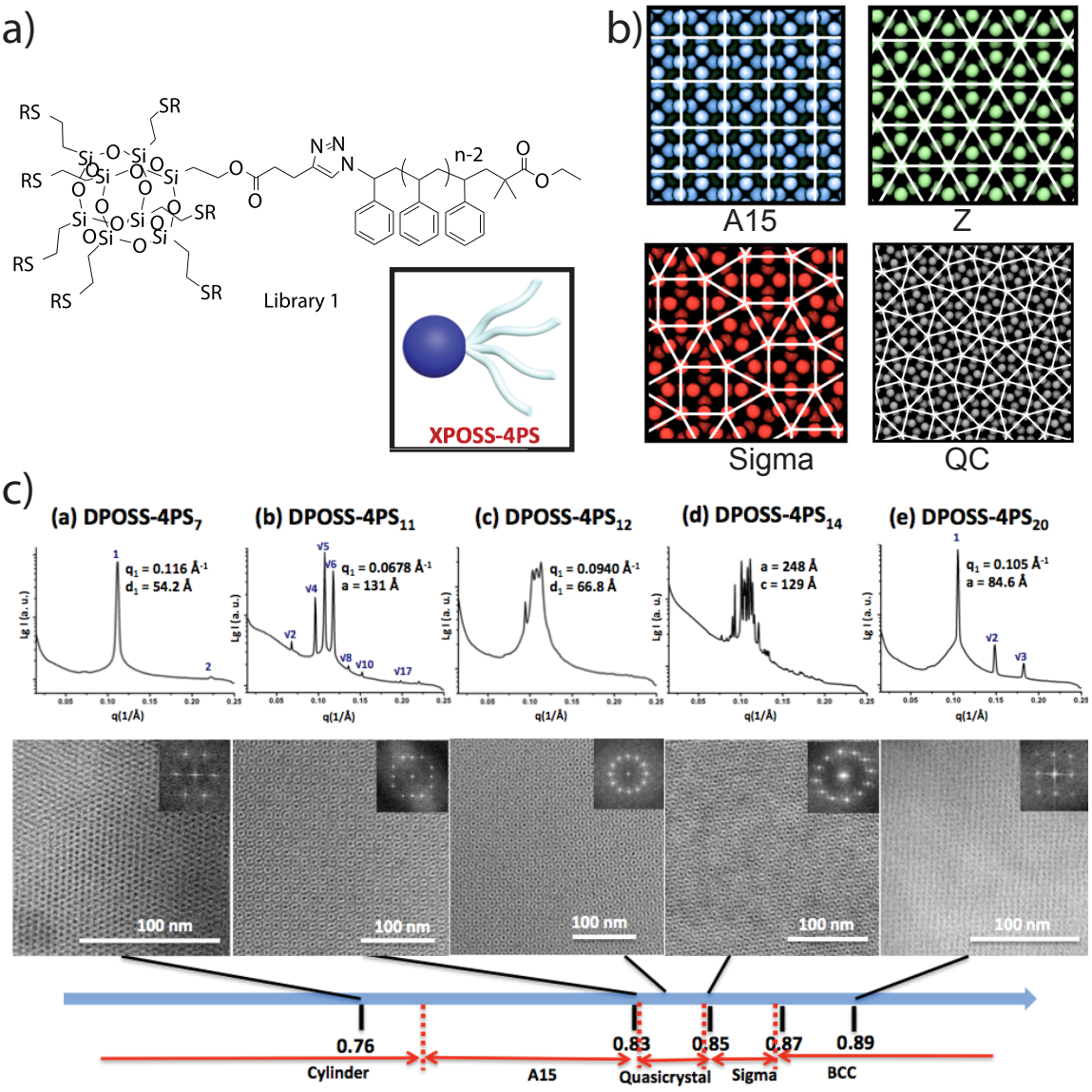

Figure 3.6: *Experimental information on DPOSS-4PSn TNP*. Details on the DPOSS-4PSn building block and assembly. (a) The chemical structure of a DPOSS-PSn molecule. A cartoon of the DPOSS-4PSn molecule is inset. (b) Frank-Kasper A15 and Z phases, the Sigma phase, and a dodecagonal quasicrystal, from Iacovella et al.[17] (c) An experimental phase diagram generated from the DPOSS-4PSn molecule, based on varying the tether length.

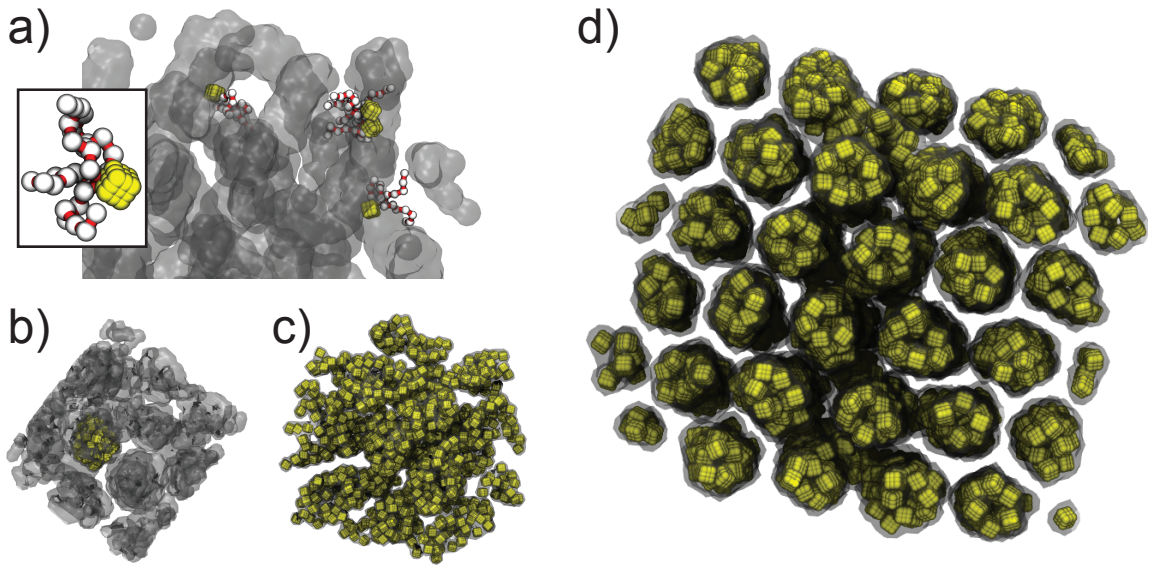

Figure 3.7: *DPOSS-4PSn simulation details*. Simulation information about the assembly of the DPOSS-4PSn building-block. (a) Initial assembly steps show POSS aggregates as an isosurface (gray). Inset shows an individual block, with POSS molecules colored yellow, PS tethers white, and bonds red. (b-c) Micelles formed by aggregated POSS head groups. (d) Hexagonal long-micelles formed by $L = 4, 6$ tether lengths of DPOSS-4PSn.

3.2 Tethered nanoparticle DPOSS-4PSn - a "giant surfactant"

The ability to synthesize a a variety of different TNPs has increased dramatically in recent years. Through "click" chemistry[53] researchers are able to create many classes of complex nanoparticle "atoms" and "molecules"[118]. Cheng et al. report the synthesis of numerous classes of these building blocks[119, 120, 121, 122, 118], including a subset of TNPs they refer to as "giant surfactants"[59].

We will discuss the assembly behavior of a particular building block taken from their classification scheme[59]. By attaching a polystyrene (PS) tether to a polyhedral oligomeric silsesquioxane (POSS) molecule they create a giant surfactant molecule, DPOSS-4PSn. The integer "n" is determined by the degree of polymerization of the PS tail, thus indicating the length of the tail; the number 4 referring to the fact that four PS tethers are attached at a single vertex of the cube-like POSS molecule. The chemical structure of single tailed DPOSS-PS molecule is shown in Fig 3.6a), with a 4-tailed cartoon shown as inset.

The DPOSS-4PSn molecule has a rich assembly behavior, which is shown in Fig. 3.6c). The building block transitions from Hexagonal tubes to a variety of micelle structures, in-

cluding Frank-Kasper phases and a dodecagonal quasicrystal (DQC). Figure 3.6b) highlights several of these phases, demonstrating how micelles formed by TNPs can arrange on each lattice. As described by Iacovella et al.[17] these phases form in TNP and related systems due to the interplay between shape polydispersity (in the form of micelles of different size and asphericity) and particle functionalization (in the form of soft, squishy coronas formed by the tether or nanoparticles). In the case of DPOSS-4PSn, the POSS molecules form the colored domains (blue, green, red, and gray), while the PS tethers fill the dark space in between. This is evident in the TEM micrographs taken from experiment, shown in Fig. 3.6c); here, the colors are inverted, dark domains are POSS molecules and white-space is PS tether.

Molecular Dynamics simulations are used to study the generality of this assembly behavior, as well as corroborate experimental data. The model for this study was adapted from previous studies of tethered nanoparticles. The POSS head groups are modeled as rigid bodies, created from overlapping 3 spheres along each side; the side length was chosen to be $.84\sigma$, the distance between the two corner spheres. Values were chosen to match the experimental condition that $\frac{V_{POSS}}{V_{PS}} = 10$; all POSS and PS beads have a diameter $d = 1.0\sigma$. Polymer beads are linked with harmonic springs, as detailed in the model section. Immiscibility between POSS and PS domains is captures via an attractive SLJ potential between like domains.

We integrate using Brownian (Langevin) dynamics, as with the TNPTs study[16]. Systems are simulated at volume fractions ranging from $\phi = 40\% - 60\%$ in cubic boxes at $dt = 0.005$ and $T^* = 1.0$; each is first thermalized for $5e5$ time steps, compressed over $5e5$ time steps to the desired volume fraction, thermalized again, then finally run for 200 million time steps. Each state point is run for tether lengths $L = 4, 6, 7, 8,$ and 10.

An intermediate step of the assembly process from MD simulations is shown in Fig. 3.7a). A single DPOSS-4PSn molecule is inset in Fig. 3.7, showing the POSS cage in yellow, PS beads in white, and bonds in red. The gray (dark) domains represent the isosurface of POSS clusters; as indicated by the figure, POSS domains aggregate into micellar domains, while polymer tails point out from these domains, forming a soft corona. Two representations of spherical micelles formed by POSS domains are shown in Fig. 3.7b) and c), while hexagonally packed long micelles are shown in d).

Simulations also show a tendency to form both the A15 and Sigma phases for intermediate tether lengths, as shown in Fig. 3.8 and Fig. 3.9 phases, respectively. The A15 phase occurs at $L = 6, 7,$ and 8 for volume fractions of $\approx 43\% - 45\%$. Sigma phases occur at $L = 7, 8,$ and 10 for volume fractions between $\approx 44\% - 46\%$.

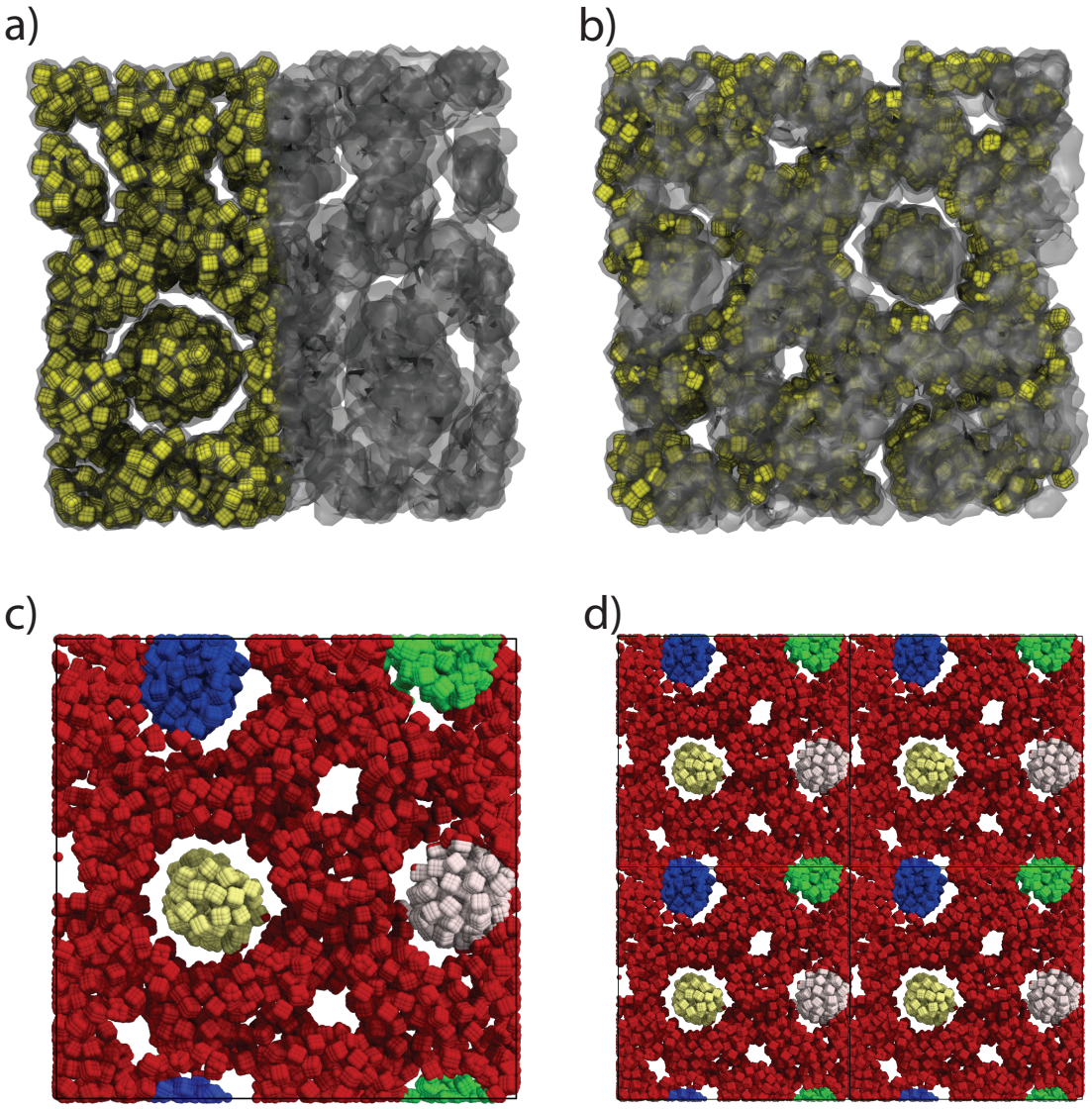

Figure 3.8: *A15 phase*. Frank-Kasper A15 phase images. All domains are individual micelles, and *do not* form continuous connected domains. (a-b) Different views of slightly defective A15 phase, showing the cubic symmetry. (c) Similar view where domains are colored for visual clarity. (d) View from (c) tiled once in each direction.

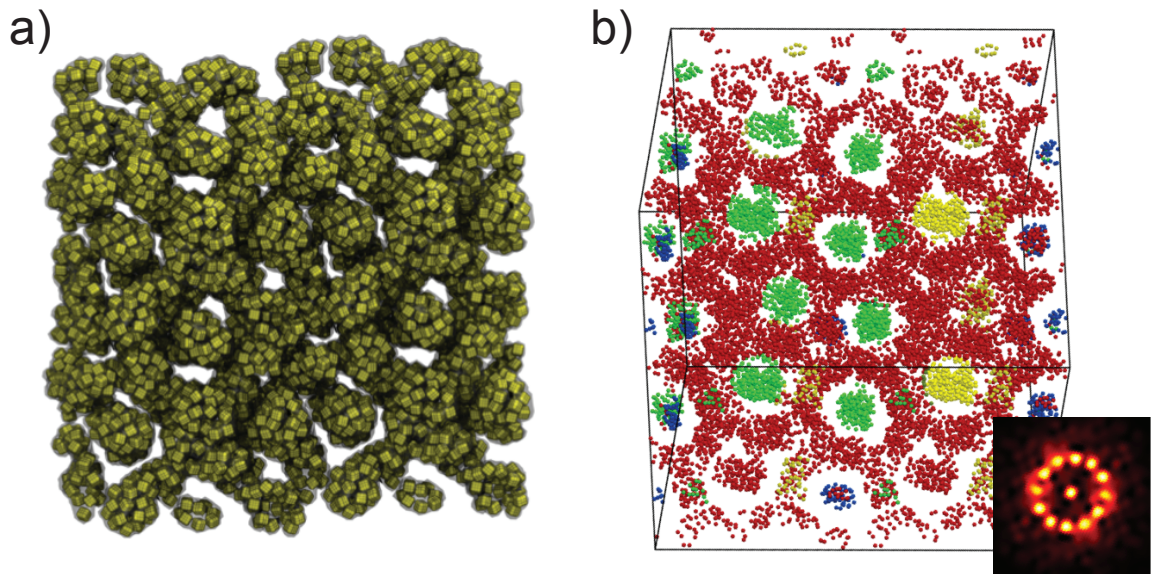

Figure 3.9: *Sigma and quasicrystal approximant.* Formation of the sigma QC approximant. 12-fold diffraction pattern as inset in (b).

3.3 Concluding remarks on TNPTs and DPOSS-4PSn

In our first study on TNPTs, we explored the phase behavior of a system of immiscible NP spheres tethered to one another, altering both the diameter ratio of the NPs and the length of the tether. Each configuration was simulated over a range of volume fractions and temperatures. We found long micelle, network, micelle in network, lamellae, and perforated lamellar phases. All phases reported as equilibrium phases in the triblock copolymer literature also appear in this TNPT system. In addition, we report three phases that are new to the design space: $\beta - Sn$ micelless in network, $R\bar{3}m$ micelles, and honeycomb with short and long micelles.

Varying both the diameter ratio and tether length have a significant impact on the self-assembled phases. First, as the diameter ratio deviates from 1.0, the asymmetry in the NP end group volume fractions stabilizes asymmetric phases. Second, increasing the tether length increases the number and complexity of the phases present. A longer tether provides the TNPT system more freedom to satisfy energetic constraints such as the bonding of incompatible NP end groups and the asymmetric NP sizes. The most complex phases, ($\beta - Sn$ micelle in network, Double Gyroid, Fddd, $R\bar{3}m$ phases), are found when the diameter ratio is asymmetric and the tether is long. We have introduced a new set of complex structures that can be spontaneously self-assembled from tethered nanoparticles and thereby comprise materials other than polymer. Only simple nanospheres of different

sizes are required to create these complex phases. For future studies, we theorize that adding additional constraints to the system, such as changing the shape of the nanoparticles to disrupt the packing[65] in the end group domains, may lead to new complex phases possessing hierarchies of order.

In our second study, we explored the ability of multiply-tethered "giant surfactant" TNPs to assemble Frank-Kasper, quasicrystal, and QC approximate phases. We observed transitions between hexagonal tubes, the A15 FK phase, and the Sigma phase as we increased the length of the polymer tether. We additionally hypothesize the presence of QC phases, provided the system size is large enough to accommodate a larger range of tiles; current simulations demonstrate a propensity to from phases with 12-fold diffraction patters, without the clear periodic order present in the sigma phase, indicating the formation of quasicrystalline order. These phases were corroborated with experimental evidence from a DPOSS-4PSn nanoparticle, demonstrating the same trend in ordering based upon increasing the polystyrene tether length.

CHAPTER 4

Microdroplets Made from Star Polymer Building Blocks

Polymers are a versatile building block, capable of forming a plethora of mesophases. Immiscible segments within the polymer block separate into separate domains based on their like (-philicity) or dislike (-phobicity) for the solvent or other polymer blocks. Their versatility accounts for much of the soft-matter phase diversity we've observed thus far.[45] These phases range from complex network phases,[46, 26] to thin films,[123] and droplets[27, 124, 125, 126, 127, 128].

Droplets are a convenient microstructure for a variety of applications including delivery of chemical and biological molecules [129, 127, 130], fabrication of electronic displays [131, 132], preparation of photonic [133], plasmonic [32], and photosynthetic [36] assemblies and self-healing structural materials [134], as well as separation, sensing and catalysis [135]. The external and internal structures of the microsphere are critical to their function and performance. The Ma group has demonstrated that porous polymer micro droplets are can be used to facilitate tissue regeneration; a porous structure on the micrometer scale can increase cell-loading efficiency, improve nutrition transport, decrease the amount of degradation products, and facilitate vascularization and tissue formation [136]. On the nanometer scale, a nanofibrous structure mimics the structure of collagen and improves cell-matrix interactions[136].

In this case study, motivated by experiment[136] we study a system of star polymer micro-droplets. Immiscibility between unreacted portions of the star polymer and the solvent trigger a phase transition between solid, hollow, and porous drops. We demonstrate via a combination experiments and computer simulations how the molecular structure of SS-PLLA dictates its self-assembly on both the nano- and micro-meter scales. We demonstrate and describe a versatile method to create microspheres with simultaneously controlled nano- and micro-structures. This system is a tunable mesoscale platform whose complex structure emerges from a single, simple interaction.

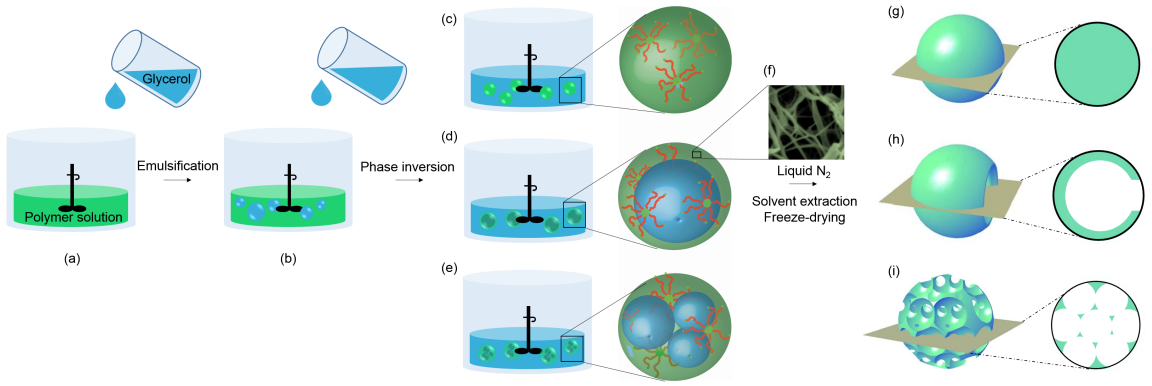

Figure 4.1: *Star-polymer double emulsion*. An illustration of a one-step emulsification combined with thermally-induced phase separation for the fabrication of nano- and micro-structured spheres. (a, b) Glycerol is slowly poured into a stirred polymer solution. (c-e) As the amount of the added glycerol increases, catastrophic phase inversion occurs, generating three types of emulsions: (c) single emulsions; (d) double emulsions with one inner droplet of glycerol inside one polymer droplet; and (e) double emulsions with multiple inner droplets of glycerol inside one polymer droplet (referred as "multiple emulsions" hereafter). (f) Emulsions are quenched in liquid nitrogen to induce phase separation on the nanometer scale. Upon solvent/glycerol extraction and freeze-drying, the single emulsions form non-hollow microspheres (g) the double emulsions form hollow microspheres; and (h) the multiple emulsions form nanofibrous spongy microspheres (i). Figure reproduced from publication.[18]

The results of this study are taken from our publication in *Advanced Materials*, "Simultaneous Nano- and Microscale Control of Nanofibrous Microspheres Self-Assembled from Star-Shaped Polymers", Zhanpeng Zhang, Ryan L. Marson, Zhishen Ge, Sharon C. Glotzer, and Peter X. Ma, doi:10.1002/adma.201501329.[18]

4.1 Star polymer double emulsion experiments

To study how the molecular architecture of star-shaped polymers affect assembly, we choose initiators with X initiating sites (hydroxyls (OH)) to polymerize L-lactide (LLA) to generate star-shaped poly(L-lactic acid) (SS-PLLA) with X arms (X = 2, 3, 4, 8, 16, 32 and 64. The average arm length is calculated from the feeding ratio, LLA:OH (=Y). The polymers are abbreviated as X-arm PLLA-Y (Table S1). Emulsification and thermally induced phase separation (TIPS) techniques are used to fabricate the microspheres from these SS-PLLAs (Fig. 4.1a). Specifically, glycerol is gradually added (Fig. 4.1(a, b)) into a 2% (w/v) SS-PLLA/tetrahydrofuran (THF) solution (glycerol : SS-PLLA/THF = 3:1 (v/v)),

which causes phase inversion and three types of emulsions to form (Fig. 4.1(c-e)). The emulsions are then quenched in liquid nitrogen to induce nanometre scale phase separation of the polymer solution (Fig. 4.1(f)). After glycerol and THF extraction with distilled ice water, the microspheres (Fig. 4.1(g-i)) are freeze-dried and stored in vacuum.

4.1.1 Nano-scale self-assembly

Quenching the emulsions in liquid nitrogen induces nano-scale phase separation of the polymer solution (Fig. 4.1(f)). During this thermodynamic process, polymer solutions can phase separate into bi-continuous nano-scale phases, presumably through a spinodal decomposition pathway, and ultimately form nanofibres upon solvent removal [136]. According to the Flory-Huggins (FH) theory, the FH polymer-solvent interaction parameter, χ, must exceed a critical value χ_c to trigger the spinodal decomposition pathway [137]. Increasing the molecular weight (MW) of a polymer can reduce χ_c to trigger the spinodal decomposition. In addition to the initiation of the spinodal phase separation, the stabilization of the phase-separated nanofibrous patterns is needed to obtain nanofibers. It is known that crystallinity of SS-PLLA increases as arm length increases [138]. Therefore, sufficiently long arm length is also needed to crystalize the nanofibers. Here, we find that SS-PLLAs assemble into nanofibers only when the arm length Y is above a critical value (denoted as Y_c) (Fig. 4.1a, b). $Y_c = 200$ when $X = 2, 3, 4$, while $Y_c = 100$ when $X \geq 8$. It should be noted that the actual arm number is few than X and the actual arm length (denoted as Y_a) is longer than Y when $X \geq 8$ because not all hydroxyls participate in the polymerization due to steric hindrance [139]. The actual critical arm length $Y_{ac} \approx 150$ when $Y = 100$ at $X = 8, 16, 32, and Y_{ac} \approx 200$ when $Y = 100$ at $X = 64$. Therefore, an approximate universal Y_{ac} (including linear PLLA (with 2 arms) and all the examined SS-PLLAs) appears in the range of 150-200. When the actual arm length Y_a is longer than this Y_{ac} range, any SS-PLLA forms nanofibers. Decreasing the actual arm length Ya below this range leads to fibre aggregation (Fig. 4.1b (middle) and Fig. 4.1c (middle)), and ultimately a smooth (dense) microsphere formation (Fig. 4.1b (left) and Fig. 4.1c (left)).

4.1.2 Micro-scale self-assembly

Prior to nanometre scale phase separation, SS-PLLAs phase separate on the micro-scale during emulsification. Three types of microstructures are identified: non-hollow microspheres (Fig. 4.1 (g)), hollow microspheres with one or multiple pore openings on the shell (Fig. 4.1 (h)), and spongy microspheres with an interconnected pore structure (Fig. 4.1 (i)). This suggests that single emulsions, double emulsions and multiple emulsions

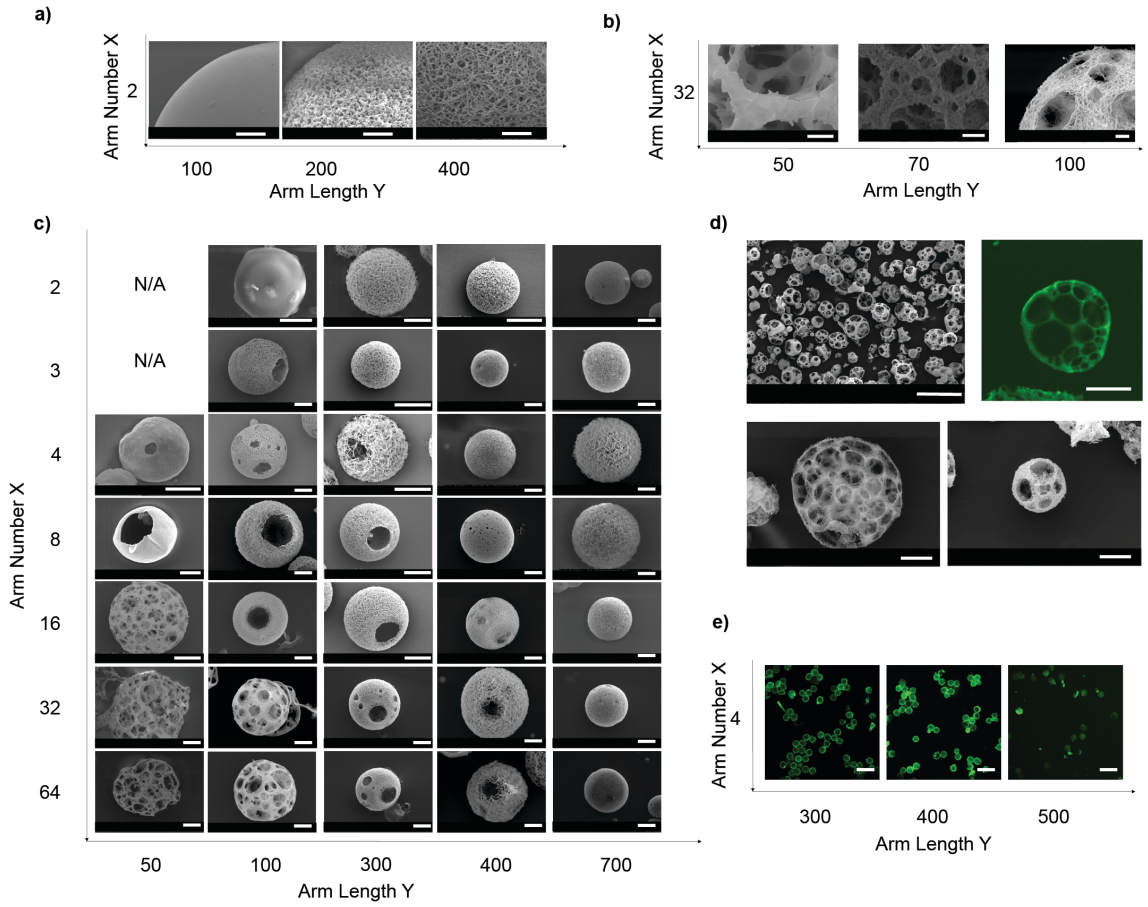

Figure 4.2: *Star-polymer experimental phase diagram.* Structural characterization of microspheres fabricated from SS-PLLA of different X and Y. (a-c) SEM micrographs of microspheres fabricated from (a) 2-arm PLLAs with $Y = 100, 200$ and 400. Scale bars: 5 μm; (b) 32-arm PLLAs with $Y = 50$ and 100. Scale bars: 5 μm; (c) SS-PLLAs of different X and Y, showing the structural transition process as X and Y changes. Scale bars: 20 μm. (d) SEM and cross-sectional confocal images of microspheres formed from 32-arm PLLA-100. Scale bars: 100 μm in left top and 20 μm in the rest figures; (e) Cross-sectional confocal images of microspheres fabricated from 4-arm PLLAs with $Y = 300, 400$ and 500. Scale bars: 100 μm. Figure reproduced from publication.[18]

are formed, respectively (Fig. 4.1 (c-e)). Combined with the two types of observed nanoscale structure (smooth and nanofibrous), six distinct types of microspheres are formed: smooth non-hollow microspheres, nanofibrous non-hollow microspheres, smooth hollow microspheres, nanofibrous hollow microspheres, smooth spongy microspheres and nanofibrous spongy microspheres (Fig. 4.1 (d)). Of particular note is the nanofibrous spongy microsphere, which integrates a nanofibrous structure with an internally interconnected multi-pore structure into microspheres with an increasing number of pores as the diameter increases (Fig. 4.1(e)).

The values of both X and Y affect the microstructure of the spheres. On the one hand, a small Y favours a more porous microstructure. For example, 16-arm PLLAs transition from non-hollow microspheres to hollow microspheres to spongy microspheres when Y decreases from 700 to 50. Four-arm PLLAs transition from hollow to non-hollow microspheres when Y increases from 300 to 500 (Fig. 4.1f). On the other hand, when Y is fixed, an increased X produces a more porous structure. For instance, when Y= 100, microspheres transition from non-hollow to hollow to spongy as X increases from 2 to 64. We speculate that the hydroxyls of the SS-PLLAs are responsible for the hollow/spongy structure formation, because the change of the molecular architecture affects the hydroxyl density of the polymers. Here, the hydroxyl density of SS-PLLA, denoted as OH/LLA, is calculated from the molar ratio of hydroxyls to monomer LLA. Thus, OH/LLA=1/Y. We therefore hypothesize that: 1) the hydroxyl groups are required for the hollow/spongy structure formation, and 2) a high OH/LLA value favours the formation of a hollow/spongy structure. Two experiments are designed to test these hypotheses. In the first experiment, we cap the hydroxyls of SS-PLLA prior to emulsification and TIPS (Figure S2a). The hydroxyl-capping reaction "turns off" the polymer's ability to self-assemble into hollow microspheres. For example, 4-arm PLLA100, which is capable of forming hollow microspheres (Fig. 4.1d), assembles into non-hollow microspheres after the hydroxyl capping reaction (Fig. 4.2a). This finding supports our first hypothesis that the hydroxyl groups on SS-PLLA are required for the hollow structure formation. In the second experiment, we double OH/LLA without altering X or Y. 4-arm PLLA-400, which has a low OH/LLA value (1/400) and forms non-hollow microspheres (Fig. 4.1d), assembles into hollow microspheres after its OH/LLA is increased to 1/200 (Fig. 4.2b). 16-arm PLLA-100 (OH/LLA=1/100), which forms hollow microspheres (Fig. 4.1d) before modification, assembles into spongy microspheres after hydroxyl doubling (OH/LLA increased to 1/50) (Fig. 4.2c). These findings support our second hypothesis that a higher OH/LLA favours hollow/spongy structure formation. In these two experiments, the modification does not alter the nanometre scale phase separation, which agrees with our previous discussion that the nanometre scale phase sepa-

ration is mainly a result of polymer chain-solvent interaction (arm length). Associating the hollow/spongy structure formation with the OH/LLA of the SS-PLLAs, we determine the OH/LLA threshold values for structural transition of the spheres on the micro-scale. Figure 4.2c shows a phase diagram based on these values and the Y_c values.

4.2 Star polymer droplet simulations

We further hypothesize that the hydroxyl groups of SS-PLLA stabilize the polymer solution/glycerol interface due to the high affinity of hydroxyl to glycerol. As a result, SS-PLLA with a higher OH/LLA favours the formation of double/multiple emulsions, which contain larger interfacial area than single emulsions. To test this hypothesis, which requires information more directly obtainable via computer simulation, we perform dissipative particle dynamics (DPD) simulations for 4, 8, and 16 arm polymers and for a range of arm lengths using HOOMD.[24, 23]

The coefficients for F_c between polymer beads (A_{PP}) and between glycerol (solvent) beads (A_{SS}) were set at $A_{PP} = A_{SS} = 20.0$ as a baseline, as has been done in prior works. To increase affinity for the hydroxyl and solvent (glycerol), this repulsion was reduced to $A_{HS} = 10.0$, thereby making the hydroxyls attractive to the solvent. The repulsion between hydroxyls was also reduced to $A_{HH} = 10.0$, so that the hydroxyls have the same tendency to aggregate with other hydroxyls or at the glycerol-polymer solution interface. Because the hydroxyl-polymer and polymer-solvent interaction is repulsive, we increased the repulsion to $A_{HP} = A_{PS} = 40.0$.

Star polymers are created by linking beads together with harmonic springs $V(r) = \frac{1}{2}k(r - r_0)^2$, with $k = 4$ and $r_0 = 0$. Arms are attached to a single polymer core bead.

The temperature in the simulations was set at a standard value of T = 1.0. The timestep was chosen to be dt = 0.01 as a compromise between integration stability and expediency of the simulation. All simulations were run for 5 million DPD timesteps. Systems were initialized by randomly placing one million solvent beads in a box at a volume fraction of 80%. Star polymers were generated randomly beforehand, and then placed individually in a spherical shell, allowing for overlaps between polymer and solvent beads. The box size remained fixed across all simulations. Systems were thermalized for 30 thousand timesteps, and then run for 5 million steps to equilibrate.

The amount of solvent was kept fixed at 1 million particles, while the concentration of polymer was varied. Simulations were performed for eight different polymer concentrations $\phi = \frac{N_{poly}}{N_{total}} = 30\%, 28\%, 25\%, 22\%, 19\%, 16\%, 13\%, or 10\%$. System sizes varied between 1.1 and 1.5 million particles, depending upon concentration; individual large sys-

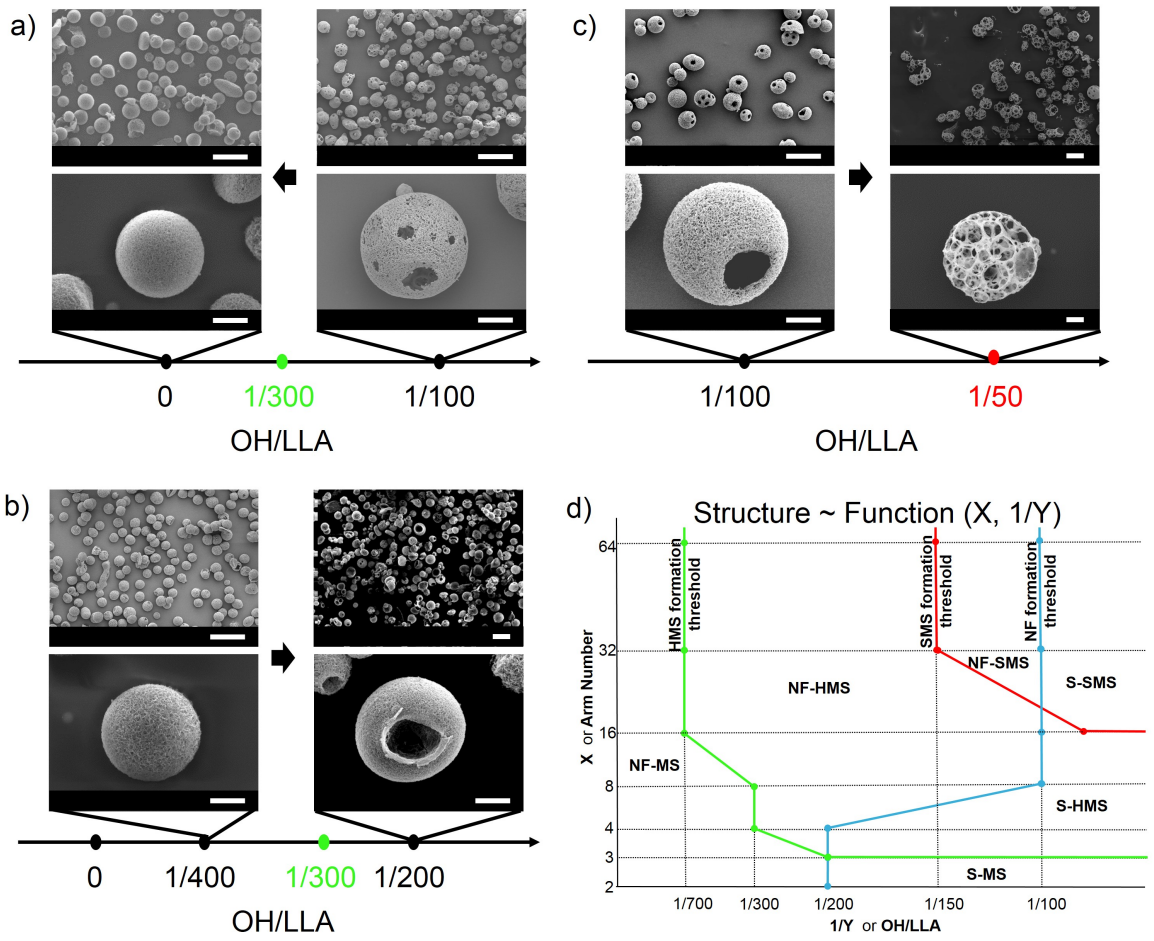

Figure 4.3: *Star-polymer experimental phase diagram plot*. Hydroxyl density of SS-PLLA affects the micro-scale structure of microspheres. (a-c) SEM micrographs of microspheres fabricated from (a) 4-arm PLLA-100 before (right column) and after (left column) hydroxyl capping. (b) 4-arm PLLA-200 before (left column) and after (right column) hydroxyl doubling. (c) 16-arm PLLA-100 before (left column) and after (right column) hydroxyl doubling. The hollow-to-non-hollow transition point is 1/300 for 4-arm PLLAs. The hollow-to-spongy transition point for 16-arm PLLAs is 1/50. Scale bars: 100 μm on the top row, 20 μm on the bottom row. (d) The structure of microspheres as a function of arm number and arm length. Note: This graph is based on SS-PLLA without modification. Figure reproduced from publication.[18]

tems run contained ≈ 11 million particles. At each concentration, four different arm lengths were run: $L = 10, 40, 80,$ or 120 beads per arm. Finally, all simulations were performed for 4, 8, and 16 arms. In total, over 100 individual simulations were performed. A total of 20,000 GPU/CPU hours was employed for this study. To ensure reproducibility of the structures, three independent runs were conducted for 50 million time steps each using Blue Waters.

For each set of arms, simulations are run for arm lengths of L = 10, 40, 80, and 120 coarse grained beads, linked together with harmonic springs. To capture the catastrophic phase inversion process that causes the initial encapsulation of glycerol into the polymer solution droplets, star polymers are initialized within a thin spherical shell. Each simulation containing between 1.1 and 1.5 million particles is run for at least 5 million time steps to ensure proper equilibration, and is additionally verified by running to 50 million time steps for one of each type of microspheres (non-hollow, hollow, and spongy). Larger simulations (containing 11 million particles, Figure 4.6) of each type of microspheres are also run to rule out finite size or other non-physical effects. In total, over 100 independent state points are simulated.

For all simulated state points, a transition from hollow to non-hollow is observed as L increases, supporting the experimental data. For star-shaped polymers with long arms, the polymer shell ruptures during the simulation and the glycerol mostly leaves the droplet, with only small pockets of solvent remaining inside (Figure 4.4a, b). For star-shaped polymers with short arms, the double emulsion is stabilized, with the hydroxyl groups concentrated at both the glycerol/polymer-solution and the polymer-solution/glycerol interfaces (Figures 4.4c, d & 4.6a, b). By looking at a single star-shaped polymer molecule (Figure 4.4c), we find that the polymer "stretches" its arms to reach to the interfaces, acting like a surfactant capable of stabilizing both the glycerol/polymer-solution and the polymer-solution/glycerol interfaces.

To verify the effect of the hydroxyl stabilizer, two non-hollow cases were tested separately: 8 arm, $L = 120$ at polymer concentrations of both 10% and 13%. The strength of the hydroxyl-solvent and hydroxyl-hydroxyl repulsion was decreased, thereby increasing the preference for the hydroxyls to aggregate at the polymer/solvent interface. In all cases, $A_{HS}, A_{HP} = 8.0, 5.0, 2.0,$ or 1.0 reducing A triggered a hollow to non-hollow transition. Increasing the strength of attraction between the hydroxyls and glycerol (mimicking the "hydroxyl doubling" modification experiment) causes a transition from non-hollow to hollow structures, again matching the experimental data (Figure 4.4b). These results support our hypothesis that hydroxyls can stabilize the glycerol/polymer-solution and the polymer-solution/glycerol interfaces for hollow sphere formation. In addition, for 16-arm polymers

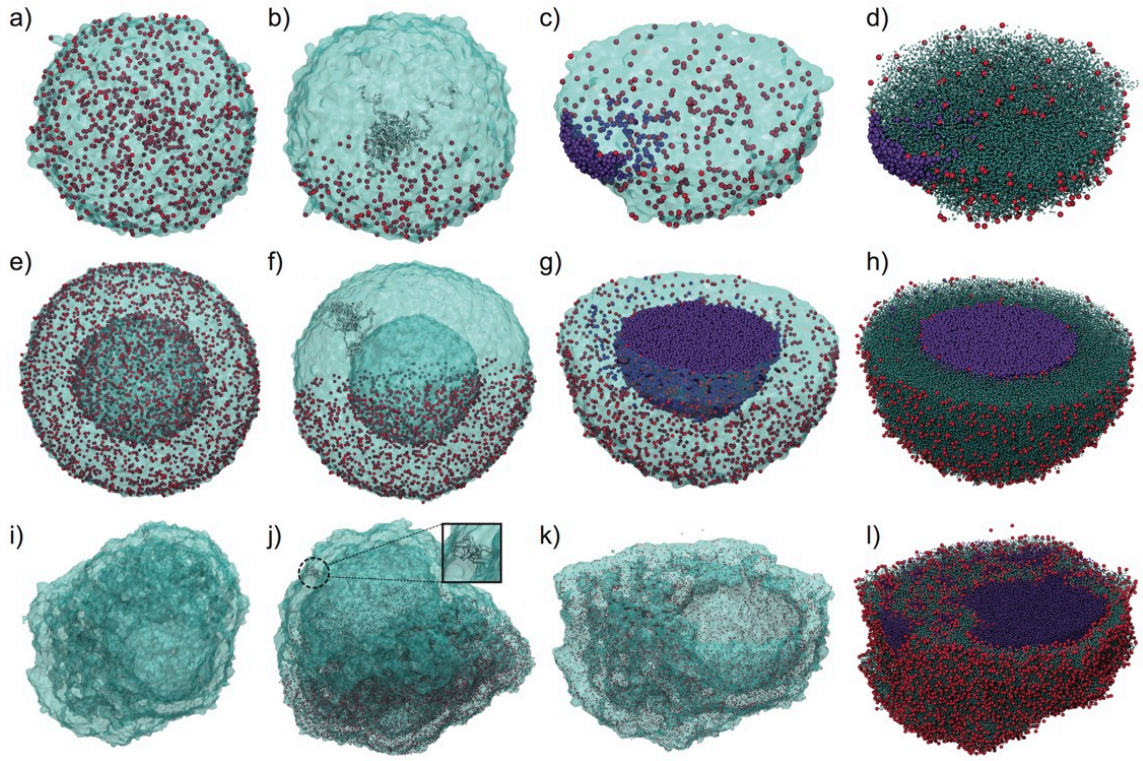

Figure 4.4: *Star-polymer droplet phases from simulations*. Images of all 3 morphologies of droplets - hollow, non-hollow, and porous - shown in various representations to make features apparent. (a-d) Non-hollow droplets; (e-h) nollow droplets; (i-l) porous droplets. In the right two columns only half of each droplet is shown so that the inner structure is visible.

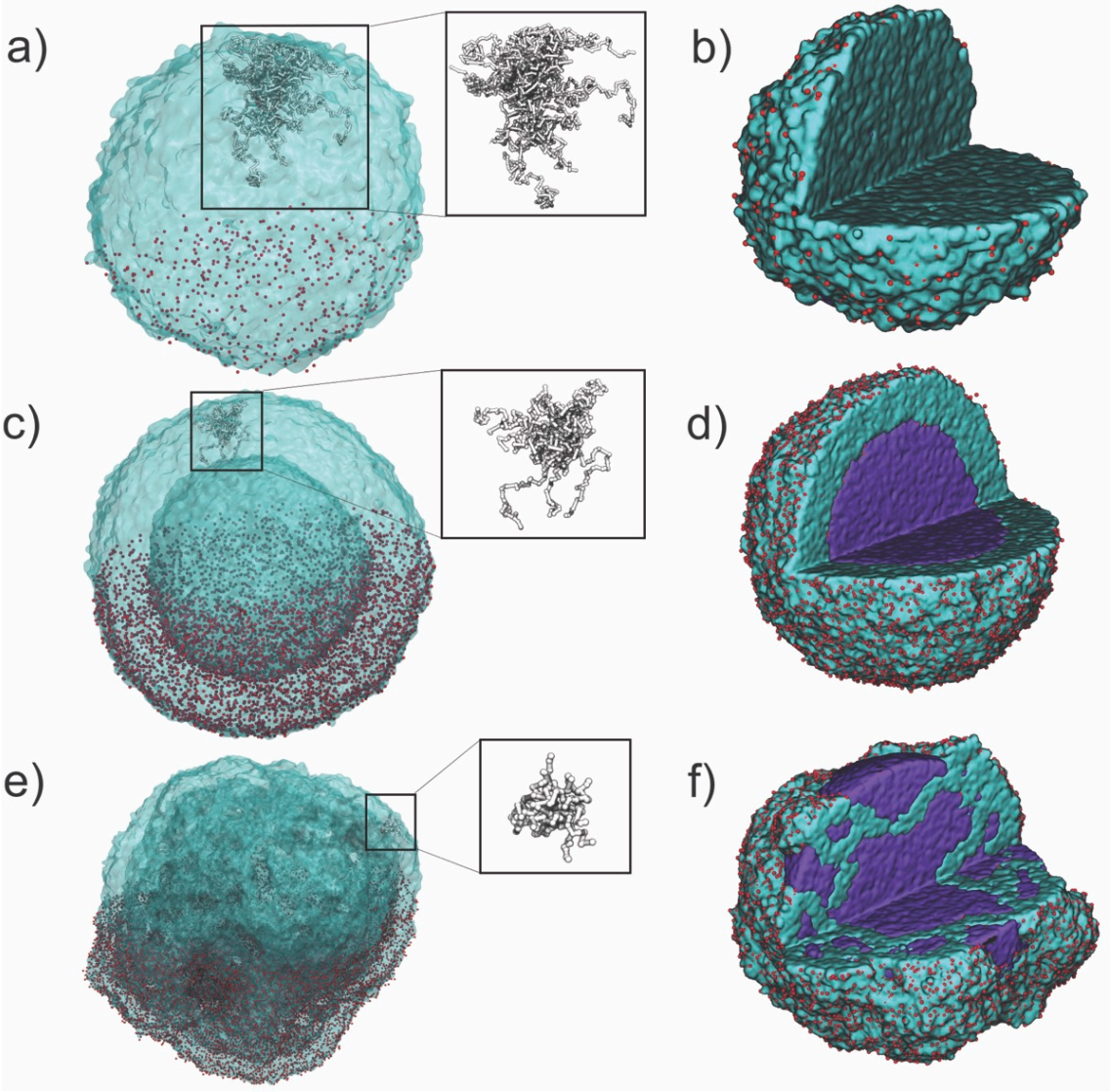

Figure 4.5: *Star-polymer simulation phases from varying arm length*. DPD simulations of various star-shaped polymers and the formation of different emulsions. For 16-arm PLLAs, as the length of the polymer arm decreases from, the structures undergo a transition from non-hollow ($L = 120$, a, b) to hollow ($L = 40$, c, d) to spongy ($L = 10$, e, f). This happens in a variety of polymer droplet concentrations and in other star polymer systems with different arm numbers. The left column of images (a, c, e) shows the polymer iso-surface, with individual hydroxyl beads on the bottom half of the droplet shown in red. The conformation of a single 16-arm PLLA is shown in the square box. The right column (b, f, j) shows the internal structure of the same droplet in the left, with glycerol stained in purple. Some hydroxyls (red beads) are removed for clarity. Figure reproduced from publication.[18]

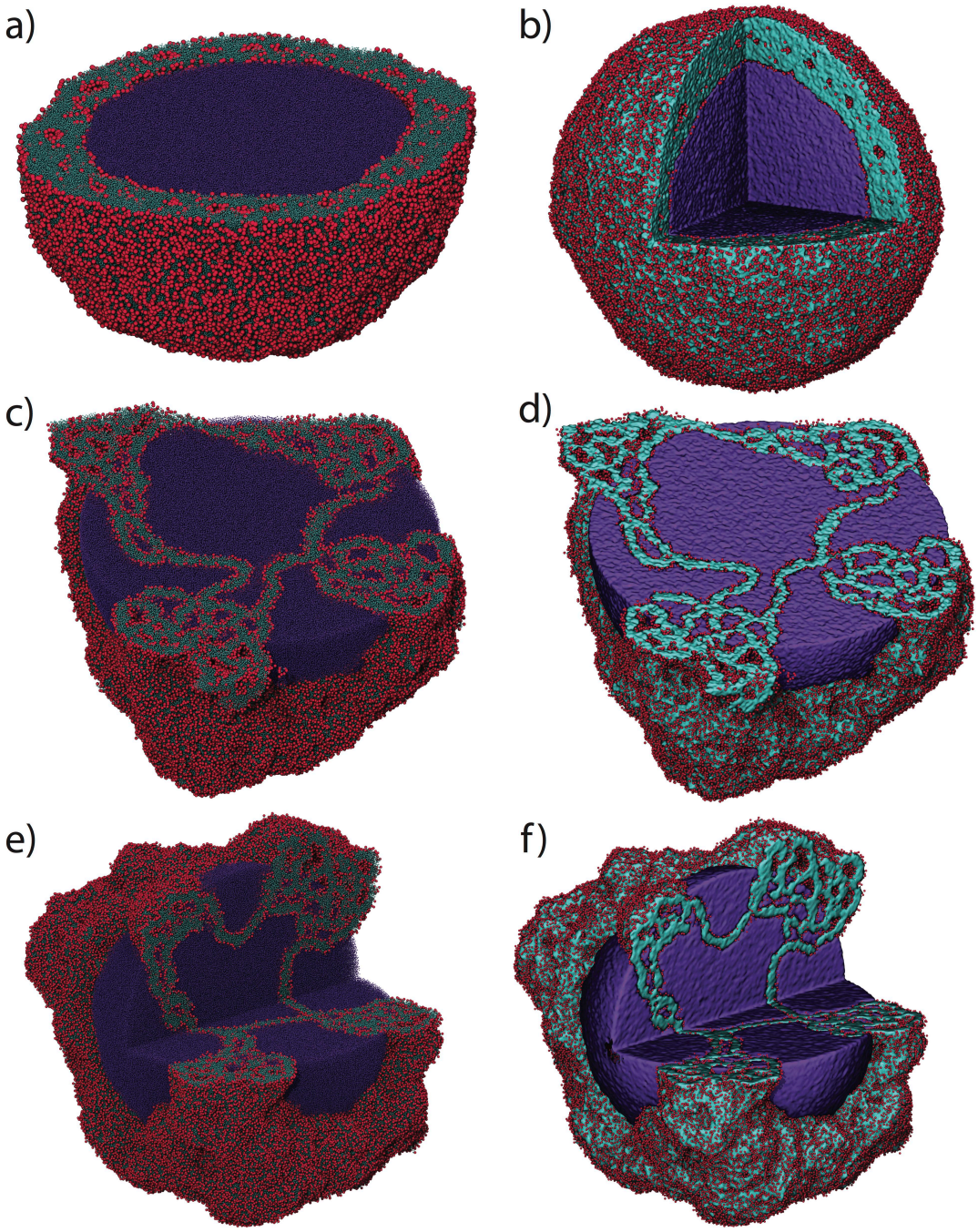

Figure 4.6: *Star-polymer simulation phases from varying arm length.* Large scale DPD simulations of 16-arm star-shaped polymers of varying arm length (containing 11 million particles) and the formation of different emulsions: (a,b) the formation of hollow structure at $L = 40$; (c-f) the formation of spongy structure at $L = 10$. Left column shows individual bead representations, while the right shows the isosurface.

with $L = 10$, glycerol molecules in the interior of the polymer solution droplet separate into multiple domains (Figures 4.4e, f & 4.6c-f), consistent with the experimental finding that 16-arm PLLA with short arms form spongy microspheres (Figure 4.1d). These simulation results indicate that, while the catastrophic phase inversion might initially cause the encapsulation of glycerol inside the polymer solution droplet (Figure 4.1), the final structure of the emulsions is determined by OH/LLA and the molecular structure of SS-PLLAs.

4.3 Concluding remarks on star polymer micro droplets

In summary, star-shaped polymers with varying arm numbers and arm lengths are synthesized, characterized, and simulated for the systematic study of their self-assembly during emulsification and TIPS processes. During these processes, phase separation on the nanometer and micrometer scales determines the final structure of the microspheres at these two levels. The nano-scale phase separation of SS-PLLA depends on arm-length, while the micro-scale structure is determined by arm-number and OH/LLA ratio. These mechanisms provide guidance on simultaneous control of nano- and micro-structure formation and resulting in several novel microspheres, which may broadly impact biomedical and other emerging technologies. For example, the interconnected internal pore structure of spongy microspheres enables deliberate control of cell-cell interactions to maximize regeneration outcome (to be reported in future publications). The nano- and micro-structured spheres may also provide advanced 3D substrates for catalysis or bio-sensing technologies.

CHAPTER 5

Chiral Rods from CdTe Truncated Tetrahedral Building Blocks

We now turn our attention to how interactions down to the individual nanoparticle can dictate structure at the mesoscale. We have shown that immiscibility between parts of the building block and the solvent can lead to ordered assemblies. More complex interactions can also occur, leading to anisotropic effects between pairs of particles, or portions of the blocks themselves. Examples of these anisotropic interactions include the shape of the nanoparticles itself[65], induced dipoles due to surface charges[43], and surface interactions due to stabilizers or coatings[44]. These anisotropic interactions can create free stranding structures such as wires[30, 37], sheets[34], or clusters[36], which can then be used for a variety of applications.

Chiral structures are of particular interest due to their ability to filter circularly polarized light of a preferred handiness[140, 141, 44, 142, 143, 144], and for their usefulness as candidate photonic structures[145, 146, 147]. In this case study, we demonstrate that CdTe NPs stabilized by (D, L) -cysteine (CYS) can self-assemble into chiral helical structures without a template. The left and right-handed helices are controlled by the chirality of CYS as evidenced by the circular dichroism spectroscopy. Finally, we simulate the effects of the D-CYS and L-CYS stabilizers using a simple chiral potential model, and demonstrate that localized effects of the chiral stabilizer can selectively produce the desired chirality in the micro/macroscopic helices. These tunable chiral structures provide a route to understand and design chiral optical structures. The text that follows is taken from our forthcoming publication "Enantioselectivity of Biomimetic Rod-Like Supraparticles Self-Assembled from Chiral Nanoparticles", work done in collaboration with the Kotov group, which is currently in preparation.[19]

Chirality is a ubiquitous property in nature that can be found in wide range of building blocks of matter, and, among other manifestations, govern numerous physiological mechanisms. Chirality can appear at the atomic scale in amino acids as well as at the nanometer

scale in peptides, proteins, DNA and metal-amino acid supramolecules[148, 67, 149]. The transition from one scale to another occurs via assembly of many smaller units into superstructures with hierarchical chirality. Examples include assemblies known from biology, synthetic polymers, and liquid crystals exhibiting chiral hierarchy[68, 150, 148]. Besides fascinating mathematical relationships between the symmetries of structural units and assemblies, further studies of hierarchically chiral nanostructures are motivated by chemical, optical, mechanical, and biological phenomena associated with them[144, 151]. As such, the interplay of plasmonic/excitonic phenomena observed for inorganic nanostructures with chiral geometries appears to be one of the most dynamic areas of nanoscale science today that can benefit from replicating the methods of chiral assemblies known from biological matter for semiconductor and metal particles[44, 136].

Water-soluble NPs demonstrate a similar ability to self-assemble originate from the same chemical and intermolecular interactions[152]. They are known to self-assemble into nanowires, nanosheets, and even geometrically complex structures exemplified by helices[152, 66]. It is conceivable that inorganic NPs carrying chiral molecular units can form secondary structures with chirality at a larger scale; for instance, at the scale of tens or hundreds of nanometers. This effect is demonstrated in the enantioselective assembly of CdTe NPs observed recently driven by either packing of chiral nanoscale core or by intermolecular interactions of chiral stabilizers on their surface[66, 37]. Besides further validation of the mechanisms of the assembly of inorganic NPs and creating their adequate theoretical models, the next step in this research would be increase in complexity of the chiral assemblies. Replication of some elements of organization of, for instance, viruses could be realistic although challenging.

The relatively small difference in energy of interactions associated with molecular chirality can be enhanced by the collective effects in large assemblies and multiplied for large number of molecules with chiral centers. Therefore, we decided to investigate self-assembly phenomena in CdTe NPs stabilized by cysteine (CYS). Besides its L- form, which represents one of the most common amino acids, we stabilized NPs with it D- form and allowed them to self-assemble under conditions that are conducive to formation of supraparticles[32]. These assemblies typically involve several hundred individual NPs and several (million) stabilizer molecules, which creates a sufficiently large chemical system where the interplay of the weak interaction forces between particles, with the effects of the chirality of the CYS stabilizer, can leads to enantioselectivity at much larger scales.

5.1 Cysteine coated CdTe nanoparticle experiments

D and L -CYS stabilized CdTe NPs (D -NPs and L-NPs) were synthesized by a arrested precipitation method following a standard protocol (Supplementary Information, Part I)[44, 153]. To observe self-organization phenomena, the CdTe NPs were precipitated by addition of isopropanol and centrifuged for 5 min, followed by redispersion in deionized water in pH 9.0 ultrapure water and stored in a nitrogen atmosphere (Supplementary Information, Part I). The solution of NPs changed its color from orange to dark-red when left it in dark at room temperature for 8 hours, indicating that self-assembly of NPs has occurred.

Scanning electron microscopy (SEM) showed the formation of NRs (NRs) as the primary product of the self-assembly process. The length of the NRs was $\approx$ 250 nm for assembly of D -NPs and $\approx$ 300 nm for L-NPs (Fig. 5.1 a, d). The length of NRs can be controlled by the NPs preparation conditions, which can be as long as 5 m. Moreover, the NRs showed the tendency to self-organize even into higher order parallel structure. Scanning transmission electron microscopy (STEM) showed that NRs have pronounced twist (Fig. 5.1b, e) although not as regular as in DNA or some viruses[154]. The diameter of NR was $\approx$ 20 nm for D -NP assemblies and $\approx$ 23 nm for L-NP assemblies; Interestingly, the NRs show different preferable twist direction when they are assembled from D-NPs and L-NPs. The assemblies from D and L-NPs were left-handed helices and right-handed helices, respectively. To obtain three-dimensional image of the NRs, we collected STEM images from -70° to 70° and tomographically reconstructed their geometry (Supplementary information). NRs self-assembled from D-NPs show left-hand helical structures. In contrast, right-hand helical structures existed in the samples of self-assembly of L-NPs (Fig. 5.1g-j). Along with the assemblies with helical motif we also observed structures with discrete NPs attached to the central Te rod and indiscernible regularity of the surface topography when assemblies formed in suboptimal conditions. We evaluated the preference of helical direction of one hundred samples from STEM and found consistent chirality. STEM images show the helical NRs have an average pitch of $\approx$ 10 nm. Further characterization of the helix pitches in solution was conducted by small angle X-ray scattering (SAXS). According to the equation given by $d = \frac{2\pi}{q}$, the d-spacing is 12.5 nm, which is consistent with STEM results.

Nano-area X-ray energy dispersive spectroscopy (XEDX) (Fig. 5.2a) showed $\approx 2:1$ atom ratio for Te to Cd in the central part of the chiral helical structure; however, the Te to Cd ratio converges to 1:1 for the outside layer. High resolution TEM (HRTEM) images (Fig. 5.2 b, c) clearly indicate the CdTe NPs lies the outside of the chiral helical structure, the center part is a single crystal nanowire with $\approx$ 5 nm. The thickness of the twisted CdTe

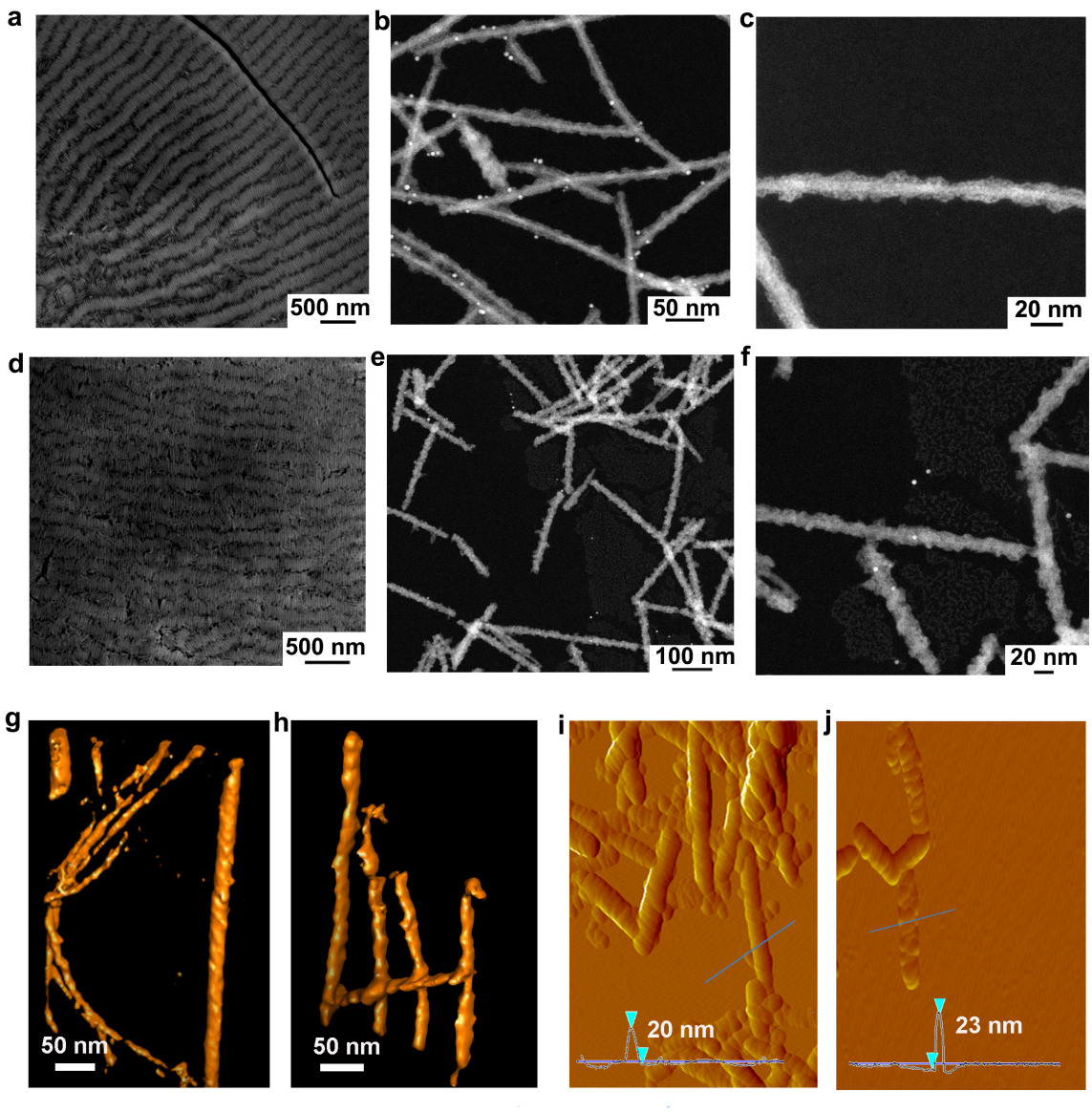

Figure 5.1: *Nanoscale geometry of left and right - hand NP assemblies*. (a), (b), (c) and (g), SEM, STEM and STEM tomography images of assembled D -NPs. (d), (e), (f) and (h), SEM, STEM and STEM tomography images of assembled L -NPs. (i) and (h), AFM images of assemblies obtained from D-NPs and L-NPs. Note: In Figure 1(b), 1(e) and 1(f), the bright points are gold NPs added as spatial marker for TEM tomography. Figure reproduced from our forthcoming publication, in preparation.[19]

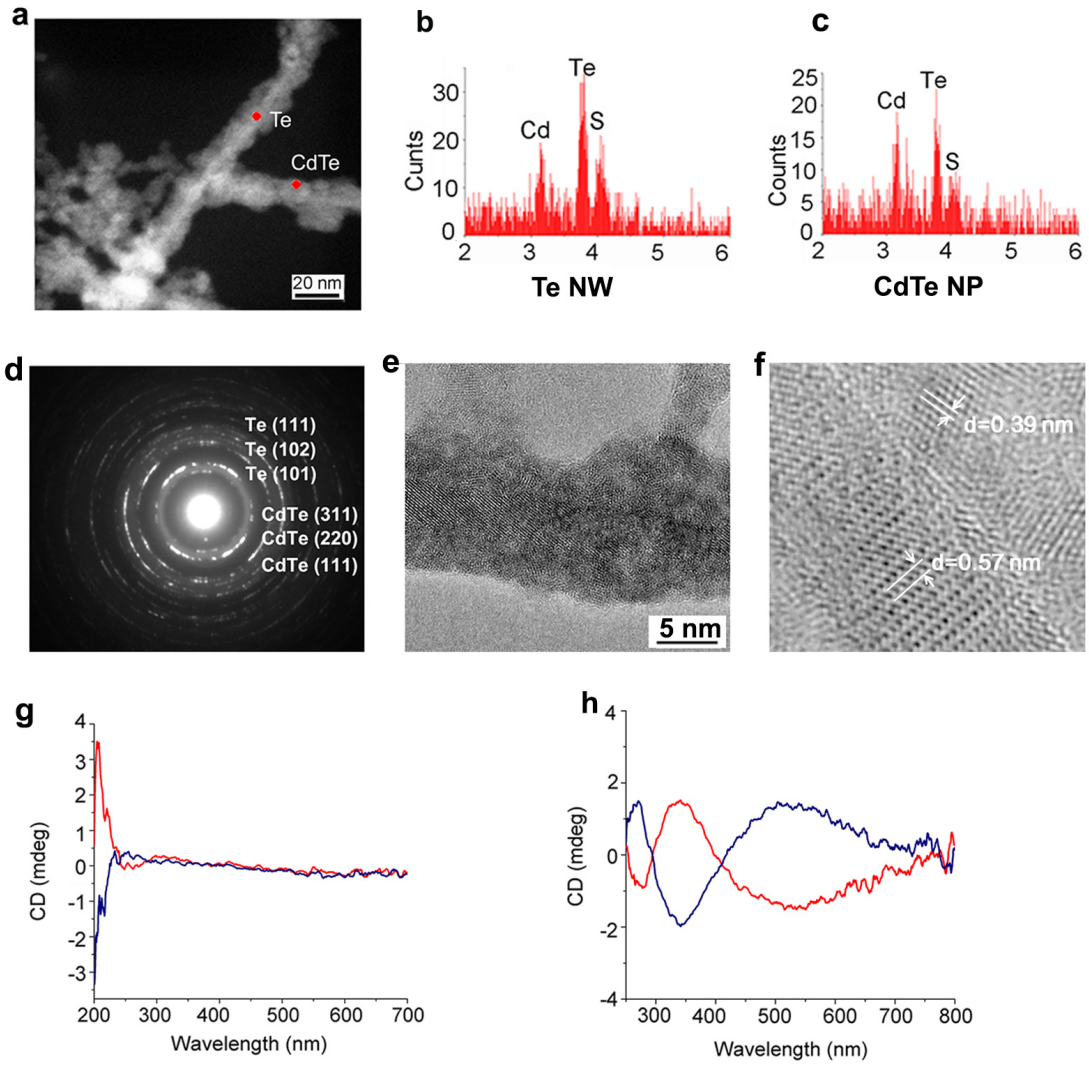

Figure 5.2: *Nanoscale structure and chirality of helical NP assemblies*. (a-c), Nanoscale EDX analysis of peripheral and core part of helix. (d), Electron diffraction of right -hand helix. (e, f), HRTEM image of peripheral CdTe NPs and Te core. CD spectra of D-cys (red) and L-cys (blue) NP chains obtained after 8 hours of the assembly. CD spectra of left (red) and right (blue) -hand random network structures (g) and helix (h) obtained after two weeks of the assembly. Figure reproduced from our forthcoming publication, in preparation.[19]

layer is about 10-15 nm. Electron diffraction for the helical structure gives a diffraction pattern for a cubic phase for CdTe and a hexagonal phase for Te. The diffraction pattern for CdTe corresponds to crystal faces of (111) (d=0.39 nm), (220) (d=0.22 nm) and (311) (d=0.19 nm). The crystal faces indicated in diffractions pattern (101) (d=0.32nm), (102) (d=0.23 nm), (111) (d=0.20 nm) characterize Te in a hexagonal phase and show the Te have a (001) growth direction. Most importantly, the chiral helical structures, as is typical of chiral structures, show non-zero circular dichroism in the visible region. However, the random network structures in the supernatant show zero CD signals in the visible region, although chiral signals from (D and L) CYS bound to the NPs can be seen between 200 nm - 300 nm[44]. Compared with the random network structures found in the supernatant (Fig. 5.2e), the twisted chiral structures show pronounced mirrored-peak signals in the viable region (Fig. 5.2f), which obviously results from the isotropic chiral helical structure of the samples. The CD spectra of assemblies critically depend on the quality of the helical structures. For example, NPs with a thin layer of particles randomly attached to the Te nanowire surface present broadened and odd, asymmetric, CD signals. Therefore, it is reasonable that the symmetric CD signals in visible region are from persistent regions of perfect order over long range within the nanowires.

To further understand the intrinsic structural evolution and the driving forces from NPs to chiral helices, we examined the samples at time points of 8, 24, 48 and 72 hours by measuring their morphology through TEM, photoluminescence (PL) peaks, CD spectroscopy, and the zeta potential (Fig. 5.3). In the first 8 hours, TEM images revealed a gradual structural transformation from NPs to short NPs chains for D-NPs (Fig. 5.3) and L-NPs assemblies. Interestingly, some short twisted chains can be seen in the assemblies of D-NPs. However, this does not show up in the corresponding CD spectroscopy of D-NPs assemblies, which suggests the system is mainly composed of dispersed NPs. However, the CD spectroscopy of L-NP assemblies does show an enhanced broad peak compared with NPs solution which suggests more NP chains have formed. By 24 hours, we observed D-NP assemblies showed some straight, short wires in the major NP chain phase, which is confirmed by the corresponding CD signal. However, neither morphology nor CD signal for L- NP assemblies could show obvious change at 24 hours which suggests the assembly dynamics differ for D-NPs and L-NPs. With increasing to 48 hours and 72 hours, both D-NP and L-NP assemblies show many short, helical wires, for which the corresponding CD signals show a distinct mirror symmetric bisignate Cotton effect[67, 155, 156, 157, 158, 159]. It is clear that the NP chains self-organize into left and right helical forms on the surface of the nanowires in the intermediate state for the formation of long chains. In the immediate transition, PL peaks only show slight blue shifting, which is not like obvious red shift due

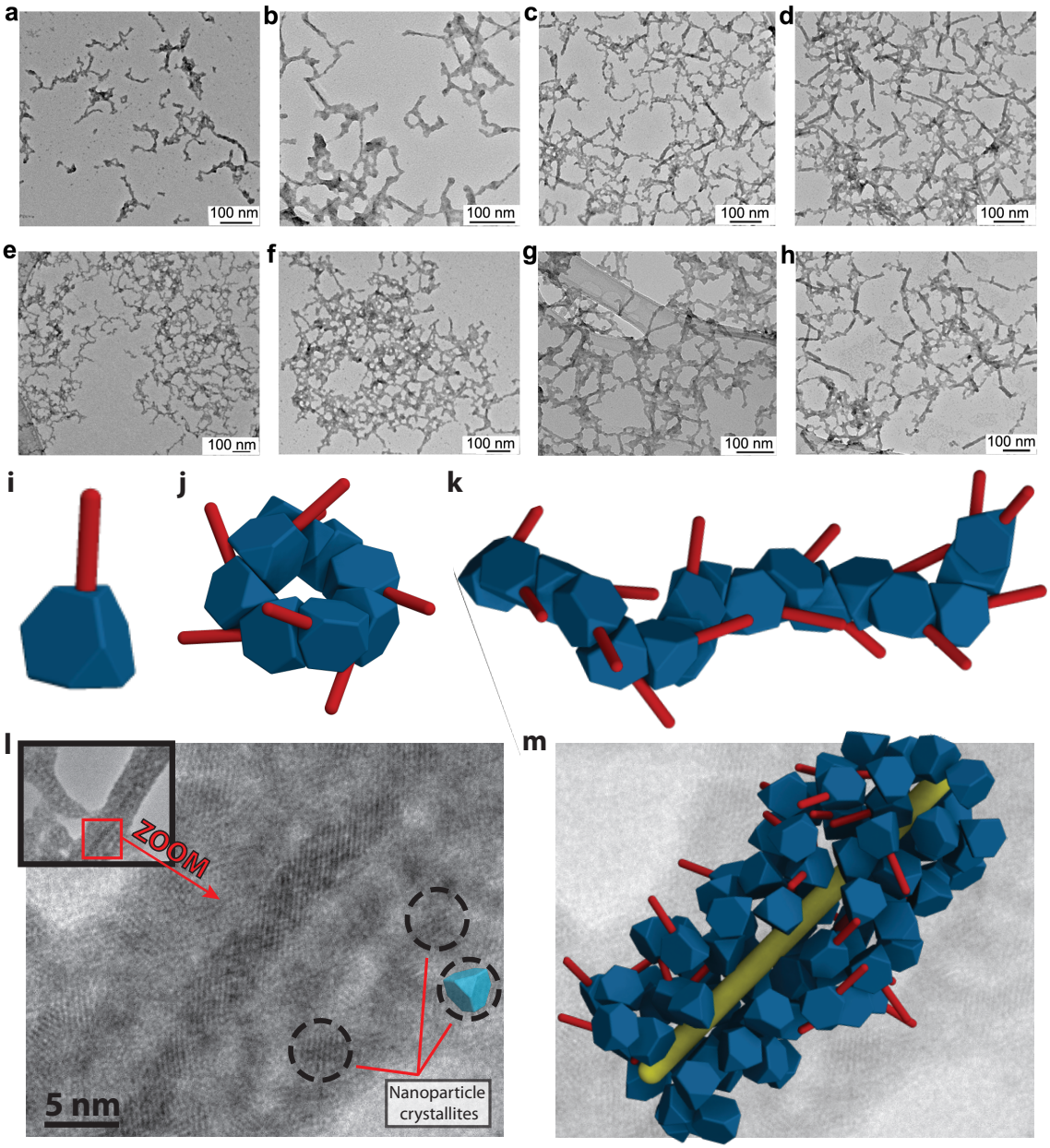

Figure 5.3: *Intermediate states of helix assembly of of D-NPs*. (a-d) TEM images of the formation process of left -hand helical structures by assembly of D -NPs in 8 hours (a), 24 hours (b), 48 hours (c) and 72 hours (d). (e-f) TEM image of a magnified composite NP/nanowire assembly obtained 72 hours. (Insert images are the simulated assembly of CdTe NP/nanowire assemblies from a single model CdTe NP with electric dipole direction) Figure reproduced from our forthcoming publication, in preparation.[19]

to aggregation of NPs4. It is well known that ordered aggregations of NPs red shift the PL peak and oxidation of NPs contribute a PL blue shift. Considering that most of the ultimate products are Te-CdTe core - shell helical structures, it is reasonable that the slight blue shift is due to aggregations of NPs partially counteracting the effect of oxidation of NPs, which release Te2- from the surface of NPs. Finally, the NP chains will attach on the surface and remain stable in a thermodynamic, free-energy minimizing state. The aggregation of NPs and the formation of helical structures make the CYS on the surface of NPs bind to each other and subsequently decrease the electrostatic force between NPs. This is confirmed via our observation of a decreasing zeta potential during the immediate process of assembly.

What balance of forces is behind the formation of helices? Previous reports indicated that the self-organization of organic helices arises mainly from the coordination of multiple types of short range and long range forces[160, 161]. Hydrogen bonding is one of the most important forces in the self-organization of chiral biotic tissues via bonding to small bio-units, e.g., the DNA double helical structure and chiral peptides - amphiphile nanofibers[155, 161, 162]. In contrast, helical inorganic nanobelts can be formed by oriented attachment or screw axis dislocation[155, 163]. As globular protein mimics, biomolecule-stabilized colloidal inorganic NPs are similar in size, shape and charge, which possibly assemble with structure transformations depending on amino acids interaction with hydrophobic forces, van der Waals forces, hydrogen bonds, etc.; although the inorganic "core" of NPs is an impenetrable crystal that will not present a dynamic assembly process, NPs with zinc blende atomic packing were theoretically proved to be a truncated tetrahedron structure, which contributes to a dipole moment[43, 29]. By adjusting the weak interaction forces between NPs including the weak interaction force from stabilizer and inorganic "core", NPs could also present some similarity with proteins in the assembly behavior. Therefore, we hypothesize that the formation of chiral helical structures is due to the self-building of chiral CYS-capped inorganic NPs. The driving forces include van der Waals forces, dipole - dipole, dipole-charge interaction, and hydrogen bonds between NPs. The helical directions of assemblies are controlled by the D-CYS and L-CYS.

As indicated in the study of the intermediate state, the various transformations in the transient state observed are different from previous assembly reports in organic and inorganic helical systems[155, 162, 140]. In contrast to previous work, we did not observe the formation of pure Te nanowires in the intermediate assembly state, which excludes the uncorrelated two-phase mixture assembly. Instead, we observed the growth of Te nanowires concurrently with the attachment of CdTe. The pitches of helical structure are only ≈ 10 nm, which is similar to the thickness of the CdTe helical layer. The atomic ratio of Cd:Te is close to 1 in the helical layer and the preferred twist direction also precludes the simple

charge-dipole induction of twist.

In the initial 8 hours, the NPs connected to each other and assembled into a one-dimensional structure driven by dipole-dipole forces, hydrogen bonding, and van der Waals forces (Fig. 5.3a and b). Due to partially removed CYS on the surface of CdTe, the Te2- on the surface of CdTe NPs is more prone to exposure on the surface and easily oxidized into Te. A gradual growth of Te nanowires with a diameter ≈ 5 nm can be formed in a slow oxidation process (Fig. 5.3d a, f)[30]. Again, strong Van der Waals forces can bind Te nanowires and CdTe twisted structures. As NH2 is the chiral group in (D and L) CYS molecule, the hydrogen bonding show chiral orientation when it selectively bonding with COO-. Therefore, strong hydrogen bonding between NH2 and COO- induces the CdTe to adopt a preferable winding on the Te surface. The energy of the dipole attraction between NPs can be evaluated by classical formula for aligned dipoles. The energy of CdTe NPs with 3.4 nm dipole attraction is equal to 8.8 kJ/mole. The energy of the hydrogen bond between CYS-CYS is estimated to be 12.5 kJ/mole. The comparison with the molar energy of species clearly shows the possibility of formation of helical structures. Detailed analysis of the diameter of NPs chains shows very similar diameter of network structure with the helical CdTe layer on the Te nanowires surface. So, it is reasonable that the formation of binary helical core-shell structure arises from the direct attachment between twist NPs chains and Te nanowires by the interaction of dipole forces, van der Waals forces and hydrogen bonds.

5.2 Cysteine coated CdTe nanoparticle simulations

To confirm that the chirality of the CYS NP stabilizer is responsible for the chirality of the bulk structure, we performed coarse-grained Molecular Dynamics (MD) simulations of NP self-assembly. Our simulations incorporate three primary features of the experimental system - the excluded volume effects due to the NP shape, the attraction of the NPs to the surface of the nanowire, and finally the surface interactions introduced by the chiral cysteine stabilizer, Fig. 5.4a. Additionally, some initial simulations were performed with dipole-dipole interactions included to demonstrate the steps of nanowire formation; these forces were excluded for assembly studies because, as shown in the experiments, as the nanowire grows the charge and dipole moment diminish relative to the additional forces in the system. Excluded volume effects are captured in the typical way via a purely repulsive Weeks-Chandler-Anderson (WCA) potential[92]. To model the axial form of the nanowires, we confine particles using a harmonic well $U = \frac{1}{2}kx^2$ at the center of the simulation box. To include the "twisting" effect induced by the amino acid stabilizer, we include

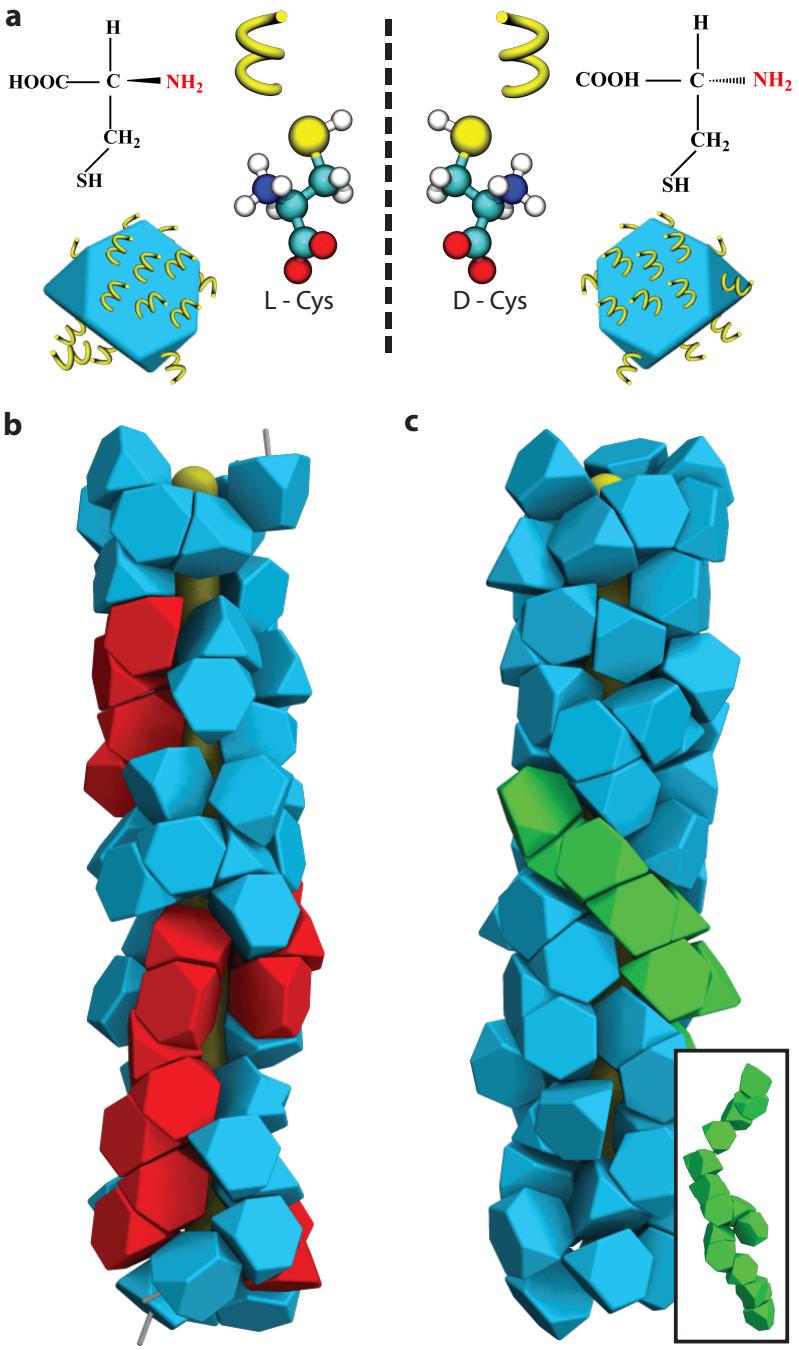

Figure 5.4: *Scheme and simulation*. (a) Two versions of the cysteine stabilizer are used, L - and D -CYS, which are of opposite chirality. Chemical structures are related to a "steric coil". Structures produce a predetermined twist based upon the chirality of the stabilizer by biasing local nanoparticle motifs. Either right (b) or left (c) handed structures are produced, depending upon the choice of "twist", as determined by a chiral interaction between nanoparticle faces. The inner structure of the wire is shown in yellow (c), with an outer layer of NPs removed. Insets show the unaltered wire (top), and centers of mass of the NPs connected with bonds along closest neighbors (bottom). Figure reproduced from our forthcoming publication, in preparation.[19]

a chiral potential that acts between interacting faces of the particles.

Initially, we conducted simulations without the chiral interaction and found chiral structures, but with no preferred handedness. In contrast, when we include the chiral surface interaction, to model the effects of L- and D- CYS, we still observed chiral structures, but the chirality was pre-determined by the chirality of the surface interaction. Structures with predictable chirality were observed in simulations of particles between 100 and 300 particles, and for rod diameters of 1 and 2 NP widths; the effects are particularly pronounced in simulations where the particle number, rod thickness, and box length were commensurate with a close, face-to-face packing of tetrahedra around the rod. Figures 5.4b, c demonstrate this effect with two structures of opposite chirality created by controlling the twist direction. A path through each rod highlights its overall handedness; Fig. 5.4b shows this path in green through a left-handed structure, while Fig. 5.4c shows a path in red. Figure 5.4c additionally contains two insets - at top, we show a full rod without particles removed, while at bottom the centers of mass of particles are shown with bonds drawn between nearest neighbors, demonstrating the pitch of this chiral arrangement.

We have shown that molecular chirality induces the formation of chiral superstructures. What do we expect in the case of racemic stabilizer-capped NPs? To answer this question, we further investigated via simulation the morphology of DL-CYS capped CdTe NP (DL-NPs) assemblies under the same conditions as previous experiments. Interestingly, TEM and AFM results show intertwined structures with diameter ≈ 40 nm, which is almost double the diameter compared with left and right hand helical structures (Fig. 5.5). HRTEM show twinning structures are composed of many intertwined ultrathin nanowires (≈ 2 nm) (Fig. 5.5c). FFT images imply the existence of Te nanowires. Unexpectedly, these split fibers are not twinned structures composed of left and right helices. It could imply that very short NPs chains composed by preferential binding with opposite-handed NPs in the early stages of assembly. Circular dichroism spectra show a broadening dispersive signal, which mostly from scattering due to the anisotropic structures. It is also coincidence with previous twisted ribbons assemble from non-chiral thioglycolic acids[66]. Simulations with a racemic mixture of stabilizer show no overall bulk preference of handedness. As shown in Fig. 5.5f particles prefer to mix, thereby eliminating a preferred local twist. In some cases, modest clustering of particle of similar twist do occur, but still do not result in an overall preference in handedness for the rods.

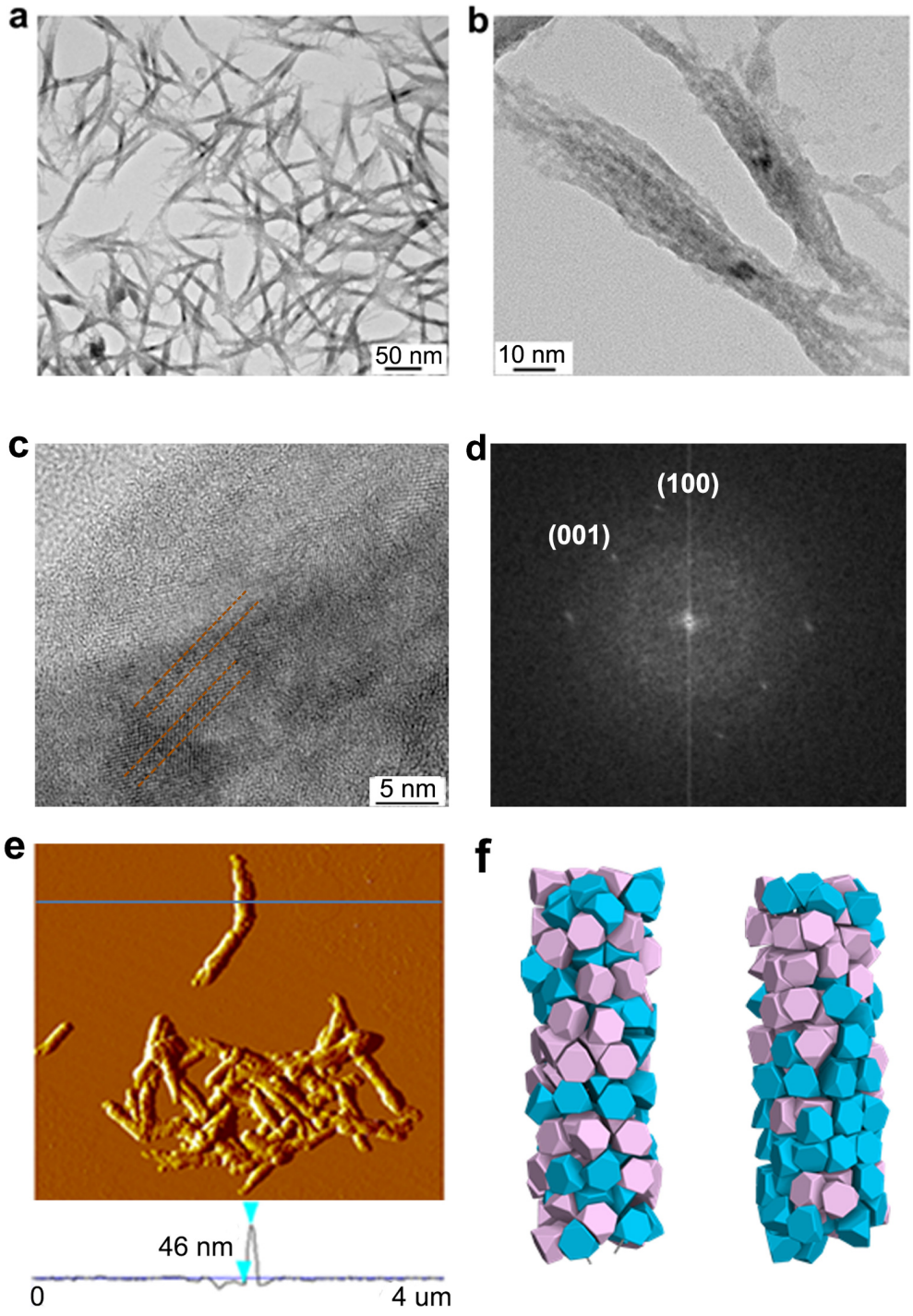

Figure 5.5: *Self-assembly of DL-NPs*. (a) and (b), Low magnification TEM. (c) and (d), High magnification TEM characterizations of twinning structures and corresponding fast Fourier transform pattern. (e), AFM characterization of self-assembled structures. (f), Simulations containing racemic mixture of L and R twisting tetrahedra. Figure reproduced from our forthcoming publication, in preparation.[19]

5.3 Concluding remarks on cysteine coated CdTe nanoparticles

In summary, we showed chiral helical structures can be assembled from CdTe NPs and the corresponding twist direction can be controlled by the chirality of stabilizers. We developed a model to coarse-grain the induced twist between pairs of interacting faces on our tetrahedra. This formulation can be generalized to study chiral interactions between particles of any geometry, and will be a useful tool for investigating other systems with shapes that possess a similar chiral twisting mechanism. This tool can be used to lay the ground work for a complete understanding of how the geometry and interaction of the NPs can affect the bulk optical properties of the nanowires. Our study demonstrates that mesoscale structure and chirality can be dictated by local interactions between nanoscale building blocks.

CHAPTER 6

Conclusion and Future Outlook

6.1 Summary of results

In summary, we have examined different systems, each of which targets a separate aspect of mesoscale assembly behavior. These studies demonstrate exquisite control of mesoscale structure and morphology by varying features of the system such as the building-block architecture, immiscibility between block segments and the solvent, as well as local interactions between nanoparticles themselves.

In the first study, we show that tethered nanoparticle building blocks can assemble phases such as lamellae, micelles, and network phases such as the double gyroid. By varying the architecture of the building block, we can tune between the types of phases the block prefers to form. In the case of "telechelics" the length of the polymer tether and size ratio between the end groups allowed us to tune between a wide variety of phases, as well as control the overall composition of the resulting domains. In the case of "giant surfactants", the geometry of the building block leads to a preference for micelle phases. The length of the attached polymer tether drives transitions between different types of micelle phases, which pack like "squishy" spheres with coronas of variable softness. These results are corroborated by experimental findings in systems of polyhedral oligomeric silsesquioxane (POSS) with attached polystyrene (PS) tethers; in both the computational and experimental systems identical mesophases emerge as the length of the polymer tether increases. We demonstrate specific transitions between hexagonal tubes, Frank-Kasper phases, and the Sigma-phase quasicrystal approximant for this building-block.

Our second study uses a modification of MD, dissipative particle dynamics (DPD), to establish the role of unreacted hydroxyl star polymer end-groups in stabilizing microdroplet assemblies. We show that by changing both the length and number of the polymer arms we can tune between 3 types of mesoscopic assemblies - porous, non-hollow, and hollow droplets. We confirm that a critical hydroxyl density is necessary to trigger the hollow to

non-hollow droplet transition. Through a single control parameter, the hydroxyl density, we demonstrated transitions between solid, hollow, and porous droplets.

Finally, our third study demonstrates that local nanoparticle interactions can bias the bulk chirality of a pseudo-1D assembly. By coating CdTe nanoparticles with a chiral amino-acid stabilizer, Cysteine, it is possible to predictably bias the handedness of rods and wires created from the nanoparticles. Via simulation, we establish that local twist originating from the Cysteine coating on the nanoparticle surface can locally bias assemblies. Additionally, we demonstrate that the pitch and structure of the rod can depend critically on the nanoparticle shape.

6.2 Concluding remarks

With powerful tools in hand both to synthesize building blocks of arbitrary complexity [40, 41, 57], and to simulate their assembly behavior [65, 16], it is tempting to begin exploring complex assemblies that could lead to new applications and devices [142, 146, 141, 164]. A pressing challenge is unifying these tools before moving into application. We have highlighted just a few of the conceptual design axes, as we highlight in Fig. 1.4 shows. Despite having already sketched out a framework that encompasses the vast design space [28], linking structural prediction to properties within a simulation framework would expedite application-specific design. As new building blocks and assemblies continue to emerge, the fundamental question is no longer *if* we can build targeted structures of exquisite complexity, but *how* we can design a target structure? What specific building blocks or set of interactions may lead to its formation, and how can the assembled structure be utilized from a technology stand point?

Knowing the target structure that will suit a particular application is one of the most crucial aspects of the problem. Diamond structures, for example, are known to be excellent candidates for photonics applications[165, 166, 167, 168]. The challenge is then to supply a proper set of design conditions to produce the structure. Computation allows us to rapidly screen candidate blocks for targeted assemblies. New data science approaches, coupled with high performance computing-enabled prediction of nano building-block self-assembly, promise to further expedite material design in this space [169, 170, 171], in the spirit of the Materials Genome Initiative [172].

In conclusion, we have several studies of nanoparticle building blocks that highlight the wide range of mesoscopic assemblies accessible by tuning block architecture and interaction. In several studies we have predicted, via simulations, novel phases for different architectures. Many of the blocks we proposed have since been synthesized, and structures

we predicted in those papers have now been realized.

We reviewed the groundwork that enabled the synthesis of these building blocks, and discussed self-assembled structures that have been made in bulk quantities using these nanoparticles. Finally, we discussed the computational work that played a role in both establishing the feasibility of assembling these nanoparticles, as well as making predictions of self-assembly behavior that have since been corroborated with experiments.

Importantly, our predictions are not specific to particular material types, and thus can guide the synthesis and assembly of many types of nanoparticle building blocks. Moreover, our design approach provides experimentalists flexibility in their design strategy - the same set of results holds equally for polymer-tethered gold particles as for, say, giant surfactants of ligand functionalized POSS molecules, provided the geometric length scales of particle and tether are commensurate; the same is true for nanoparticles of different types, ranging from semi-conducting to noble metals. Any materials that are amenable to surface modification can be incorporated into this scheme, providing a versatile materials design platform.

BIBLIOGRAPHY

[1] Subbiah, R., Veerapandian, M., and Yun, K. S., "Nanoparticles: Functionalization and Multifunctional Applications in Biomedical Sciences," *Current Medicinal Chemistry*, Vol. 17, 2010, pp. 4559–4577.

[2] Yue, K., Liu, C., Guo, K., Wu, K., Dong, X.-H., Liu, H., Huang, M., Wesdemiotis, C., Cheng, S. Z. D., and Zhang, W.-B., "Exploring shape amphiphiles beyond giant surfactants: molecular design and click synthesis," *Polymer Chemistry*, Vol. 4, No. 4, 2013, pp. 1056–1067.

[3] Zhang, Y., Lu, F., Yager, K. G., van der Lelie, D., and Gang, O., "A general strategy for the DNA-mediated self-assembly of functional nanoparticles into heterogeneous systems," *Nature Nanotechnology*, Vol. 8, No. October, Oct. 2013, pp. 865–872.

[4] Macfarlane, R. J., Lee, B., Jones, M. R., Harris, N., Schatz, G. C., and Mirkin, C. A., "Nanoparticle Superlattice Engineering with DNA," *Science*, Vol. 334, No. 6053, Oct. 2011, pp. 204–208.

[5] Li, W., Kim, Y., Li, J., and Li, M., "Dynamic self-assembly of coordination polymers in aqueous solution," *Soft Matter*, Vol. 10, 2014, pp. 5231–5242.

[6] Lahann, J., "Recent progress in nano-biotechnology: compartmentalized micro- and nanoparticles via electrohydrodynamic co-jetting," *Small*, Vol. 7, 2011, pp. 1149–1156.

[7] Lee, K. J., Yoon, J., and Lahann, J., "Recent advances with anisotropic particles," *Current Opinion in Colloid & Interface Science*, Vol. 16, 2011, pp. 195–202.

[8] Lee, K., Yoon, J., Rahmanic, S., Hwang, S., Bhaskar, S., Mitragotri, S., and Lahann, J., "Spontaneous shape reconfigurations in multicompartmental microcylinders," *Proceedings of National Academy of Science USA*, Vol. 109, 2012, pp. 16057–16062.

[9] Marson, R. L., Nguyen, T. D., and Glotzer, S. C., "Rational design of nanomaterials from assembly and reconfigurability of polymer-tethered nanoparticles," *MRS Communications*, 2015.

[10] Hayashida, K., Dotera, T., Takano, A., and Matsushita, Y., "Polymeric quasicrystal: Mesoscopic quasicrystalline tiling in ABC star polymers," *Physical Review Letters*, Vol. 98, No. May, 2007, pp. 1–4.

[11] Marson, R. L., Phillips, C. L., Anderson, J. A., and Glotzer, S. C., "Phase behavior and complex crystal structures of self-assembled tethered nanoparticle telechelics," *Nano Letters*, Vol. 14, 2014, pp. 2071–2078.

[12] Iacovella, C. R. and Glotzer, S. C., "Complex crystal structures formed by the self-assembly of ditethered nanospheres." *Nano Letters*, Vol. 9, No. 3, March 2009, pp. 1206–11.

[13] Nguyen, T. and Glotzer, S. C., "Reconfigurable assemblies of shape-changing nanorods," *ACS nano*, Vol. 4, No. 5, 2010, pp. 2585–2594.

[14] Iacovella, C. R., Keys, A. S., and Glotzer, S. C., "Self-assembly of soft-matter quasicrystals and their approximants," *Proceedings of the National Academy of Sciences*, Vol. 108, 2011, pp. 20935–20940.

[15] Spellings, M. P., Marson, R. L., Anderson, J. A., and Glotzer, S. C., "GPU accelerated Discrete Element Method (DEM) Molecular Dynamics," *In preparation*, 2015.

[16] Marson, R. L., Phillips, C. L., Anderson, J. A., and Glotzer, S. C., "Phase behavior and complex crystal structures of self-assembled tethered nanoparticle telechelics." *Nano letters*, Vol. 14, No. 4, April 2014, pp. 2071–8.

[17] Iacovella, C. R., Keys, A. S., and Glotzer, S. C., "Self-assembly of soft-matter quasicrystals and their approximants." *Proceedings of the National Academy of Sciences of the United States of America*, Vol. 108, No. 52, Dec. 2011, pp. 20935–20940.

[18] Zhang, Z., Marson, R. L., Zhishen, G., Glozter, S. C., and Ma, P. X., "Simultaneous nano- and microscale control of nanofibrous microspheres self-assembled from star-shaped polymers," *Macromolecules*, 2015.

[19] Zhou, Y., Marson, R., van Anders, G., Zhu, J., Ma, G., Ercius, P., Sun, K., Yeom, B., Krayev, A., Glotzer, S., and Kotov, N., "Enantioselectivity of Biomimetic Rod-Like Supraparticles Self-Assembled from Chiral Nanoparticles," *In preperation*, 2015.

[20] Glotzer, S. C., "Assembly engineering: Materials design for the 21st centruy," *Chemical Engineering Science*, Vol. 121, 2014, pp. 3–9.

[21] Berendsen, H., van der Spoel, D., and van Drunen, R., "GROMACS: A message-passing parallel molecular dynamics implementation," *Computer Physics Communications*, Vol. 91, No. 1-3, 1995, pp. 43–56.

[22] Plimpton, S., "Fast parallel algorithms for short-range molecular dynamics," 1995.

[23] Anderson, J. and Glotzer, S., "The development and expansion of HOOMD-blue through six years of GPU proliferation," *arXiv preprint arXiv:1308.5587*, 2013.

[24] Glaser, J., Nguyen, T. D., Anderson, J. A., Lui, P., Spiga, F., Millan, J. A., Morse, D. C., and Glotzer, S. C., "Strong scaling of general-purpose molecular dynamics simulations on GPUs," *Computer Physics Communications*, 2015.

[25] Bates, F. and Fredrickson, G., "Block copolymers - designer soft materials," *Physics today*, Vol. 52, No. February, 1999, pp. 32.

[26] Meuler, A. J., Hillmyer, M. A., and Bates, F. S., "Ordered Network Mesostructures in Block Polymer Materials," *Macromolecules*, Vol. 42, No. 19, Oct. 2009, pp. 7221–7250.

[27] Xu, W., Jiang, K., Zhang, P., and Shi, A.-C., "A Strategy to Explore Stable and Metastable Ordered Phases of Block Copolymers." *The journal of physical chemistry. B*, April 2013.

[28] Glotzer, S. C. and Solomon, M. J., "Anisotropy of building blocks and their assembly into complex structures." *Nature Materials*, Vol. 6, No. 8, Aug. 2007, pp. 557–62.

[29] Lilly, G., Lee, J., Sun, K., Tang, Z., Kim, K.-S., and Kotov, N., "Media Effect on CdTe Nanowire Growth: Mechanism of Self-Assembly, Ostwald Ripening, and Control of NW Geometry," *Journal of Physical Chemistry C*, Vol. 112, No. 2, Jan. 2008, pp. 370–377.

[30] Tang, Z., Wang, Y., Sun, K., and Kotov, N. A., "Spontaneous transformation of stabilizer-depleted binary semiconductor nanoparticles into selenium and tellurium nanowires," *Advanced Materials*, Vol. 17, No. 3, 2005, pp. 358–363.

[31] Yang, M. and Kotov, N. A., "Nanoscale helices from inorganic materials," *Journal of Materials Chemistry*, Vol. 21, No. 19, 2011, pp. 6775.

[32] Xia, Y., Nguyen, T. D., Yang, M., Lee, B., Santos, A., Podsiadlo, P., Tang, Z., Glotzer, S. C., and Kotov, N. A., "Self-assembly of self-limiting monodisperse supraparticles from polydisperse nanoparticles." *Nature nanotechnology*, Vol. 6, No. 9, Sept. 2011, pp. 580–7.

[33] Zhou, Y., Yang, M., Sun, K., Tang, Z., and Kotov, N. A., "Similar topological origin of chiral centers in organic and nanoscale inorganic structures: effect of stabilizer chirality on optical isomerism and growth of CdTe nanocrystals." *Journal of the American Chemical Society*, Vol. 132, No. 17, May 2010, pp. 6006–13.

[34] Tang, Z., Zhang, Z., Wang, Y., Glotzer, S. C., and Kotov, N. A., "Self-assembly of CdTe nanocrystals into free-floating sheets." *Science (New York, N.Y.)*, Vol. 314, No. 5797, Oct. 2006, pp. 274–8.

[35] Westenhoff, S. and Kotov, N. A., "Quantum dot on a rope." *Journal of the American Chemical Society*, Vol. 124, No. 11, March 2002, pp. 2448–9.

[36] Park, J. I., Nguyen, T. D., de Queirós Silveira, G., Bahng, J. H., Srivastava, S., Zhao, G., Sun, K., Zhang, P., Glotzer, S. C., and Kotov, N. A., "Terminal supraparticle assemblies from similarly charged protein molecules and nanoparticles." *Nature communications*, Vol. 5, No. May, Jan. 2014, pp. 3593.

[37] Yeom, J., Yeom, B., Chan, H., Smith, K. W., Dominguez-Medina, S., Bahng, J. H., Zhao, G., Chang, W.-S., Chang, S.-J., Chuvilin, A., Melnikau, D., Rogach, A. L., Zhang, P., Link, S., Král, P., and Kotov, N. A., "Chiral templating of self-assembling nanostructures by circularly polarized light." *Nature Materials*, Vol. 14, No. 1, Jan. 2015, pp. 66–72.

[38] Henzie, J., Grünwald, M., Widmer-Cooper, A., Geissler, P. L., and Yang, P., "Self-assembly of uniform polyhedral silver nanocrystals into densest packings and exoticsuperlattices," *Nature Materials*, Vol. 11, No. 2, Nov. 2011, pp. 131–137.

[39] Zhang, Z. and Glotzer, S. C., "Self-assembly of Patchy Particles," *Nano letters*, Vol. 4, No. 8, Dec. 2004, pp. 1407–1413.

[40] Zhang, W.-b., Yu, X., Wang, C.-l., Sun, H.-j., Hsieh, I.-f., Li, Y., Dong, X.-h., Yue, K., Horn, R. V., and Cheng, S. Z. D., "Molecular Nanoparticles Are Unique Elements for Macromolecular Science : From Nanoatoms to Giant Molecules," *Macromolecules*, Vol. 47, 2013, pp. 1221–1239.

[41] Gong, J., Li, G., and Tang, Z., "Self-assembly of noble metal nanocrystals: Fabrication, optical property, and application," *Nano Today*, Vol. 7, No. 6, Dec. 2012, pp. 564–585.

[42] Liao, C.-W., Lin, Y.-S., Chanda, K., Song, Y.-F., and Huang, M. H., "Formation of diverse supercrystals from self-assembly of a variety of polyhedral gold nanocrystals." *Journal of the American Chemical Society*, Vol. 135, No. 7, Feb. 2013, pp. 2684–93.

[43] Yaroslavov, A. A., Sinani, V. a., Efimova, A. A., Yaroslavova, E. G., Rakhnyanskaya, A. A., Ermakov, Y. A., and Kotov, N. A., "What is the effective charge of TGA-stabilized CdTe nanocolloids?" *Journal of the American Chemical Society*, Vol. 127, No. 20, May 2005, pp. 7322–3.

[44] Zhou, Y., Zhu, Z., Huang, W., Liu, W., Wu, S., Liu, X., Gao, Y., Zhang, W., and Tang, Z., "Optical coupling between chiral biomolecules and semiconductor nanoparticles: Size-dependent circular dichroism absorption," *Angewandte Chemie - International Edition*, Vol. 50, No. 48, 2011, pp. 11456–11459.

[45] Bates, F. S., Hillmyer, M. A., Lodge, T. P., Bates, C. M., Delaney, K. T., and Fredrickson, G. H., "Multiblock polymers: panacea or Pandora's box?" *Science (New York, N.Y.)*, Vol. 336, No. 6080, April 2012, pp. 434–40.

[46] Epps III, T., Cochran, E., Hardy, C., Bailey, T., Waletzko, R., and Bates, F., "Network phases in ABC triblock copolymers," *Macromolecules*, Vol. 37, No. 19, 2004, pp. 7085–7088.

[47] Kirkensgaard, J. J. K., "Striped networks and other hierarchical structures in A_{m}B_{m}C_{n} (2m+n)-miktoarm star terpolymer melts," *Physical Review E*, Vol. 85, No. 3, March 2012, pp. 031802.

[48] Judas, J. and Kirkensgaard, K., "Kaleidoscopic tilings, networks and hierarchical structures in blends of 3-miktoarm star terpolymers." *Interface focus*, Vol. 2, No. 5, Oct. 2012, pp. 602–7.

[49] Guo, Z., Zhang, G., Qiu, F., Zhang, H., Yang, Y., and Shi, A.-C., "Discovering Ordered Phases of Block Copolymers: New Results from a Generic Fourier-Space Approach," *Physical Review Letters*, Vol. 101, No. 2, July 2008, pp. 1–4.

[50] Capone, B., Coluzza, I., LoVerso, F., Likos, C. N., and Blaak, R., "Telechelic star polymers as self-assembling units from the molecular to the macroscopic Scale," *Physical Review Letters*, Vol. 109, No. 23, Dec. 2012, pp. 238301.

[51] Zhang, Z., Horsch, M. A., Lamm, M. H., and Glotzer, S. C., "Tethered Nano Building Blocks: Toward a Conceptual Framework for Nanoparticle Self-Assembly," *Nano Letters*, Vol. 3, No. 10, Oct. 2003, pp. 1341–1346.

[52] Kotov, N. A., *Nanoparticle assemblies and superstructures*, CRC Press, 2014.

[53] Kolb, H. C., Finn, M. G., and Sharpless, K. B., "Click Chemistry: Diverse Chemical Function from a Few Good Reactions." *Angewandte Chemie (International ed. in English)*, Vol. 40, No. 11, June 2001, pp. 2004–2021.

[54] Lee, S., Bluemle, M. J., and Bates, F. S., "Discovery of a Frank-Kasper sigma phase in sphere-forming block copolymer melts." *Science (New York, N.Y.)*, Vol. 330, No. 6002, Oct. 2010, pp. 349–53.

[55] Zhang, C., Macfarlane, R. J., Young, K. L., Choi, C. H. J., Hao, L., Auyeung, E., Liu, G., Zhou, X., and Mirkin, C. a., "A general approach to DNA-programmable atom equivalents." *Nature materials*, Vol. 12, No. 8, May 2013, pp. 741–746.

[56] Choi, J. J., Bealing, C. R., Bian, K., Hughes, K. J., Zhang, W., Smilgies, D.-M., Hennig, R. G., Engstrom, J. R., and Hanrath, T., "Controlling nanocrystal superlattice symmetry and shape-anisotropic interactions through variable ligand surface coverage." *Journal of the American Chemical Society*, Vol. 133, No. 9, March 2011, pp. 3131–8.

[57] Zhang, L., Niu, W., and Xu, G., "Synthesis and applications of noble metal nanocrystals with high-energy facets," *Nano Today*, Vol. 7, No. 6, Dec. 2012, pp. 586–605.

[58] Zhang, C., Macfarlane, R. J., Young, K. L., Choi, C. H. J., Hao, L., Auyeung, E., Liu, G., Zhou, X., and Mirkin, C. a., "A general approach to DNA-programmable atom equivalents." *Nature materials*, Vol. 12, No. 8, May 2013, pp. 741–746.

[59] Yu, X., Yue, K., Hsieh, I.-f., and Li, Y., "Giant surfactants provide a versatile platform for sub-10-nm nanostructure engineering," *Proceedings of the National Academy of Sciences*, Vol. 110, No. 25, 2013, pp. 10078–10083.

[60] Pawar, A. B. and Kretzschmar, I., "Fabrication, assembly, and application of patchy particles," *Macromolecular Rapid Communications*, Vol. 31, 2010, pp. 150–168.

[61] Sacanna, S. and Pine, D., "Shape-anisotropic colloids: Building blocks for complex assemblies," *Current Opinion in Colloid and Interface Science*, Vol. 16, 2011, pp. 96–105.

[62] Bates, F. S. and Fredrickson, G. H., "Block copolymer thermodynamics: theory and experiment." *Annual review of physical chemistry*, Vol. 41, Jan. 1990, pp. 525–57.

[63] Qin, J., Bates, F. S., and Morse, D. C., "Phase Behavior of Nonfrustrated ABC Triblock Copolymers: Weak and Intermediate Segregation," *Macromolecules*, Vol. 43, No. 11, June 2010, pp. 5128–5136.

[64] Agarwal, U. and Escobedo, F. a., "Mesophase behaviour of polyhedral particles." *Nature materials*, Vol. 10, No. 3, March 2011, pp. 230–5.

[65] Damasceno, P. F., Engel, M., and Glotzer, S. C., "Predictive self-assembly of polyhedra into complex structures," *Science*, Vol. 337, No. 6093, July 2012, pp. 453–457.

[66] Srivastava, S., Santos, A., Critchley, K., Kim, K.-S., Podsiadlo, P., Sun, K., Lee, J., Xu, C., Lilly, G. D., Glotzer, S. C., and Kotov, N. A., "Light-controlled self-assembly of semiconductor nanoparticles into twisted ribbons." *Science (New York, N.Y.)*, Vol. 327, No. 5971, March 2010, pp. 1355–9.

[67] Li, C., Deng, K., Tang, Z., and Jiang, L., "Twisted Metal - Amino Acid Nanobelts : Chirality Transcription," , No. 13, 2010, pp. 8202–8209.

[68] Aggeli, A., Nyrkova, I. A., Bell, M., Harding, R., Carrick, L., McLeish, T. C., Semenov, A. N., and Boden, N., "Hierarchical self-assembly of chiral rod-like molecules as a model for peptide beta -sheet tapes, ribbons, fibrils, and fibers." *Proceedings of the National Academy of Sciences of the United States of America*, Vol. 98, No. 21, 2001, pp. 11857–11862.

[69] Glotzer, S. C., Horsch, M. A., Iacovella, C. R., Zhang, X. L., Chan, E., and Zhang, X., "Self-assembly of anisotropic tethered nanoparticle shape amphiphiles," *Current Opinion in Colloid & Interface Science*, Vol. 10, No. 5-6, Dec. 2005, pp. 287–295.

[70] Iacovella, C. R., Horsch, M. A., Zhang, Z., and Glotzer, S. C., "Phase diagrams of self-assembled mono-tethered nanospheres from molecular simulation and comparison to surfactants." *Langmuir*, Vol. 21, No. 21, Oct. 2005, pp. 9488–94.

[71] Tschierske, C., "Liquid crystal engineering–new complex mesophase structures and their relations to polymer morphologies, nanoscale patterning and crystal engineering." *Chemical Society reviews*, Vol. 36, No. 12, Dec. 2007, pp. 1930–70.

[72] Iacovella, C., Keys, A., Horsch, M., and Glotzer, S., "Icosahedral packing of polymer-tethered nanospheres and stabilization of the gyroid phase," *Physical Review E*, Vol. 75, No. 4, April 2007, pp. 1–4.

[73] Phillips, C. L., Iacovella, C. R., and Glotzer, S. C., "Stability of the double gyroid phase to nanoparticle polydispersity in polymer-tethered nanosphere systems," *Soft Matter*, Vol. 6, No. 8, 2010, pp. 1693–1703.

[74] Jayaraman, A. and Schweizer, K. S., "Effective Interactions, Structure, and Phase Behavior of Lightly Tethered Nanoparticles in Polymer Melts," *Macromolecules*, Vol. 41, No. 23, Dec. 2008, pp. 9430–9438.

[75] Jayaraman, A. and Schweizer, K. S., "Structure and assembly of dense solutions and melts of single tethered nanoparticles." *The Journal of chemical physics*, Vol. 128, No. 16, April 2008, pp. 164904.

[76] Jayaraman, A. and Schweizer, K. S., "Effective Interactions and Self-Assembly of Hybrid Polymer Grafted Nanoparticles in a Homopolymer Matrix," *Macromolecules*, Vol. 42, No. 21, Nov. 2009, pp. 8423–8434.

[77] Hall, L. M., Jayaraman, A., and Schweizer, K. S., "Molecular theories of polymer nanocomposites," *Current Opinion in Solid State and Materials Science*, Vol. 14, No. 2, April 2010, pp. 38–48.

[78] Nair, N., Wentzel, N., and Jayaraman, A., "Effect of bidispersity in grafted chain length on grafted chain conformations and potential of mean force between polymer grafted nanoparticles in a homopolymer matrix." *The Journal of chemical physics*, Vol. 134, No. 19, May 2011, pp. 194906.

[79] Horsch, M. A., Zhang, Z., and Glotzer, S. C., "Self-assembly of end-tethered nanorods in a neat system and role of block fractions and aspect ratio," *Soft Matter*, Vol. 6, No. 5, 2010, pp. 945–954.

[80] Iacovella, C. R., Horsch, M. A., and Glotzer, S. C., "Local ordering of polymer-tethered nanospheres and nanorods and the stabilization of the double gyroid phase." *The Journal of Chemical Physics*, Vol. 129, No. 4, July 2008, pp. 044902.

[81] Nguyen, T. D., Zhang, Z., and Glotzer, S. C., "Molecular simulation study of self-assembly of tethered V-shaped nanoparticles." *The Journal of Chemical Physics*, Vol. 129, No. 24, Dec. 2008, pp. 244903.

[82] Horsch, M. A., Zhang, Z., and Glotzer, S. C., "Simulation studies of self-assembly of end-tethered nanorods in solution and role of rod aspect ratio and tether length." *The Journal of Chemical Physics*, Vol. 125, No. 18, Nov. 2006, pp. 184903.

[83] Horsch, M. A., Zhang, Z., and Glotzer, S. C., "Self-assembly of laterally-tethered nanorods." *Nano Letters*, Vol. 6, No. 11, Nov. 2006, pp. 2406–13.

[84] Horsch, M., Zhang, Z., and Glotzer, S., "Self-assembly of polymer-tethered nanorods," *Physical Review Letters*, Vol. 95, No. 5, July 2005, pp. 1–4.

[85] Damasceno, P. F., Engel, M., and Glotzer, S. C., "Crystalline assemblies and densest packings of a family of truncated tetrahedra and the role of directional entropic forces." *ACS nano*, Vol. 6, No. 1, Jan. 2012, pp. 609–14.

[86] Young, K. L., Personick, M. L., Engel, M., Damasceno, P. F., Barnaby, S. N., Bleher, R., Li, T., Glotzer, S. C., Lee, B., and Mirkin, C. A., "A Directional Entropic Force Approach to Assemble Anisotropic Nanoparticles into Superlattices," *Angewandte Chemie International Edition*, Nov. 2013, pp. n/a–n/a.

[87] Smallenburg, F., Vutukuri, H. R., Imhof, A., van Blaaderen, A., and Dijkstra, M., "Self-assembly of colloidal particles into strings in a homogeneous external electric or magnetic field." *Journal of physics. Condensed matter : an Institute of Physics journal*, Vol. 24, No. 46, Nov. 2012, pp. 464113.

[88] Dennison, M., Milinković, K., and Dijkstra, M., "Phase diagram of hard snowman-shaped particles." *The Journal of chemical physics*, Vol. 137, No. 4, July 2012, pp. 044507.

[89] Sarić, A., Bozorgui, B., and Cacciuto, A., "Packing of soft asymmetric dumbbells." *The Journal of Physical Chemistry. B*, Vol. 115, No. 22, June 2011, pp. 7182–9.

[90] Smallenburg, F., Filion, L., Marechal, M., and Dijkstra, M., "Vacancy-stabilized crystalline order in hard cubes." *Proceedings of the National Academy of Sciences of the United States of America*, Vol. 109, No. 44, Oct. 2012, pp. 17886–90.

[91] Iacovella, C. R. and Glotzer, S. C., "Phase behavior of ditethered nanospheres," *Soft Matter*, Vol. 5, No. 22, 2009, pp. 4492–4498.

[92] Chandler, D. and Weeks, J., "Van der Waals picture of liquids, solids, and phase transformations," *Science*, Vol. 220, 1983, pp. 787–794.

[93] Grest, G. and Kremer, K., "Molecular dynamics simulation for polymers in the presence of a heat bath," *Physical Review A*, Vol. 33, No. 5, 1986, pp. 3628.

[94] Anderson, J., Lorenz, C., and Travesset, A., "General purpose molecular dynamics simulations fully implemented on graphics processing units," *Journal of Computational Physics*, Vol. 227, No. 10, May 2008, pp. 5342–5359.

[95] Phillips, C. L., Anderson, J. A., and Glotzer, S. C., "Pseudo-random number generation for Brownian Dynamics and Dissipative Particle Dynamics simulations on GPU devices," *Journal of Computational Physics*, Vol. 230, No. 19, Aug. 2011, pp. 7191–7201.

[96] Ghaboussi, J. and Barbosa, R., "Three-dimensional discrete element method for granular materials," *International Journal for Numerical and Analytical Methods in Geomechanics*, Vol. 14, No. June 1987, 1990, pp. 451–472.

[97] Mack, S., Langston, P., Webb, C., and York, T., "Experimental validation of polyhedral discrete element model," *Powder Technology*, Vol. 214, No. 3, Dec. 2011, pp. 431–442.

[98] Wang, J., Yu, H. S., Langston, P., and Fraige, F., "Particle shape effects in discrete element modelling of cohesive angular particles," *Granular Matter*, Vol. 13, No. 1, Oct. 2010, pp. 1–12.

[99] Alonso-Marroquín, F. and Wang, Y., "An efficient algorithm for granular dynamics simulations with complex-shaped objects," *Granular Matter*, Vol. 11, No. 5, July 2009, pp. 317–329.

[100] Langston, P., Ai, J., and Yu, H.-S., "Simple shear in 3D DEM polyhedral particles and in a simplified 2D continuum model," *Granular Matter*, May 2013, pp. 13–15.

[101] Anderson, J. A., Jankowski, E., Grubb, T. L., and Engel, M., "Massively parallel Monte Carlo for many-particle simulations on GPUs," *arXiv preprint arXiv:* ....

[102] Bannerman, M. N., Sargant, R., and Lue, L., "DynamO: a free O(N) general event-driven molecular dynamics simulator." *Journal of computational chemistry*, Vol. 32, No. 15, Nov. 2011, pp. 3329–38.

[103] Marfn, M., "Event-driven hard-particle molecular dynamics using bulk-synchronous parallelism," Vol. 102, 1997, pp. 81–96.

[104] Miller, S. and Luding, S., "Event-driven molecular dynamics in parallel," *Journal of Computational Physics*, Vol. 193, No. 1, Jan. 2004, pp. 306–316.

[105] Imai, M., Sakai, K., Kikuchi, M., Nakaya, K., Saeki, A., and Teramoto, T., "Kinetic pathway to double-gyroid structure." *The Journal of Chemical Physics*, Vol. 122, No. 21, June 2005, pp. 214906.

[106] Matsen, M. W., "Gyroid versus double-diamond in ABC triblock copolymer melts," *The Journal of Chemical Physics*, Vol. 108, No. 2, 1998, pp. 785–796.

[107] Mogi, Y., Mori, K., and Matsushita, Y., "Tricontinuous morphology of triblock copolymers of the ABC type," *Macromolecules*, Vol. 25, 1992, pp. 5412–5415.

[108] Dotera, T. and Hatano, A., "The diagonal bond method: A new lattice polymer model for simulation study of block copolymers," *The Journal of Chemical Physics*, Vol. 105, No. 18, 1996, pp. 8413.

[109] Dotera, T., "Tricontinuous Cubic Structures in ABC/A/C Copolymer and Homopolymer Blends," *Physical Review Letters*, Vol. 89, No. 20, Oct. 2002, pp. 1–4.

[110] Anderson, J., Sknepnek, R., and Travesset, A., "Design of polymer nanocomposites in solution by polymer functionalization," *Physical Review E*, Vol. 82, No. 2, Aug. 2010, pp. 1–11.

[111] Imai, M., Kawaguchi, A., Saeki, A., Nakaya, K., Kato, T., Ito, K., and Amemiya, Y., "Fluctuations of lamellar structure prior to a lamellar–¿gyroid transition in a nonionic surfactant system," *Physical Review E*, Vol. 62, No. 5 Pt B, Nov. 2000, pp. 6865–74.

[112] Hajduk, D., Harper, P., and Gruner, S., "The gyroid: a new equilibrium morphology in weakly segregated diblock copolymers," *Macromolecules*, Vol. 27, 1994, pp. 4063–4075.

[113] Hamley, I. W., Koppi, K. A., Rosedale, J. H., Bates, F. S., Almdal, K., and Mortensen, K., "Hexagonal mesophases between lamellae and cylinders in a diblock copolymer melt," *Macromolecules*, Vol. 26, No. 22, Oct. 1993, pp. 5959–5970.

[114] Tyler, C., Qin, J., Bates, F., and Morse, D., "SCFT study of nonfrustrated ABC triblock copolymer melts," *Macromolecules*, Vol. 40, 2007, pp. 4654–4668.

[115] Grünwald, M., Lutker, K., Alivisatos, A. P., Rabani, E., and Geissler, P. L., "Metastability in Pressure-Induced Structural Transformations of CdSe/ZnS Core/Shell Nanocrystals." *Nano letters*, Vol. 13, July 2012, pp. 1367–1372.

[116] Cheng, X., Lin, L., E, W., Zhang, P., and Shi, A.-C., "Nucleation of Ordered Phases in Block Copolymers," *Physical Review Letters*, Vol. 104, No. 14, April 2010, pp. 1–4.

[117] Wales, D. J. and Doye, J., "Global optimization by basin-hopping and the lowest energy structures of Lennard-Jones clusters containing up to 110 atoms," *The Journal of Physical Chemistry A*, Vol. 5639, No. 97, 1997, pp. 5111–5116.

[118] Zhang, W. B., Yu, X., Wang, C. L., Sun, H. J., Hsieh, I. F., Li, Y., Dong, X. H., Yue, K., Van Horn, R., and Cheng, S. Z. D., "Molecular nanoparticles are unique elements for macromolecular science: From "nanoatoms" to giant molecules," *Macromolecules*, 2014.

[119] Wang, Z., Li, Y., Dong, X.-H., Yu, X., Guo, K., Su, H., Yue, K., Wesdemiotis, C., Cheng, S. Z. D., and Zhang, W.-B., "Giant gemini surfactants based on polystyrene-hydrophilic polyhedral oligomeric silsesquioxane shape amphiphiles: sequential click chemistry and solution self-assembly," *Chemical Science*, Vol. 4, No. 3, 2013, pp. 1345.

[120] Dong, X.-H., Zhang, W.-B., Li, Y., Huang, M., Zhang, S., Quirk, R. P., and Cheng, S. Z. D., "Synthesis of fullerene-containing poly(ethylene oxide)-block-polystyrene as model shape amphiphiles with variable composition, diverse architecture, and high fullerene functionality," *Polymer Chemistry*, Vol. 3, No. 1, 2012, pp. 124–134.

[121] Yu, X., Zhang, W.-B., Yue, K., Li, X., Liu, H., Xin, Y., Wang, C.-L., Wesdemiotis, C., and Cheng, S. Z. D., "Giant molecular shape amphiphiles based on polystyrene-hydrophilic [60]fullerene conjugates: click synthesis, solution self-assembly, and phase behavior." *Journal of the American Chemical Society*, Vol. 134, No. 18, May 2012, pp. 7780–7.

[122] Wang, Z., Li, Y., Dong, X.-H., Yu, X., Guo, K., Su, H., Yue, K., Wesdemiotis, C., Cheng, S. Z. D., and Zhang, W.-B., "Giant gemini surfactants based on polystyrene-hydrophilic polyhedral oligomeric silsesquioxane shape amphiphiles: sequential click chemistry and solution self-assembly," *Chemical Science*, Vol. 4, No. 3, 2013, pp. 1345.

[123] Tang, C., Lennon, E., and Fredrickson, G., "Evolution of Block Copolymer Lithography to Highly Ordered Square Arrays," *Science*, Vol. 322, No. October, 2008, pp. 429–432.

[124] Yang, R., Li, B., and Shi, A.-C., "Phase behavior of binary blends of diblock copolymer/homopolymer confined in spherical nanopores." *Langmuir : the ACS journal of surfaces and colloids*, Vol. 28, No. 2, Jan. 2012, pp. 1569–78.

[125] Chi, P., Wang, Z., Li, B., and Shi, A.-C., "Soft confinement-induced morphologies of diblock copolymers." *Langmuir : the ACS journal of surfaces and colloids*, Vol. 27, No. 18, Sept. 2011, pp. 11683–9.

[126] Yu, B., Sun, P., Chen, T., Jin, Q., Ding, D., Li, B., and Shi, A.-C., "Confinement-Induced Novel Morphologies of Block Copolymers," *Physical Review Letters*, Vol. 96, No. 13, April 2006, pp. 1–4.

[127] Zhao, W., Chen, H., Li, Y., Li, A., Lang, M., and Shi, J., "Uniform rattle-type hollow magnetic mesoporous spheres as drug delivery carriers and their sustained-release property," *Advanced Functional Materials*, Vol. 18, No. 18, 2008, pp. 2780–2788.

[128] Shi, A.-C. and Li, B., "Self-assembly of diblock copolymers under confinement," *Soft Matter*, 2013.

[129] Langer, R., "Drug delivery and targeting." *Nature*, Vol. 392, No. 6679 Suppl, 1998, pp. 5–10.

[130] Barbé, C., Bartlett, J., Kong, L., Finnie, K., Lin, H. Q., Larkin, M., Calleja, S., Bush, A., and Calleja, G., "Silica particles: A novel drug-delivery system," *Advanced Materials*, Vol. 16, No. 21, 2004, pp. 1959–1966.

[131] Comiskey, B., Albert, J. D., Yoshizawa, H., and Jacobson, J., "An electrophoretic ink for all-printed reflective electronic displays," *Nature*, Vol. 394, No. 6690, 1998, pp. 253–255.

[132] Shipway, a. N., Katz, E., and Willner, I., "Nanoparticle arrays on surfaces for electronic, optical, and sensor applications," *Angewandte Chemie (International Edition in English)*, Vol. 39, No. 15 SUPPL., 2000, pp. 19–52.

[133] Xia, Y., Gates, B., Yin, Y., and Lu, Y., "Monodispersed colloidal spheres: old materials with new applications," *Advanced Materials*, Vol. 12, No. 10, 2000, pp. 693–713.

[134] White, S. R., Sottos, N. R., Geubelle, P. H., Moore, J. S., Kessler, M. R., Sriram, S. R., Brown, E. N., and Viswanathan, S., "Autonomic healing of polymer composites." *Nature*, Vol. 409, No. 6822, 2001, pp. 794–797.

[135] Kim, S. W., Kim, M., Lee, W. Y., and Hyeon, T., "Fabrication of hollow palladium spheres and their successful application to the recyclable heterogeneous catalyst for suzuki coupling reactions," *Journal of the American Chemical Society*, Vol. 124, No. 26, 2002, pp. 7642–7643.

[136] Liu, Y. and Zhang, X., "Metamaterials: a new frontier of science and technology." *Chemical Society reviews*, Vol. 40, No. 5, 2011, pp. 2494–2507.

[137] Flory, P. J., "Thermodynamics of high polymer solutions," *The Journal of Chemical Physics*, Vol. 9, No. 8, 1941, pp. 660–660.

[138] Zhang, W. and Zheng, S., "Synthesis and characterization of dendritic star poly(L-lactide)s," *Polymer Bulletin*, Vol. 58, No. 5-6, 2007, pp. 767–775.

[139] Zhao, Y., Shuai, X., Chen, C., and Xi, F., "Synthesis and Characterization of Star-Shaped Poly (L -lactide) s Initiated with Hydroxyl-Terminated Poly (Amidoamine) (PAMAM-OH) Dendrimers," *Chemistry of Materials*, Vol. 15, No. 14, 2003, pp. 2836–2843.

[140] Govorov, A. O., Gun'ko, Y. K., Slocik, J. M., Gérard, V. A., Fan, Z., and Naik, R. R., "Chiral nanoparticle assemblies: circular dichroism, plasmonic interactions, and exciton effects," *Journal of Materials Chemistry*, Vol. 21, No. 42, 2011, pp. 16806.

[141] Saba, M., Turner, M. D., Mecke, K., Gu, M., and Schröder-Turk, G. E., "Group theory of circular-polarization effects in chiral photonic crystals with four-fold rotation axes applied to the eight-fold intergrowth of gyroid nets," *Physical Review B - Condensed Matter and Materials Physics*, Vol. 88, 2013, pp. 1–16.

[142] Saba, M., Thiel, M., Turner, M., Hyde, S., Gu, M., Grosse-Brauckmann, K., Neshev, D., Mecke, K., and Schröder-Turk, G., "Circular dichroism in biological photonic crystals and cubic chiral nets," *Physical Review Letters*, Vol. 106, No. 10, March 2011, pp. 103902.

[143] Song, C., Blaber, M. G., Zhao, G., Zhang, P., Fry, H. C., Schatz, G. C., and Rosi, N. L., "Tailorable plasmonic circular dichroism properties of helical nanoparticle superstructures," *Nano Letters*, Vol. 13, No. 7, 2013, pp. 3256–3261.

[144] Govorov, A. O., Fan, Z., Hernandez, P., Slocik, J. M., and Naik, R. R., "Theory of circular dichroism of nanomaterials comprising chiral molecules and nanocrystals: Plasmon enhancement, dipole interactions, and dielectric effects," *Nano Letters*, Vol. 10, No. 4, 2010, pp. 1374–1382.

[145] Schröder-Turk, G. E., Wickham, S., Averdunk, H., Brink, F., Fitz Gerald, J. D., Poladian, L., Large, M. C. J., and Hyde, S. T., "The chiral structure of porous chitin

within the wing-scales of Callophrys rubi." *Journal of structural biology*, Vol. 174, No. 2, May 2011, pp. 290–5.

[146] Turner, M. D., Saba, M., Zhang, Q., Cumming, B. P., Schröder-Turk, G. E., and Gu, M., "Miniature chiral beamsplitter based on gyroid photonic crystals," *Nature Photonics*, , No. September, Sept. 2013, pp. 1–5.

[147] Saranathan, V., Osuji, C., Mochrie, S., Noh, H., Narayanan, S., Sandy, A., Dufresne, E., and Prum, R., "Structure, function, and self-assembly of single network gyroid photonic crystals in butterly wing scales," *Proceedings of the National Academy of Sciences*, Vol. 107, No. 26, 2010, pp. 11676–11681.

[148] Parker, A. R. and Townley, H. E., "Biomimetics of photonic nanostructures." *Nature nanotechnology*, Vol. 2, No. 6, 2007, pp. 347–353.

[149] Marini, D. M., Hwang, W., Lauffenburger, D. A., Zhang, S., and Kamm, R. D., "Left-handed helical ribbon intermediates in the self-assembly of a β-sheet Peptide," *Nano Letters*, Vol. 2, No. 4, 2002, pp. 295–299.

[150] Shopsowitz, K. E., Qi, H., Hamad, W. Y., and Maclachlan, M. J., "Free-standing mesoporous silica films with tunable chiral nematic structures." *Nature*, Vol. 468, No. 7322, 2010, pp. 422–425.

[151] Li, Y., Zhou, Y., Wang, H. Y., Perrett, S., Zhao, Y., Tang, Z., and Nie, G., "Chirality of glutathione surface coating affects the cytotoxicity of quantum dots," *Angewandte Chemie - International Edition*, Vol. 50, No. 26, 2011, pp. 5860–5864.

[152] Kotov, N. A., "Inorganic nanoparticles as protein mimics," *Science*, Vol. 330, No. 6001, 2010, pp. 188–189.

[153] Gaponik, N., Talapin, D. V., Rogach, A. L., Hoppe, K., Shevchenko, E. V., Kornowski, A., Eychmüller, A., and Weller, H., "Thiol-capping of CDTe nanocrystals: An alternative to organometallic synthetic routes," *Journal of Physical Chemistry B*, Vol. 106, No. 29, 2002, pp. 7177–7185.

[154] Klug, a., "The tobacco mosaic virus particle: structure and assembly." *Philosophical transactions of the Royal Society of London. Series B, Biological sciences*, Vol. 354, No. 1383, 1999, pp. 531–535.

[155] Prins, L. J., Huskens, J., de Jong, F., Timmerman, P., and Reinhoudt, D. N., "Complete asymmetric induction of supramolecular chirality in a hydrogen-bonded assembly," *Nature*, Vol. 398, No. 6727, 1999, pp. 498–502.

[156] Mark, A. G., Gibbs, J. G., Lee, T.-C., and Fischer, P., "Hybrid nanocolloids with programmed three-dimensional shape and material composition," *Nature Materials*, Vol. 12, No. 6, June 2013, pp. 1–6.

[157] Jung, S. H., Jeon, J., Kim, H., Jaworski, J., and Jung, J. H., "Chiral Arrangement of Achiral Au Nanoparticles by Supramolecular Assembly of Helical Nanofiber Templates." *Journal of the American Chemical Society*, April 2014.

[158] Hao, C., Xu, L., Ma, W., Wang, L., Kuang, H., and Xu, C., "Assembled Plasmonic Asymmetric Heterodimers with Tailorable Chiroptical Response." *Small (Weinheim an der Bergstrasse, Germany)*, Feb. 2014, pp. 1–8.

[159] Zhao, Y., Sakai, F., Su, L., Liu, Y., Wei, K., Chen, G., and Jiang, M., "Progressive Macromolecular Self-Assembly: From Biomimetic Chemistry to Bio-Inspired Materials," *Advanced Materials*, Sept. 2013, pp. n/a–n/a.

[160] Zhang, S., "Fabrication of novel biomaterials through molecular self-assembly." *Nature biotechnology*, Vol. 21, No. 10, 2003, pp. 1171–1178.

[161] Paramonov, S. E., Jun, H. W., and Hartgerink, J. D., "Self-assembly of peptide-amphiphile nanofibers: The roles of hydrogen bonding and amphiphilic packing," *Journal of the American Chemical Society*, Vol. 128, No. 22, 2006, pp. 7291–7298.

[162] Bierman, M. J., Lau, Y. K. A., Kvit, A. V., Schmitt, A. L., and Jin, S., "Dislocation-driven nanowire growth and Eshelby twist." *Science (New York, N.Y.)*, Vol. 320, No. 5879, 2008, pp. 1060–1063.

[163] Cho, K. S., Talapin, D. V., Gaschler, W., and Murray, C. B., "Designing PbSe nanowires and nanorings through oriented attachment of nanoparticles," *Journal of the American Chemical Society*, Vol. 127, No. 19, 2005, pp. 7140–7147.

[164] Liu, F., Hou, Y., and Gao, S., "Well-ordered nanohybrids and nanoporous materials from gyroid block copolymer templates," *Chemical Society Reviews*, 2014.

[165] Urbas, A., Maldovan, M., DeRege, P., and Thomas, E., "Bicontinuous Cubic Block Copolymer Photonic Crystals," *Advanced Materials*, Vol. 14, No. 24, Dec. 2002, pp. 1850–1853.

[166] Maldovan, M., Urbas, A., Yufa, N., Carter, W., and Thomas, E., "Photonic properties of bicontinuous cubic microphases," *Physical Review B*, Vol. 65, No. 16, April 2002, pp. 1–5.

[167] Maldovan, M., Ullal, C. K., Carter, W. C., and Thomas, E. L., "Exploring for 3D photonic bandgap structures in the 11 f.c.c. space groups." *Nature materials*, Vol. 2, No. 10, Oct. 2003, pp. 664–7.

[168] Maldovan, M. and Thomas, E. L., "Diamond-structured photonic crystals." *Nature Materials*, Vol. 3, No. 9, Sept. 2004, pp. 593–600.

[169] Oganov, A. R., Lyakhov, A. O., and Valle, M., "How evolutionary crystal structure prediction works–and why." *Accounts of chemical research*, Vol. 44, No. 3, March 2011, pp. 227–37.

[170] Hansen, N. and Ostermeier, a., "Completely derandomized self-adaptation in evolution strategies." *Evolutionary computation*, Vol. 9, No. 2, Jan. 2001, pp. 159–95.

[171] Miskin, M. Z. and Jaeger, H. M., "Evolving design rules for the inverse granular packing problem," *Soft Matter*, Vol. 10, No. 21, 2014, pp. 3708.

[172] https://www.whitehouse.gov/mgi ; [Online; accessed 12-April-2015].